X66-14586

~~CONFIDENTIAL~~

UB
NASA TM X-1215

NASA TECHNICAL MEMORANDUM

UB
NASA TM X-1215

Declassified by authority of NASA
Classification Change Notices No. 220
Dated ** 28 FEB 1973

CLASSIFICATION CHANGE
Declassified
Authority of NASA T.N. 73-184
By E.P. Schmidt Date 1/11/73

~~NOFORN~~

STATIC LONGITUDINAL AERODYNAMIC CHARACTERISTICS OF A POWERED MODEL OF THE APOLLO LAUNCH-ESCAPE VEHICLE FROM MACH 0.50 TO 1.30

by Jack F. Runckel, James W. Schmeer, and Odis C. Pendergraft, Jr.

Langley Research Center
Langley Station, Hampton, Va.

CASE FILE COPY

NATIONAL AERONAUTICS AND SPACE ADMINISTRATION • WASHINGTON, D. C. • MARCH 1966

~~CONFIDENTIAL~~

[redacted]

NASA TM X-1215

STATIC LONGITUDINAL AERODYNAMIC CHARACTERISTICS OF A POWERED MODEL OF THE APOLLO LAUNCH-ESCAPE VEHICLE FROM MACH 0.50 TO 1.30

By Jack F. Runckel, James W. Schmeer,
and Odis C. Pendergraft, Jr.

Langley Research Center
Langley Station, Hampton, Va.

[redacted]

[redacted]

CLASSIFIED DOCU[redacted]D
nat[redacted]S.C.,
[redacted] and 794, the transmission or revelation
[redacted]d person
is prohibited by law.

[redacted]d not be returned after it has
[redacted]ed
of in accordance with your local security regula-
[redacted]ial
Security Manual for Safe Guarding Classified
Inform[redacted]

NATIONAL AERONAUTICS AND SPACE ADMINISTRATION

[redacted]

[redacted]

STATIC LONGITUDINAL AERODYNAMIC CHARACTERISTICS OF A POWERED MODEL OF THE APOLLO LAUNCH-ESCAPE VEHICLE FROM MACH 0.50 TO 1.30*

By Jack F. Runckel, James W. Schmeer,
and Odis C. Pendergraft, Jr.
Langley Research Center

SUMMARY

An investigation has been conducted in the Langley 16-foot transonic tunnel to determine the static longitudinal aerodynamic characteristics of a rocket-powered model of the Apollo launch-escape vehicle. The effects of rocket jet exhaust on the command-module pressure distributions were also obtained. The tests were conducted at angles of attack up to 61° with rocket-thrust coefficients varying from 0 to 5.8.

The results of the investigation show that the jet interference from the rocket exhaust increased the vehicle axial-force (drag) coefficient and generally decreased the static longitudinal stability at all Mach numbers. Jet impingement occurred on the lower surface of the command module and caused high local-pressure peaks at the higher angles of attack. The combined effects of rocket exhaust, angle of attack, and Mach number resulted in irregular variations in the aerodynamic characteristics of the Apollo launch-escape vehicle.

INTRODUCTION

Several investigations have been conducted to determine the static longitudinal aerodynamic characteristics of models of atmospheric abort configurations of proposed Apollo spacecraft (refs. 1 to 3, for example). All these investigations were made without simulation of the jet exhaust from the escape-rocket nozzles. An earlier investigation of a Mercury escape configuration with flow through the rocket exhaust indicated changes in the static stability at low angles of attack (ref. 4). The stability of a vehicle such as the Apollo with an escape rocket ahead of the command module would also be expected to change with the rockets firing. Information on the effect of the escape-rocket exhaust plumes on the static longitudinal aerodynamic characteristics of the Apollo launch-escape vehicle was therefore required for predicting abort trajectories.

---

*Title, Unclassified.

[redacted]

The first attempt to simulate the effect of the rocket-exhaust plumes on the aerodynamics of an Apollo abort vehicle utilized solid bodies to represent the predicted shapes of the jets. It was believed that this method did not produce adequate simulation of the actual rocket exhaust, and, in particular, completely excluded the effects of jet impingement on the command module which could occur at high angles of attack.

Test results of a rocket-powered 0.085-scale model of the Apollo launch-escape vehicle using the hot-jet simulation system of the Langley 16-foot transonic tunnel are reported herein. This system, using the decomposition products of hydrogen peroxide, provides properly scaled thrust values and good simulation of jet-interference effects including exhaust impingement. The tests were conducted at Mach numbers from 0.5 to 1.3 at angles of attack up to 61° over a thrust-coefficient range from 0 to a maximum of 5.8. The test Reynolds number based on a model base diameter of 33.25 centimeters and free-stream conditions varied from 2.95×10^6 to 4.38×10^6. Force data were obtained on the complete Apollo launch-escape-vehicle model and pressure distributions were measured on the command-module surfaces.

SYMBOLS

The positive direction of forces and moments is shown in figure 1. The basic data presented herein are referred to the body system of axes with the origin located at the theoretical apex of the command module.

Coefficients

Aerodynamic coefficients (include jet-interference effects but not the direct forces or moments produced by the jets):

C_A axial-force coefficients, $\frac{\text{Axial force}}{q_\infty A}$

C_D drag coefficient, $\frac{\text{Drag}}{q_\infty A}$

C_L lift coefficient, $\frac{\text{Lift}}{q_\infty A}$

C_m pitching-moment coefficient, $\frac{\text{Pitching moment}}{q_\infty A d}$

C_N normal-force coefficient, $\frac{\text{Normal force}}{q_\infty A}$

C_p pressure coefficient, $\frac{p_l - p_\infty}{q_\infty}$

Coefficients of force and moment components of jet thrust:

$C_{A,f}$ static axial-thrust coefficient, $\frac{(\text{Axial force})_j}{p_a A}$

$C_{A,j}$ thrust coefficient, $\frac{(\text{Axial force})_j}{q_\infty A \cos 35^\circ}$

C_j resultant thrust coefficient, $\frac{C_{A,f}}{\cos \theta}$ or $\frac{C_{A,j} \cos 35^\circ}{\cos \theta}$

$C_{m,f}$ static pitching-moment coefficient, $\frac{(\text{Pitching moment})_j}{p_a A d}$

$C_{m,j}$ pitching-moment coefficient, $\frac{(\text{Pitching moment})_j}{q_\infty A d}$

$C_{N,f}$ static normal-force coefficient, $\frac{(\text{Normal force})_j}{p_a A}$

$C_{N,j}$ normal-force coefficient, $\frac{(\text{Normal force})_j}{q_\infty A}$

Coefficients with aerodynamic and thrust components included:

$C_{A,t}$ total axial-force coefficient, $C_A - C_{A,j} \cos 35^\circ$

$C_{m,t}$ total pitching-moment coefficient, $C_m + C_{m,j}$

$C_{N,t}$ total normal-force coefficient, $C_N + C_{N,j}$

Other Symbols

A maximum cross-sectional area of command module, m^2

A_e nozzle exit area, cm^2

A_t nozzle throat area, cm^2

d maximum diameter of command module, cm

l length of command module, cm

M Mach number

p	pressure, N/m^2
p_j	rocket-chamber pressure, N/m^2
q	dynamic pressure, N/m^2
R	gas constant
r	radius, cm
V	velocity, m/s
T	total temperature, ^{o}K
x	axial distance, cm
α	angle of attack of model center line, deg
γ	ratio of specific heats
θ	angle between model center line and thrust axis, deg
ϕ	angular location of orifice with respect to module axis (see fig. 10), deg

Parameters

C_{m_α}	static-longitudinal-stability parameter, $\frac{\partial C_m}{\partial \alpha}$ at $\alpha = 0^o$, per deg
C_{N_α}	normal-force-curve slope, $\frac{\partial C_N}{\partial \alpha}$ at $\alpha = 0^o$, per deg

Subscripts

a	ambient
f	static thrust
j	jet
l	local

t	total
∞	free stream
max	maximum

APPARATUS AND PROCEDURE

Wind Tunnel

This investigation was conducted in the Langley 16-foot transonic tunnel, which is an atmospheric wind tunnel with an octagonal slotted test section and a continuous air exchange which allows testing of propulsion models.

Propellant Supply System

The propellant supply system consisted of a hydrogen peroxide (H_2O_2) storage and pumping trailer, a cryogenic nitrogen tank farm, nitrogen vaporizer unit and high-pressure gas-storage bottle field, and a propellant pressurizing and flow control trailer. The high-pressure H_2O_2 supply-system trailer, shown in the photographs of figure 2, had a 0.38-cubic-meter cylindrical stainless-steel tank which was capable of providing an H_2O_2 flow rate of 6.80 kg/sec at a pressure of 2068 N/cm^2. The propellant flow rate was set by the tank pressure and a remotely controlled throttling valve.

Model

General description.- A sketch of the 0.085-scale model of the Apollo launch-escape vehicle including some of the major dimensions is shown in figure 3. A closeup photograph of the model is presented in figure 4 and a photograph of the model mounted on the support system in the 16-foot transonic tunnel test section is shown in figure 5. This picture shows the sting-support system with a 45° bent knuckle adapter which permitted testing in the angle-of-attack range from about 45° to 61°. Four different bent-knuckle adapters were required to cover the angle-of-attack range; the angle-of-attack ranges covered by the respective knuckles were -5° to 11°, 15° to 31°, 30° to 45°, and 45° to 61°.

Propulsion system.- Liquid H_2O_2 was brought through the sting-support system and into the model by two stainless-steel propellant lines (fig. 6). Within the command module, the lines were formed into concentric right- and left-hand helices around the strain-gage force balance. This installation provided the flexibility required in bringing the lines across the force balance so that there was minimum restraint and thus minimum reduction in balance sensitivity. Further, the helices reduced to an insignificant level

the tare loads on the balance due to pressurization. From the helical coils, the H_2O_2 was fed into a plenum chamber from which it was passed through the four tower legs into the gas generator within the rocket-motor casing.

The small scale of the model, together with the high propellant flow rates required, posed unique design problems for an H_2O_2 rocket. Conventional axial-flow catalyst arrangements for decomposing H_2O_2 (as described in ref. 5) could not be used because of the high bed loadings (ref. 6). For the present model, the liquid propellant would have to flow forward through an internal catalyst, be decomposed into a gas which then must reverse direction to flow rearward out of the nozzles. Allowing for a reasonable gas passage, an axial-flow catalyst would have a bed loading about 20 times higher than the normal value. Since erosion, short operational life, and probably incomplete decomposition would make such a configuration impractical, a new approach was developed. A radial flow decomposition chamber was designed as shown in figure 7. An important feature of this design is the solid conical rod centered in the injector tube which acts to equalize the liquid pressure along the entire length of the catalyst pack and thus insures uniform flow. With this design, the catalyst bed would provide up to 30 minutes of firing time before failure. Failures were not due to the usual deterioration of the silver catalyst pack but were caused by compression and eventual separation of the individual packs from the spacer disks as a result of thermal cycling. A photograph of catalyst beds used in the investigation is shown in figure 8.

As shown in the upper sketch of figure 7, the decomposed H_2O_2 flowed rearward in the rocket-motor casing through an annular passage and into a gas plenum chamber. The gas was then exhausted through four nozzles which were canted 35° from the rocket-motor center line. All four nozzles had divergence half-angles of 17.5°. The two nozzles in the yaw plane had equal throat areas and equal exit-area ratios of 8.59. The upper nozzle in the pitch plane had a smaller throat area and a larger exit-area ratio of 10; the lower nozzle in the pitch plane had a larger throat area and smaller exit-area ratio of 7.62. The asymmetric thrust of the nozzles in the pitch plane provides the offset thrust vector ($2^{\circ}45'$) shown in figure 1.

During a later phase of the investigation, the aerodynamic characteristics of the launch-escape vehicle were obtained at thrust coefficients corresponding to the tail-off burning period of the full-scale rocket motor. At the low flow rates required for these conditions, the full-length catalyst bed performed erratically and made setting and controlling chamber pressures very difficult. For these tests the decomposition bed was shortened by omitting about 15 cm of the catalyst at the forward end of the pack. This configuration provided satisfactory thrust characteristics at low values of thrust coefficients. Static thrust calibrations of the launch-escape-rocket model for both types of catalyst configurations are presented in figure 9.

Rocket-Exhaust Simulation

Jets exhausting near adjacent surfaces have been found to produce appreciable effects on the surface pressures and temperatures and on the vehicle aerodynamics and stability. It was expected, therefore, that the exhausts from the launch-escape rocket could affect the stability and loading characteristics of the command-module abort system due both to blockage of the free-stream flow by the jet plumes and to actual impingement of the jet on the surface of the capsule. In the present case, where the downstream portion of the jets may influence the aerodynamic characteristics of the vehicle, simulation parameters affecting the jet penetration into the free-stream flow and the jet mixing with the free stream need to be considered (refs. 7 and 8). In addition the scaled jet thrust is desired to produce the proper reaction on the model aerodynamic and stability characteristics.

The model rocket nozzles had scaled throat areas A_t and exit areas A_e and the same expansion ratios A_e/A_t as the full-scale rocket nozzles and thus kept both external and internal geometric similarity. The ratio of specific heats γ for the H_2O_2 simulating exhaust ($\gamma = 1.265$) was close to that of the solid-propellant rocket ($\gamma = 1.23$). The resulting thrust-simulation parameter (ref. 8) for matched stream conditions and jet-pressure ratios gave values of $\gamma_j M_j^2$ of 15.3 and 14.0 for the model and full-scale vehicles, respectively. Presentation of data in terms of thrust coefficient $\left(C_{A,j} = \text{Thrust}/q_\infty A\right)$ provides good approximations of the jet effects on the Apollo launch-escape vehicle.

In addition to thrust simulation, the duplication of jet-boundary shape is desired. With the same divergence angle as that of the full-scale nozzle, the exit static-pressure ratio p_j/p_∞ along with γ_j and M_j determine the initial plume-shape similarity. Moreover, to meet the objectives of the present type of investigation, the downstream jet shaping is equally important. Matching the mixing boundary shape may be possible with simulation of (RT) of the full-scale rocket (ref. 8). Although the decomposition products of H_2O_2 have RT values of less than 40 percent of the high-temperature full-scale rocket, this exhaust provides very much better simulation of downstream boundaries than that obtainable with cold air. Additional compromises in nozzle geometry would also be required to obtain simulation of initial jet shape with air.

Instrumentation

Total forces and moments on the Apollo launch-escape vehicle were measured with a three-component strain-gage balance installed in the command module. Static-pressure orifices were located in the rocket chamber, at the base of the rocket, and on the forward-facing conical surface and base of the command module. The pressure-orifice locations are shown in figure 10. Pressures were measured with electrical

pressure transducers. Liquid hydrogen-peroxide propellant flow was measured with an impeller electronic flowmeter. The signals from the balance, pressure transducers, and the flowmeter were converted to dc millivolts and recorded on magnetic tape. The rocket-chamber pressure was also observed visually on a millivolt meter in order to set rocket-chamber pressure and vary thrust coefficient.

TESTS

Static rocket-thrust calibrations were conducted with a shroud around the command module to prevent any jet forces on the module. The variation of axial force, normal force, and pitching moment due to components of the static thrust are given in figure 9. Wind-tunnel measurements of force and pressure data were obtained at Mach numbers from 0.5 to 1.3 at angles of attack up to 61°. Thrust coefficient $C_{A,j}$ was varied from 0 to about 5.8 depending upon Mach number. The maximum rocket-chamber pressure achieved was about 1120 N/cm^2. Tests conducted at high values of thrust coefficients with the rocket-chamber configuration shown in figure 7 covered an angle-of-attack range up to 61°, while those made with the shortened catalyst bed were run at angles of attack from 0 to 31°.

The test runs were made by first setting Mach number and angle of attack and then taking data through a range of chamber-pressure ratios from 1 (jets off) to the maximum. In the course of operating the rocket through the cycle, tunnel Mach number varied somewhat, particularly at supersonic speeds. For example, where data is presented at a nominal value of $M = 1.3$ some of the test points may actually be at Mach numbers that are as low as 1.27.

RESULTS

The results of the investigation are presented in the following figures:

	Figure
Variation of thrust coefficient with Mach number	11
Variation of total force and moment coefficient with thrust coefficient	12 and 13
Variation of total force and moment coefficient with angle of attack	14 and 15
Variation of axial-force coefficient with thrust coefficient	16
Variation of normal-force coefficient with thrust coefficient	17
Variation of pitching-moment coefficient with thrust coefficient	18
Variation of axial-force coefficient with angle of attack	19
Variation of normal-force coefficient with angle of attack	20
Variation of pitching-moment coefficient with angle of attack	21
Variation of lift coefficient with angle of attack	22

Figure

Variation of drag coefficient with angle of attack 23
Variation of total axial-force coefficient at zero angle of attack with Mach number 24
Variation of total normal-force-curve slope with Mach number 25
Variation of total static-longitudinal-stability parameter with Mach number . . . 26
Pressure distributions and loading on command module . . . . . 27 to 30

DISCUSSION

Total Forces and Moments

With the escape-rocket jets not operating, the balance recorded the aerodynamic characteristics of the Apollo launch-escape vehicle. With the rocket operating, the balance measured both the rocket thrust forces and moments, and the aerodynamic forces and moments on the vehicle; the corresponding data have been designated total force and moment coefficients.

The thrust-coefficient variation with chamber pressure obtained in the tunnel over the test Mach number range is shown on figure 11. For a given chamber-pressure ratio, the thrust coefficient decreases with increasing Mach number for two reasons: One, chamber pressure, and thus thrust decreases, and two, dynamic pressure increases. For example, at a given p_j/p_∞, thrust at $M = 0.50$ is about 2.3 times that at $M = 1.3$, while q is only 0.35 as great.

The total force- and moment-coefficient variation with thrust coefficient for a Mach number of 0.50 is presented in figure 12. Jet-off and low thrust-coefficient values show positive axial force. The thrust overcomes the aerodynamic axial force at thrust coefficients between 0.4 and 0.8 and higher values of thrust coefficient would produce forward acceleration (fig. 12(a)). Normal-force coefficient generally increases with thrust coefficient (fig. 12(b)) due to an increasing component of the thrust, $C_{N,j}$ (fig. 1), and the pitching moment generally becomes more positive except for some reversal at higher values of α and low values of $C_{A,j}$ (fig. 12(c)). Generally similar trends of the axial-force data occur at the highest Mach number (fig. 13(a)). Total normal-force coefficient at $M = 1.3$ and $\alpha = 0^\circ$ (fig. 13(b)) increases with $C_{A,j}$ as at $M = 0.50$ but at a slower rate. With increasing α up to 45°, $C_{N,t}$ generally stays relatively constant with increasing $C_{A,j}$ but at $\alpha = 61^\circ$ the effects of thrust are reversed and $C_{N,t}$ decreases. The total pitching-moment coefficient at $M = 1.3$ (fig. 13(c)) also shows the destabilizing effect of the rocket except in an angle-of-attack range from about 31° to 45° where the effects are either negligible or slightly stabilizing.

Cross plots at constant values of thrust coefficient from figures 12 and 13 are presented in figures 14 and 15, respectively, to illustrate the variation in total force and moment coefficients with angle of attack for constant values of $C_{A,j}$. The expected aerodynamic decrease in axial-force coefficient with increasing angle of attack is generally consistent at all values of thrust coefficient (figs. 14(a) and 15(a)). Total normal-force coefficients had similar increasing trends with increasing angle of attack for all thrust coefficients at $M = 0.50$ (fig. 14(b)) but showed decreasing slopes at the highest angles of attack at $M = 1.30$ (fig. 15(b)). With the jets off, the vehicle was stable over a relatively small range of angles of attack. At the lowest Mach number the action of the jet exhaust at lower values of $C_{A,j}$ increased the angle-of-attack range over which the vehicle was stable, but at higher thrust coefficients the angle-of-attack range for positive stability was decreased. At a Mach number of 1.30, operation of the rocket jets extended the stable range of angle of attack approximately 15° for all values of thrust coefficient. The two examples of total coefficients presented in figures 14 and 15 are typical of data obtained in the low and high Mach number ranges.

Aerodynamic Force and Moment Coefficients

The aerodynamic coefficients were obtained from the total coefficients by removing the applicable components of the jet thrust. Therefore these coefficients represent the aerodynamic characteristics of the vehicle in the presence of the flow field as altered by the exhaust plumes. Comparing these data with results obtained without exhaust simulation indicates the magnitude of the jet-interference effects on the vehicle aerodynamics.

The variation of force and moment coefficients with thrust coefficient is presented in figures 16 to 18 for the range of test Mach numbers. For some ranges of thrust coefficient at the higher angles of attack, complete data coverage was not obtained and extrapolations are indicated by dashed lines. Variation of force and moment characteristics with angle of attack are presented in figures 19 to 21.

Variation of axial-force coefficient with thrust coefficient.- The effect of varying thrust coefficient on the axial-force coefficients presented in figure 16 indicates that the escape-rocket jets would produce an unfavorable interference on the launch-escape-vehicle acceleration during an abort. For every level of rocket-thrust coefficient, the axial-force coefficient was increased at all angles of attack and Mach numbers over the range of jet-off axial-force values. Generally the largest interference effect occurs at the maximum thrust coefficient with some small exceptions in the moderate angle-of-attack range. The rate of increase in C_A with thrust coefficient varies both with angle of attack and Mach number. In some cases the increase in axial force reaches a maximum value at low thrust coefficients and remains nearly constant with increasing thrust (for example, at $M = 0.50$, fig. 16(a)), whereas in others there is a continuous increase

to the maximum value of thrust coefficient, particularly at the highest angle of attack for $M = 0.90$.

Variation of normal-force coefficient with thrust coefficient.- The effect on normal-force coefficient of increasing thrust coefficient varies irregularly with Mach number and angle of attack (fig. 17). Generally, the overall trends are small and in a negative direction with some exceptions at the higher angles of attack. For example, at $M = 0.70$, C_N increases moderately with increasing $C_{A,j}$ above $\alpha = 31^{\circ}$, whereas, at higher Mach numbers C_N decreases moderately, particularly at $\alpha = 61^{\circ}$.

Variation of pitching-moment coefficient with thrust coefficient.- As might be expected, the variation of the pitching-moment coefficient with thrust coefficient is irregular as a result of the rocket free-stream flow-field interaction over the vehicle (see fig. 18). At the lowest speeds and angles of attack, generally small changes in pitching-moment coefficient resulted from increases in thrust coefficient. At angles of attack above about 20°, moderate increases in thrust coefficient produced initially more negative vehicle pitching-moment coefficients. Further increases in thrust coefficient generally caused a reversing trend toward more positive values of pitching-moment coefficient (for example, see figs. 18(a) and 18(b)). At the highest angle of attack ($\alpha = 61^{\circ}$) pitching-moment coefficient varies irregularly with thrust coefficient and maintains generally a large positive value.

Variation in axial-force coefficient with angle of attack.- The aerodynamic axial-force variation with angle of attack is presented in figure 19. For jet-off conditions $\left(C_{A,j} = 0\right)$, the aerodynamic axial force peaks at about a 10° angle of attack and then decreases with increasing angle of attack throughout the Mach number range. This variation in aerodynamic axial-force coefficient with angle of attack is similar to the results of reference 2 for a model with a rocket-nozzle fairing. With the jets operating, the axial force generally decreases continually with increasing angle of attack. At supersonic speeds the axial force decreases less rapidly with angle of attack with the jets operating than with the jets off. This decrease is apparently caused by the more positive pressure coefficient on the lower surface of the command module resulting from jet impingement, as can be seen in figure 28(c) and (d).

Variation of normal-force coefficient with angle of attack.- The jet-off variation of normal-force coefficient with angle of attack (fig. 20) also shows similarity to the data of references 1 and 2 with some increase in normal-force-curve slope occurring around 30° angle of attack. Jet-on normal-force curves are generally similar to the jet-off curves except for irregular changes in slope at some Mach numbers.

Variation of pitching-moment coefficient with angle of attack.- The variation of pitching moment with angle of attack for the Apollo launch-escape vehicle is characteristically nonlinear. (See fig. 21.) As indicated in reference 9, the nonlinearity results

from the wake of the escape-rocket case and tower structure disrupting the flow over the upper side of the command module as the angle of attack is increased. The pitching moment about the apex indicates that the vehicle is stable up to about a 40° angle of attack at $M = 0.50$ with jets off (fig. 21(a)). This stable region rapidly decreases with increasing Mach number until at $M = 1.3$ the launch-escape vehicle maintains stability only to about 11°. For center-of-gravity positions further aft than the apex, the present configuration would be even less stable. The model became abruptly unstable at subsonic Mach numbers at angles of attack around 40°. Similar trends are indicated for the atmospheric-abort configuration of reference 1.

The effect of the rocket exhausts on the pitching-moment coefficients of the Apollo launch-escape vehicle varies with thrust coefficient and Mach number over the angle-of-attack range. Most of the abrupt changes to unstable conditions (positive slope of the pitching-moment curves) occur between angles of attack of about 30° and 50° and indicate that the basic jet-off aerodynamics of the vehicle has the predominant effect on the stability. The rocket-jet exhausts do alter the variation in pitching-moment coefficient with angle of attack by changing the degree of stability, the amount of neutral stability, and the location of the unstable angle-of-attack range. Increases in rocket thrust to moderate values of thrust coefficients generally extend the stable angle-of-attack range of the vehicle at all Mach numbers. At low and moderate thrust coefficients, the point at which the system becomes abruptly unstable shifts to higher angles of attack with increasing thrust coefficient. For the higher values of thrust coefficient this trend reverses and the vehicle becomes unstable at successively lower values of angle of attack as the thrust coefficient is increased.

Lift and drag coefficients.- The variation of lift and drag coefficients with angle of attack are presented in figures 22 and 23, respectively, for the test Mach number range at jet-off conditions. Lift coefficient increases with angle of attack up to 5° and then falls off up to about 15° or 20° and then again increases at a lower rate with increasing angle of attack at all Mach numbers. The trends of drag coefficient with angle of attack are similar to those for the lift coefficient but the fall off after the initial increase starts at an angle of attack of about 10°.

Aerodynamic Parameters

The axial-force coefficient and the slopes of the normal-force-coefficient and pitching-moment-coefficient curves at zero angle of attack are presented in figures 24 to 26. These plots are shown to illustrate the effect of escape-rocket operation on these parameters; in practice, the magnitude of the thrust increment will vary with angle of attack and thrust coefficient. Axial-force coefficient is increased (up to 50 percent) and normal-force-coefficient slope is decreased (by as much as 68 percent) throughout the Mach number range due to maximum rocket thrust. The static-longitudinal-stability

parameter at zero angle of attack shows an increase in stability with increasing Mach number above $M = 0.7$ for the launch-escape vehicle with the escape rocket not thrusting. Maximum rocket thrust decreased the stability throughout the Mach number range with the stability about the command-module apex becoming almost neutral near Mach 1. As was pointed out earlier, the vehicle is very unstable at higher angles of attack.

Command-Module Pressure Distributions

Pressure distributions around the command module.- Figures 27 and 28 present typical pressure distributions over one side of the command module, from top to bottom, for Mach number 0.5 and 1.3. At zero angle of attack (figs. 27(a) and 28(a)) it would be expected that the effect of the rocket exhaust on the surface pressure would be greatest at $\phi = 0^{\circ}$, 90°, and 180° since these stations are directly behind the rocket nozzle exits. For jets-off conditions $\left(C_{A,j} = 0\right)$, pressure-distribution dissimilarities exist around the surface of the command module because of the interference of the tower-leg structure between the nozzle locations. At a Mach number of 0.5, the effect of the rocket exhaust at the lowest thrust coefficient initially is to increase the pressure on the forward surface of the command module. Further increases in thrust coefficient produce an aspirating effect in this region and thereby lower the pressure. The jet effect on the command-module pressures are similar regardless of orientation with respect to the nozzles, which indicates a substantial spreading of the jet plume at this speed as well as at $M = 1.30$ (fig. 28(a)). At moderate angles of attack (up to 31°), the pressure distributions vary with position, as the flow is complicated by effects of angle of attack, flow through and wake of the tower structure, the wake of the escape rocket, and the proximity of the jet-exhaust plume. At an angle of attack of 55° (fig. 28(d)) impingement of the exhaust plume on the lower surface of the command module is apparent.

Pressure distributions at $\phi = 180^{\circ}$.- The impingement effects of the rocket plume on the command module at $\phi = 180^{\circ}$, where maximum jet-interference effects would be expected at angle of attack, are further illustrated in figure 29. The effect of an increase in thrust coefficient at a subsonic Mach number of 0.5 can be seen in figure 29(a). Increasing thrust coefficient generally reduces the pressure coefficient uniformly up to an angle of attack of 40°. At angles of attack from 50° to 61°, increasing $C_{A,j}$ from 1.6 to 3.0 causes the impingement from the lower nozzle to move back on the command module because the higher momentum jet penetrates further into the airstream. At a $C_{A,j}$ of 5.8, the jet penetration into the stream is still greater and the plume boundary no longer impinges on the lower surface of the command module. Higher subsonic Mach numbers result in relatively less jet penetration for the same thrust coefficient so that impingement occurs at a lower angle of attack (for instance, see fig. 29(c) at $\alpha = 40^{\circ}$

and $C_{A,j} = 1.6$). The pressure distributions on the lower surface at supersonic speeds are similar to those at a Mach number of 0.90.

Peak pressures on the lower surface of the command module.- The maximum local pressures on the lower surface of the command module ($\phi = 180^{\circ}$) obtained from data similar to that shown in figure 29 are presented in figure 30. These peak loadings generally occurred at about the same angles of attack and thrust coefficients throughout the Mach number range, with the angles varying from 50° to 60° and for thrust coefficients near 1.6. Even though the jet-impingement point moves rearward on the command-module surface with increasing thrust coefficient at a constant Mach number and angle of attack, this rearward movement is counteracted by a forward movement of the impingement point as the angle of attack and Mach number are increased with the thrust coefficient held constant. The location of the peak pressure at $\phi = 180^{\circ}$ on the command module occurred between x/l of 0.5 and 0.7 for all Mach numbers. The maximum pressure of about 20 N/cm^2 occurs in the transonic speed region for the test range of the present investigation.

CONCLUDING REMARKS

An investigation has been conducted in the Langley 16-foot transonic tunnel to determine the effect of the escape-rocket exhaust on the aerodynamic and loading characteristics of the Apollo launch-escape vehicle. Data were obtained over a Mach number range from 0.5 to 1.3 at angles of attack up to 61° for escape-rocket thrust coefficients from 0 to 5.8. Although the effects of Mach number, angle of attack, and a forward-located multiple-nozzle exhaust flow all combined to produce somewhat irregular aerodynamic characteristics for the vehicle, the following general results from the investigation were observed:

The jet interference from the escape-rocket exhaust increased the vehicle axial-force (drag) coefficient at all Mach numbers.

Near zero angle of attack, the effect of rocket-jet operation decreased the vehicle stability at all Mach numbers. At higher angles of attack, the jet-interference effects were irregular and varied with Mach number and thrust coefficient. Increasing thrust coefficient to moderate values generally extended the stable angle-of-attack range at all Mach numbers.

Pressure-distribution measurements on the command module showed that jet impingement on the lower surface caused high local-pressure peaks at high angles of attack at all Mach numbers. The impingement point moves rearward with increasing thrust coefficient, but peak pressure locations on the bottom of the command module

occur within about the same general range of thrust coefficient and angle of attack at all Mach numbers.

Langley Research Center,
National Aeronautics and Space Administration,
Langley Station, Hampton, Va., October 26, 1965.

REFERENCES

1. Pearson, Albin O.: Wind-Tunnel Investigation of the Static Longitudinal Aerodynamic Characteristics of Models of Reentry and Atmospheric-Abort Configurations of a Proposed Apollo Spacecraft at Mach Numbers From 0.3 to 1.20. NASA TM X-604, 1961.
2. Pearson, Albin O.: Wind-Tunnel Investigation of the Static Longitudinal Aerodynamic Characteristics of a Modified Model of a Proposed Apollo Atmospheric-Abort Configuration at Mach Numbers From 0.30 to 1.20. NASA TM X-686, 1962.
3. Boisseau, Peter C.: Low-Speed Static and Oscillatory Stability Characteristics of a Model of the Apollo Launch-Escape Vehicle and Command Module. NASA TM X-894, 1963.
4. Johnson, Joseph L., Jr.: Wind-Tunnel Investigation at Low Subsonic Speeds of the Static and Oscillatory Stability Characteristics of Models of Several Space Capsule Configurations. NASA TM X-285, 1960.
5. Runckel, Jack F.; and Swihart, John M.: A Hydrogen Peroxide Hot-Jet Simulator for Wind-Tunnel Tests of Turbojet-Exit Models. NASA MEMO 1-10-59L, 1959.
6. Davis, N. S., Jr.; and McCormick, James C.: Design of Catalyst Packs for the Decomposition of Hydrogen Peroxide. [Preprint] 1246-60, American Rocket Soc., July 1960.
7. Huff, Ronald G.; and Abdalla, Kaleel L.: Mixing Characteristics Downstream of Core Region of High-Temperature Axisymmetric Jets Exhausting Into Transonic and Supersonic Streams. NASA TM X-151, 1960.
8. Pindzola, M.: Jet Simulation in Ground Test Facilities. AGARDograph 79, Nov. 1963.
9. Babcock, D. L.; and Wiltse, P. D.: Motor-Vehicle Interfaces in the Apollo Launch Escape System. Paper No. 65-152, Am. Inst. Aeron. Astronaut., Feb. 1965.

CONFIDENTIAL

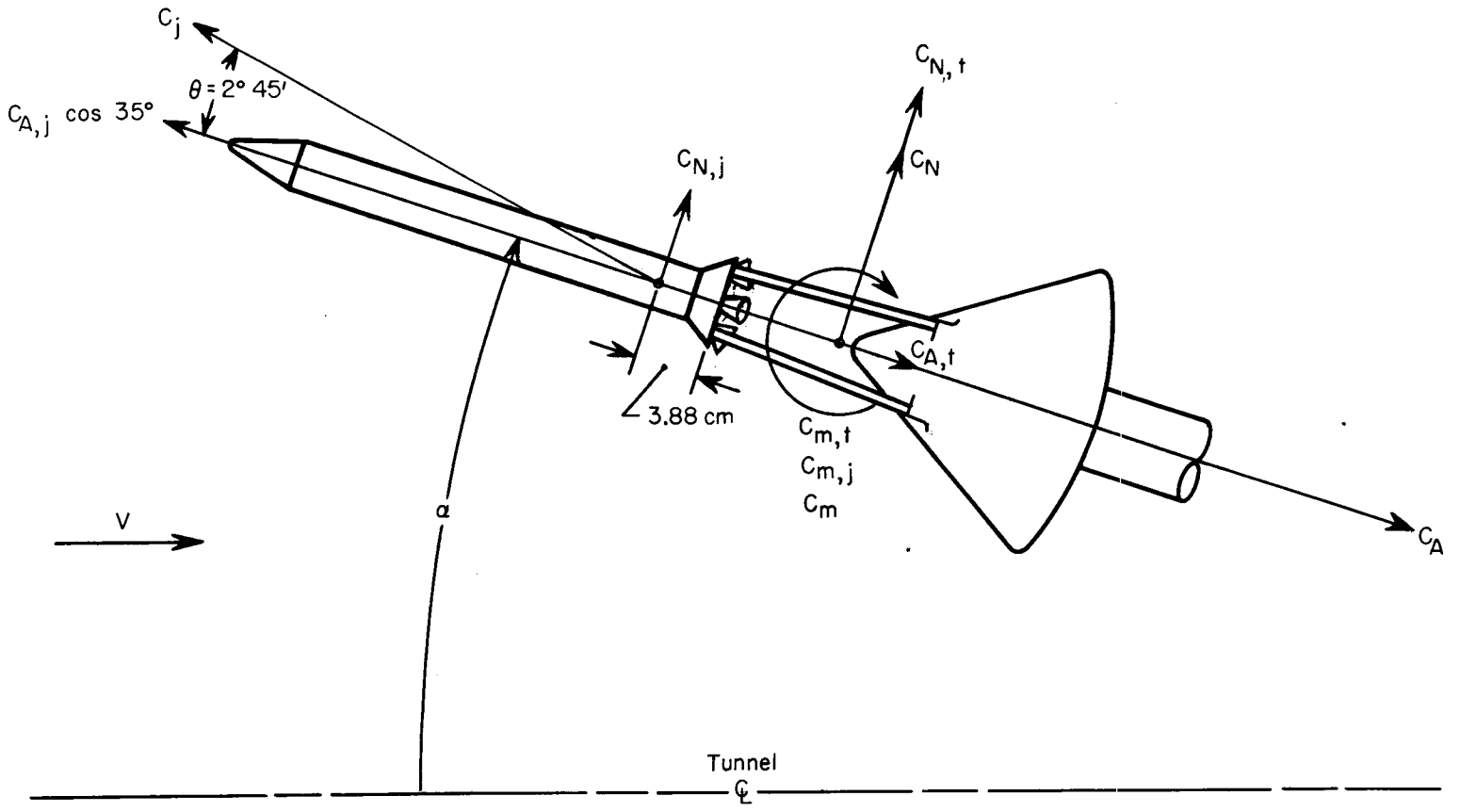

Figure 1.- Body system of axis. Force and moment coefficients on model including rocket thrust components. Arrows indicate positive direction.

CONFIDENTIAL

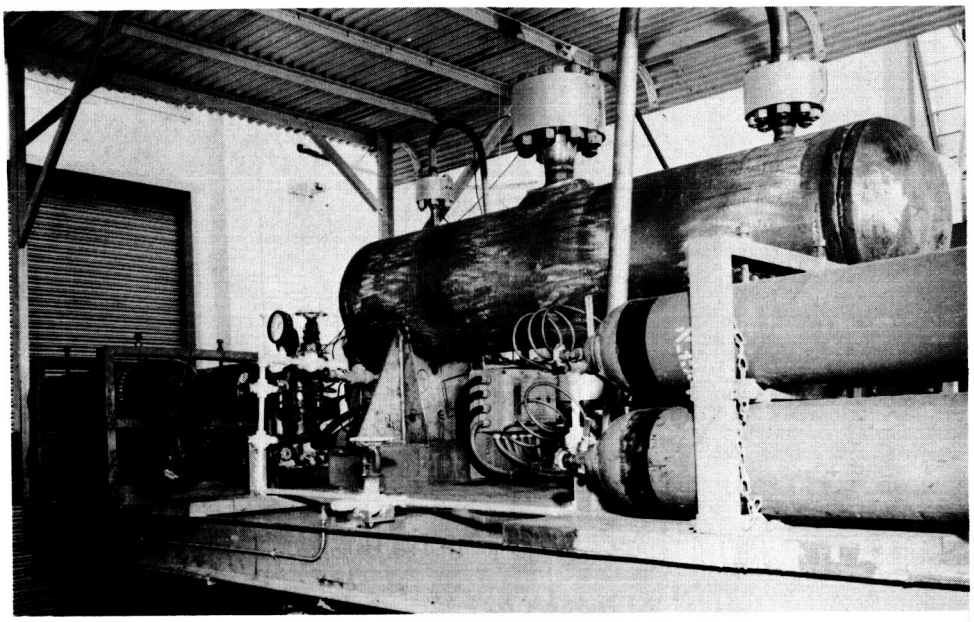

L-63-1541

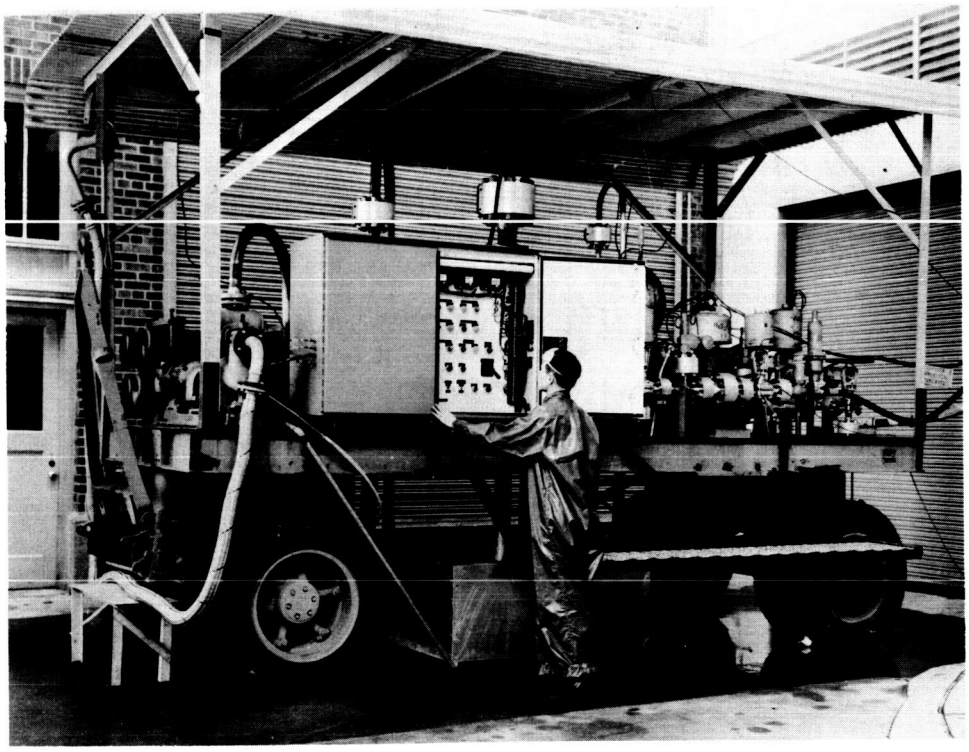

Figure 2.- Photographs of high-pressure hydrogen-peroxide supply system. L-63-1536

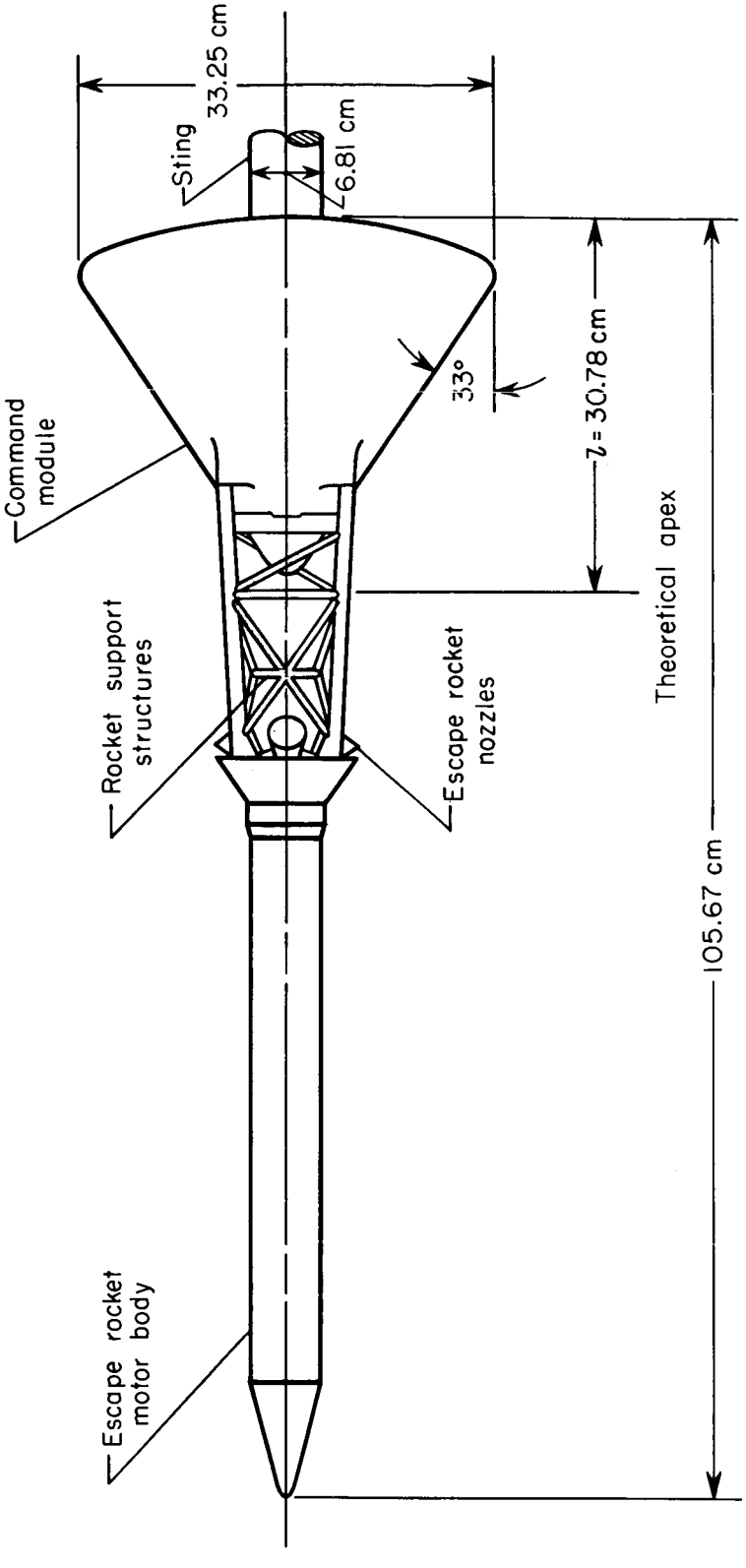

Figure 3.- Model sketch of Apollo launch-escape system.

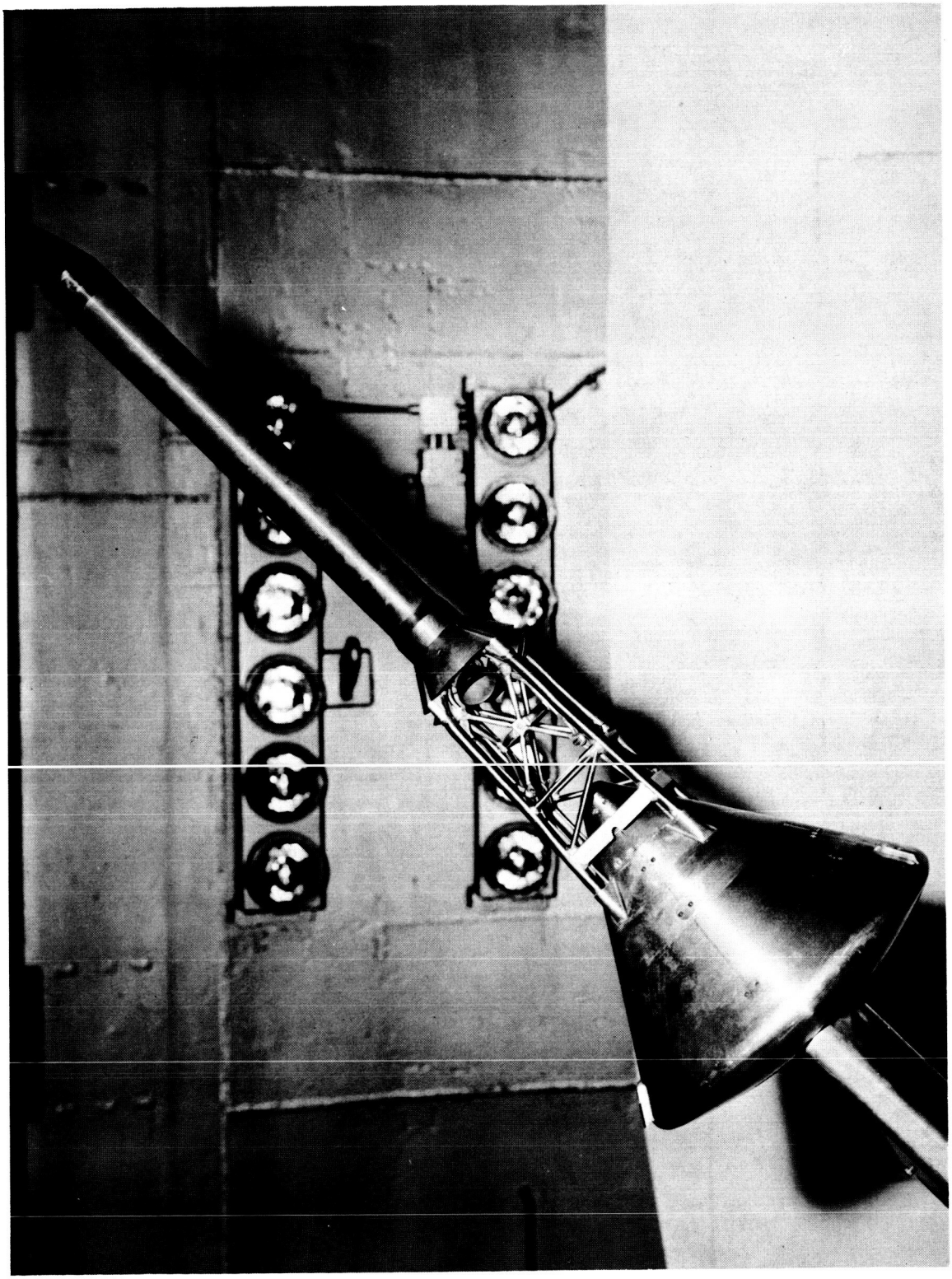

L-63-6171

Figure 4.- Photograph of Apollo launch-escape system.

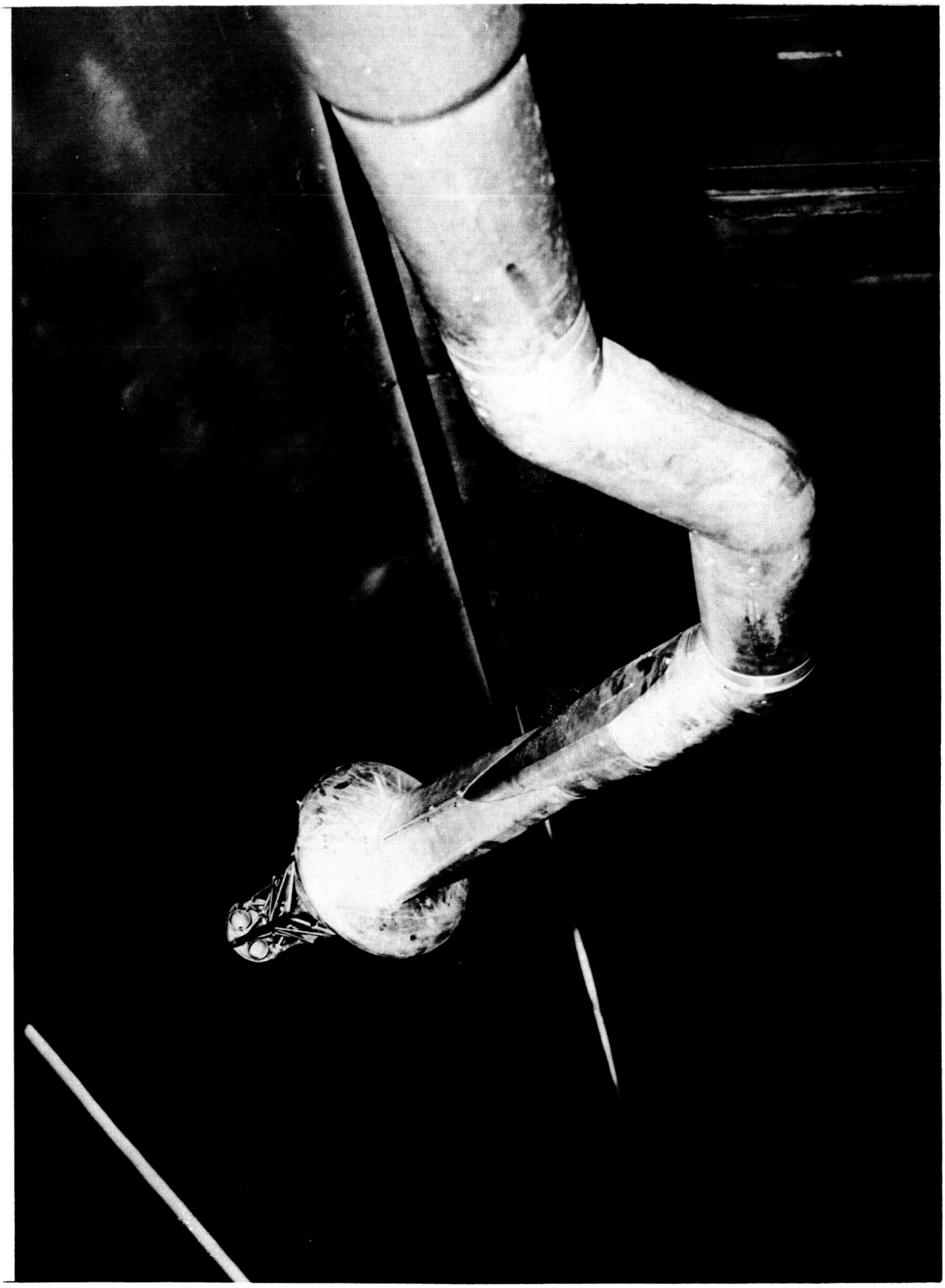

L-63-6170

Figure 5.- Model mounted on support system.

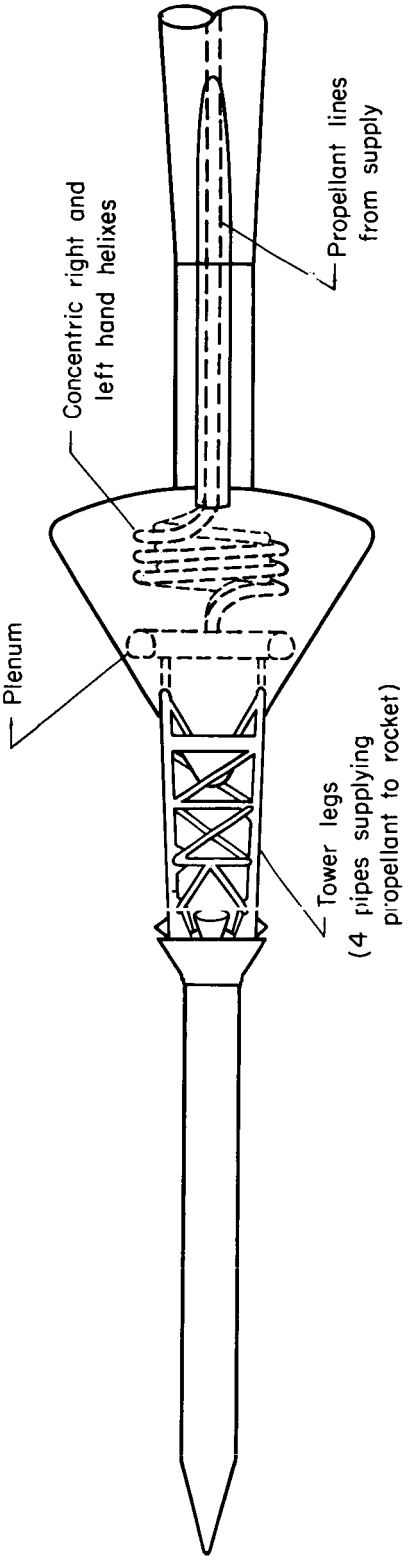

Figure 6.- Model drawing showing propellant lines.

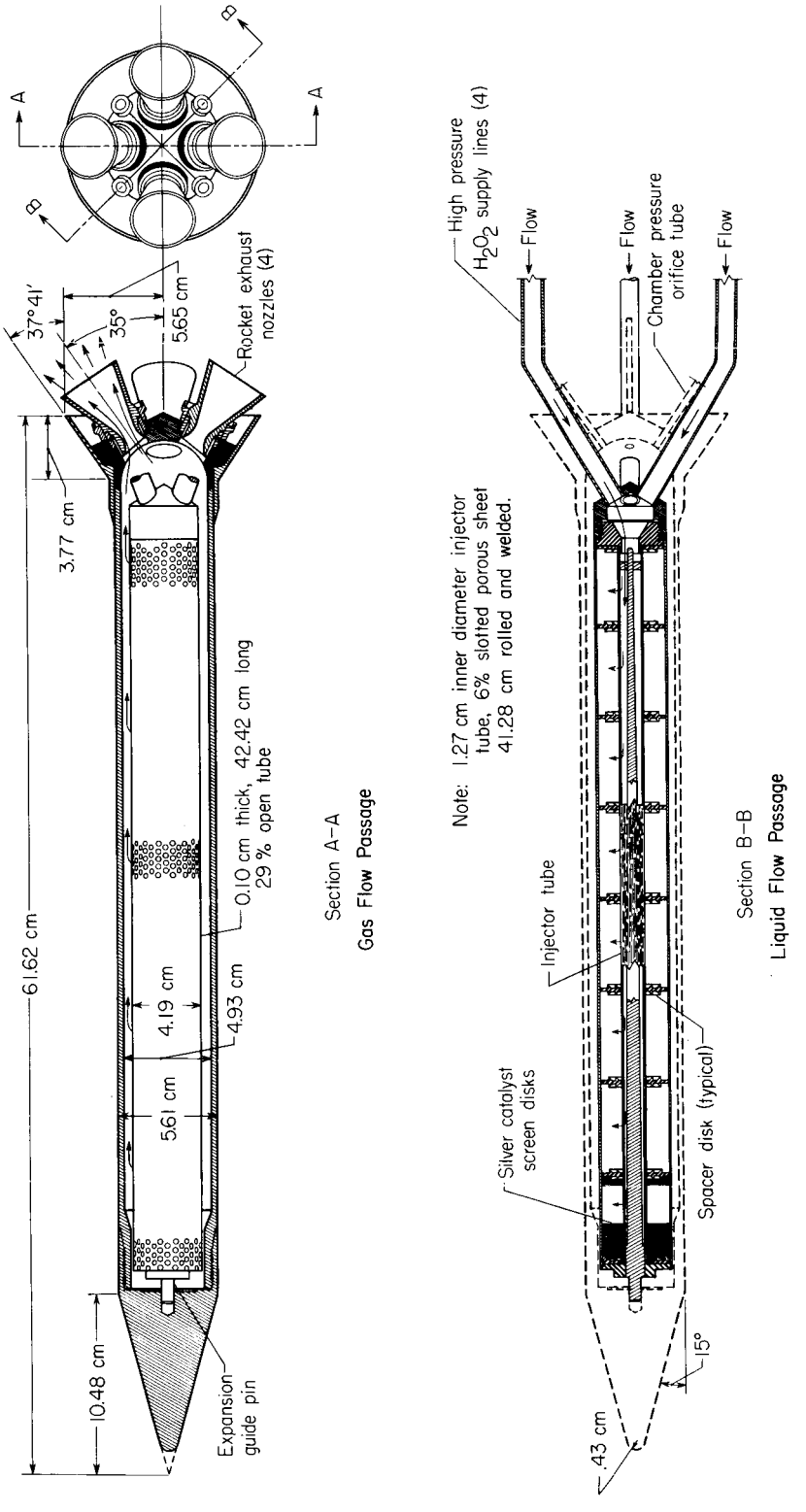

Figure 7.- Sketch of radial flow decomposition chamber.

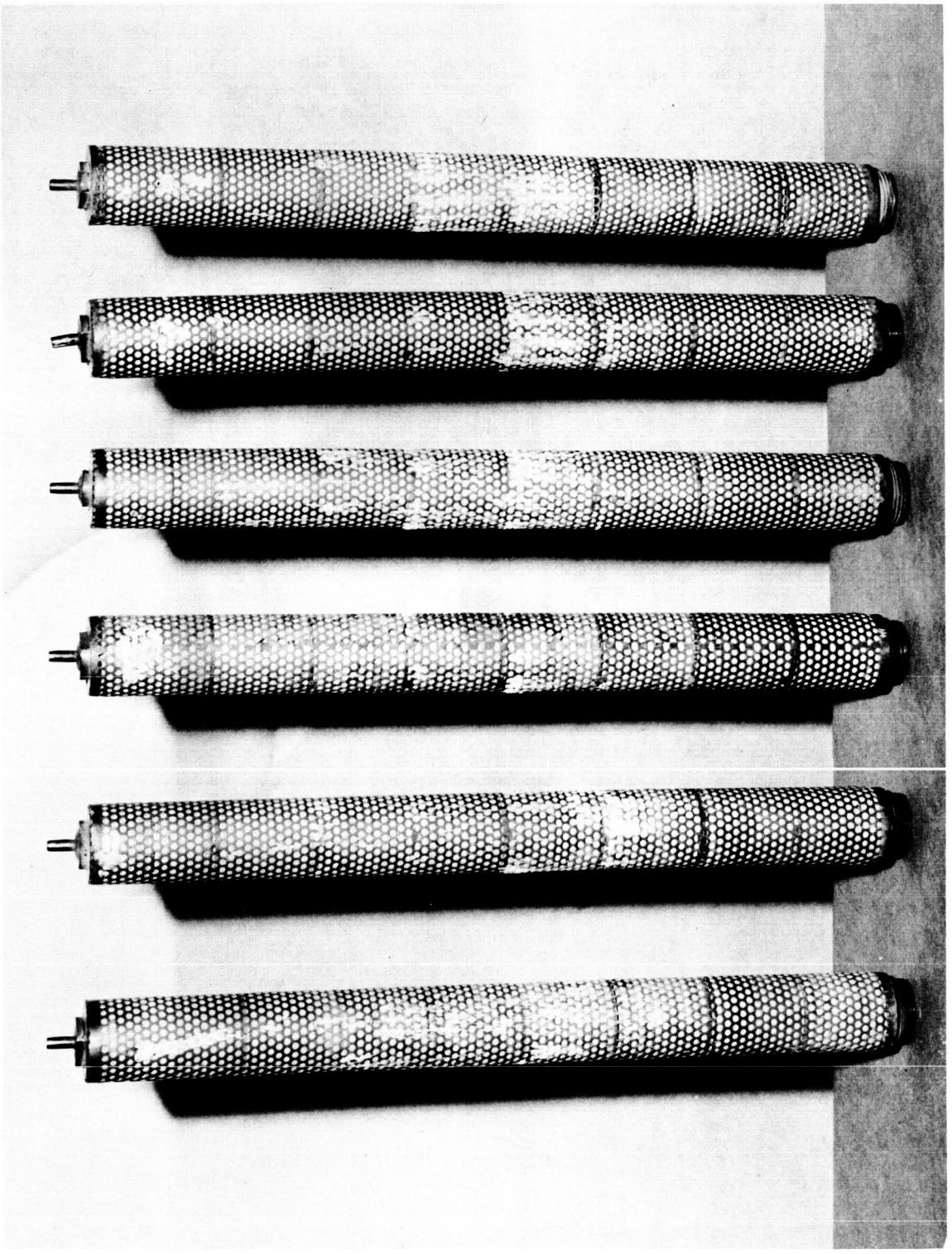

L-63-6169

Figure 8.- Photograph of catalyst packs.

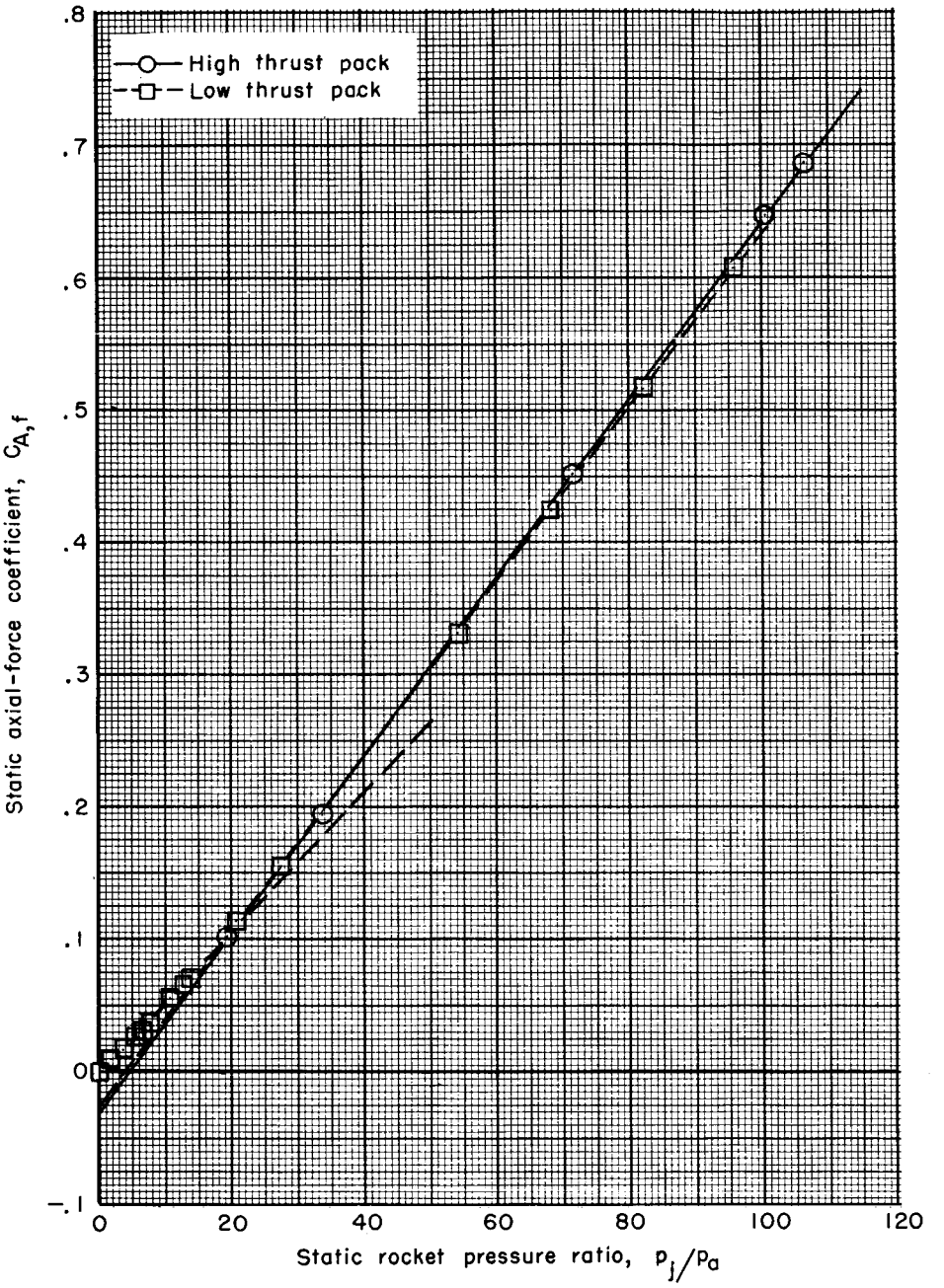

(a) Variation of axial-force coefficient with rocket-chamber-pressure ratio.

Figure 9.- Static thrust calibrations of launch-escape rocket model.

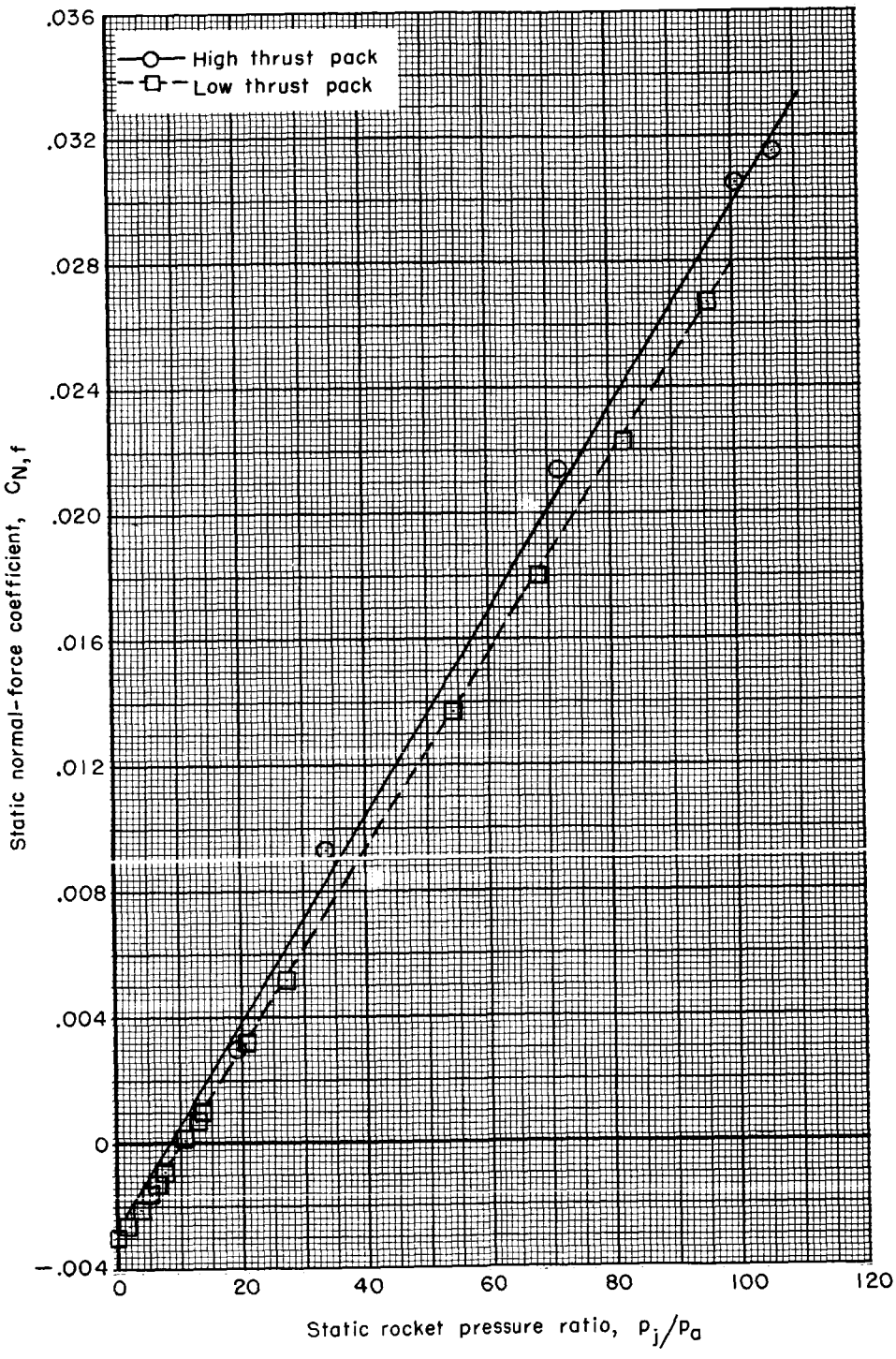

(b) Variation of normal-force coefficient with rocket-chamber-pressure ratio.

Figure 9.- Continued.

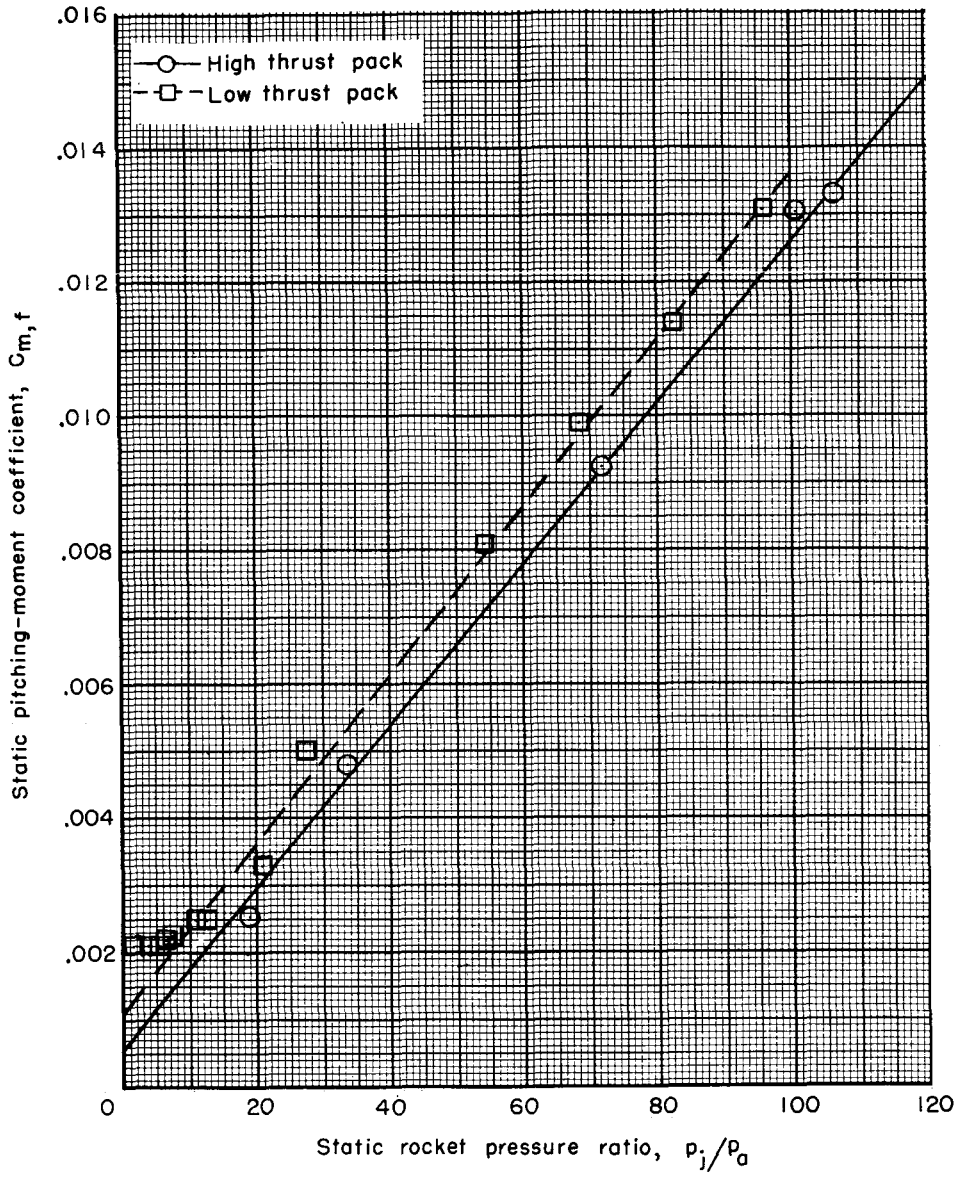

(c) Variation of pitching-moment coefficient about apex with rocket-chamber-pressure ratio.

Figure 9.- Concluded.

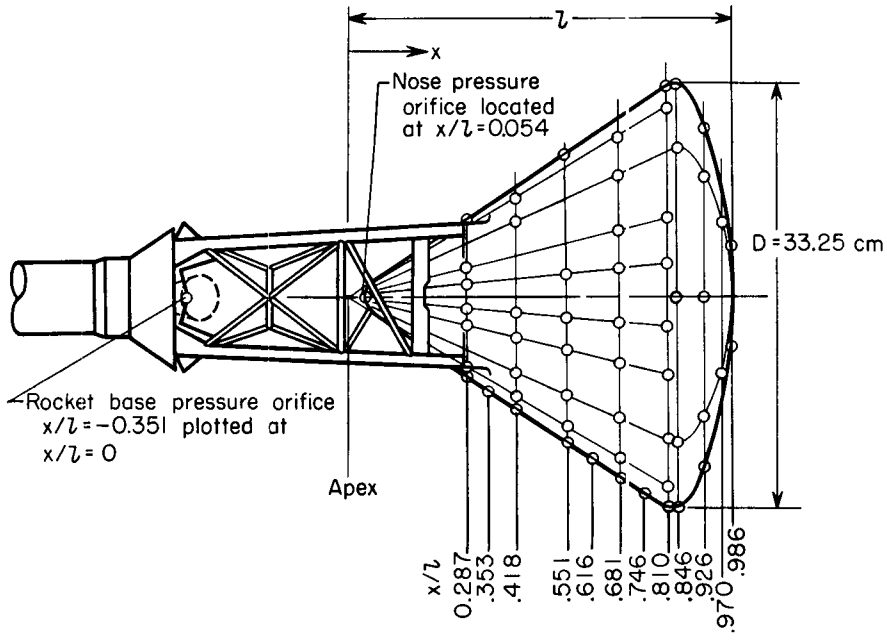

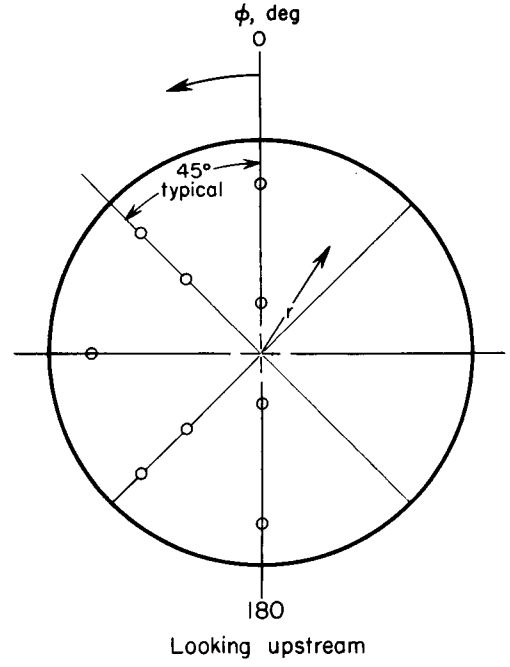

x/l	ϕ, deg	Remarks	r/d_{max}	x/l	ϕ, deg	Remarks	r/d_{max}
−0.351		Rocket base		.681	22.5, 45, 67.5, 82.5, 97.5, 112.5, 135, 157.5, 180	Conical surface	
.054		Conical surface nose		.746	180		
.287	0, 67.5, 82.5, 97.5, 112.5, 157.5, 180	Conical surface		.810	0, 22.5, 67.5, 82.5, 97.5 112.5, 135, 157.5, 180		
.353	180			.846	0, 45, 90, 135, 180	Conical surface (max. diam.)	0.50
.418	22.5, 45, 97.5, 112.5 135, 157.5, 180			.926	0, 45, 90, 135, 180	Base	.40
.551	0, 82.5, 97.5, 112.5 135, 157.5, 180			.970	45, 135		.25
.616	180			.986	0, 180		.12

Figure 10.- Pressure-orifice locations.

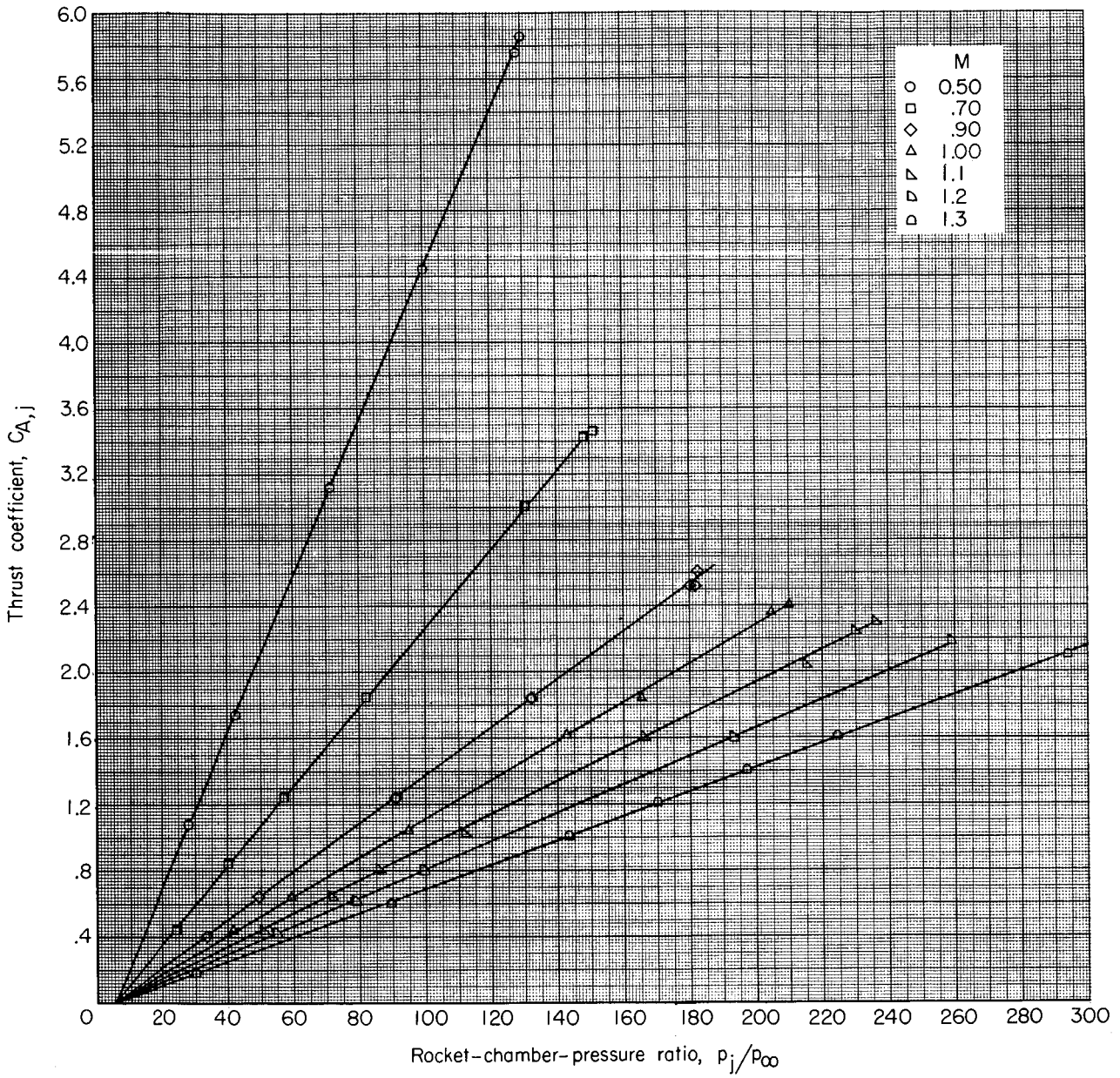

Figure 11.- Variation of thrust coefficient with Mach number and chamber-pressure ratio.

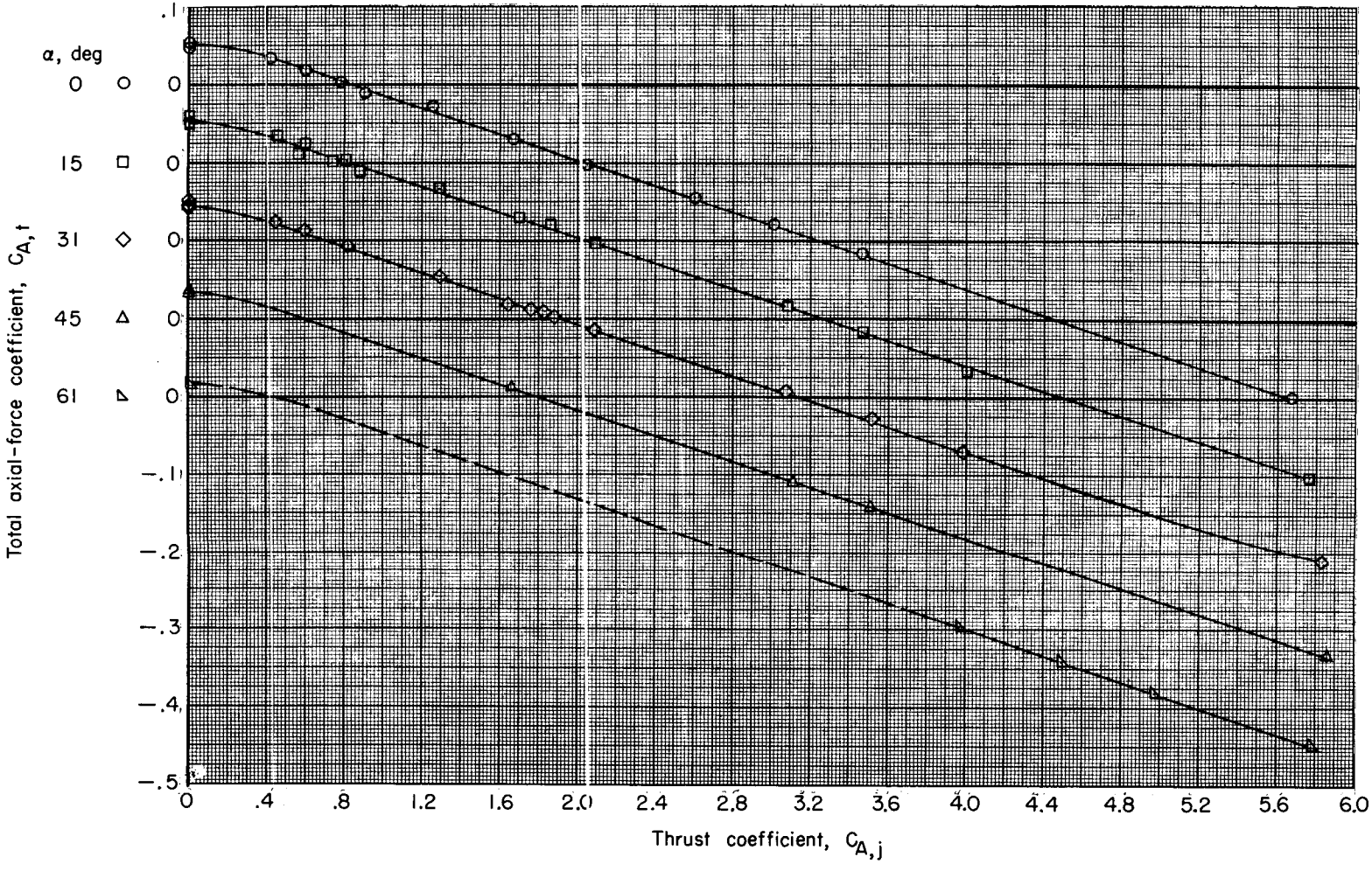

(a) Total axial-force coefficient.

Figure 12.- Variation of total force and moment coefficient with thrust coefficient. M = 0.5.

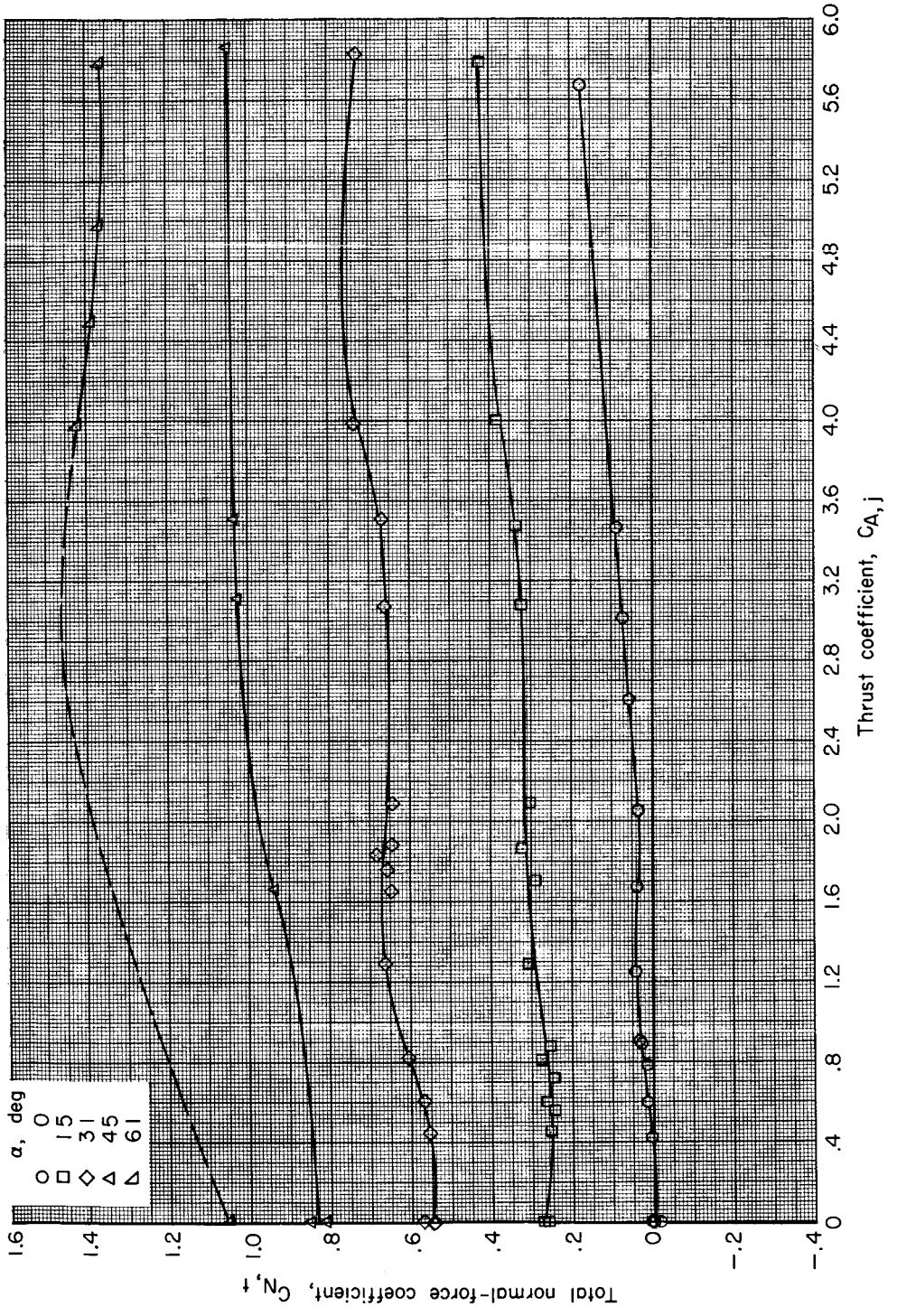

(b) Total normal-force coefficient.

Figure 12.- Continued.

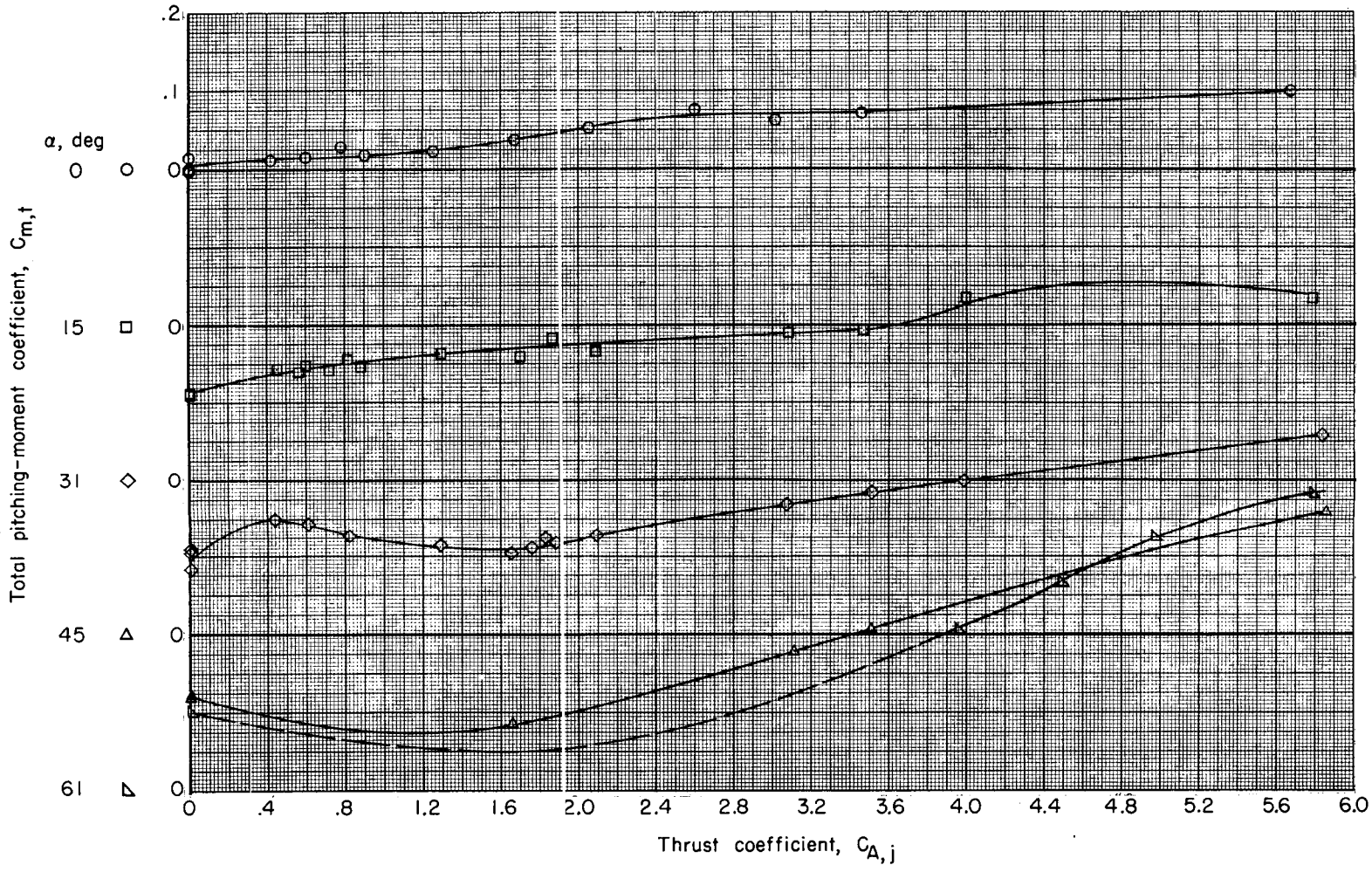

(c) Total pitching-moment coefficient.

Figure 12.- Concluded.

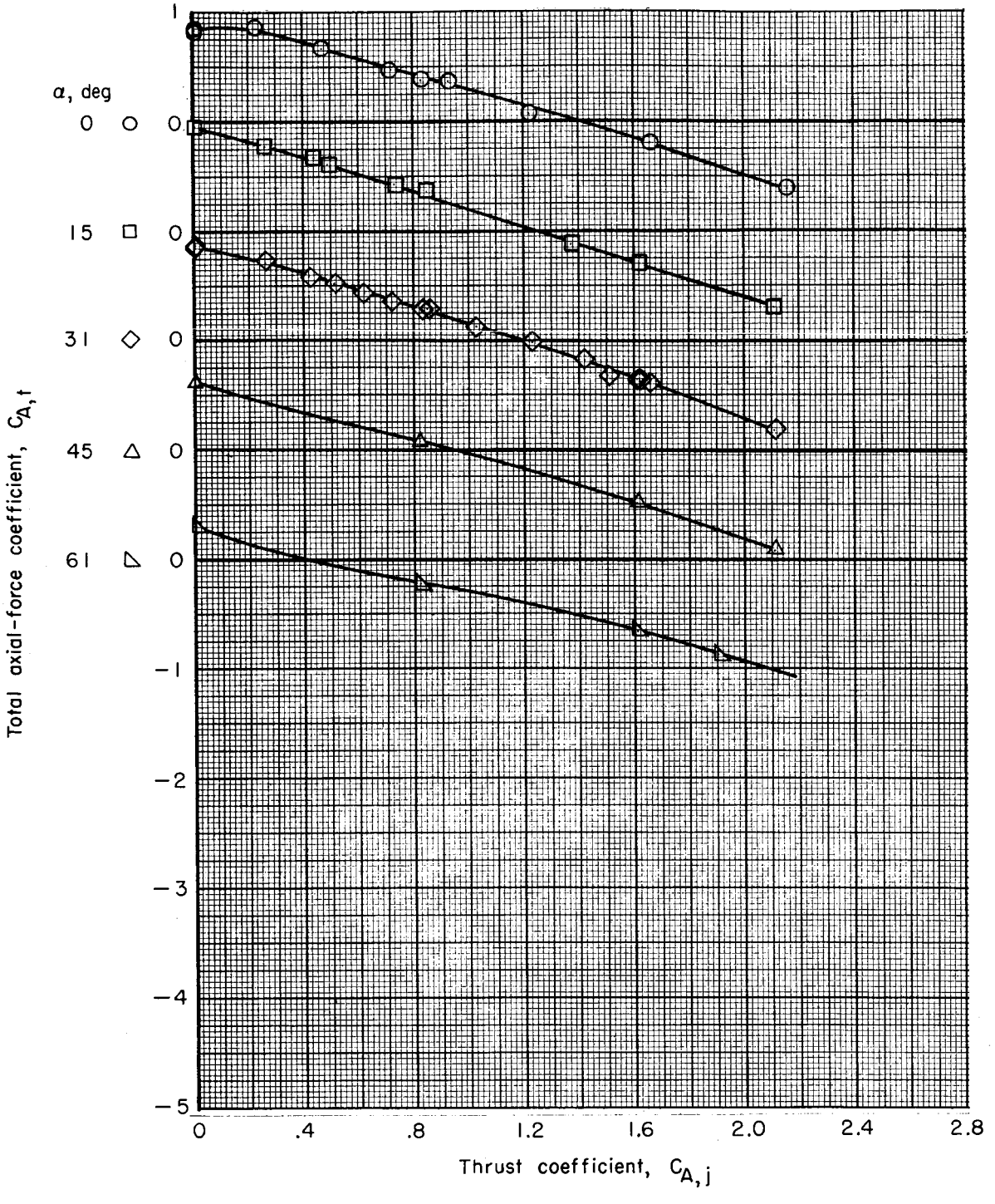

(a) Total axial-force coefficient.

Figure 13.- Variation of total force and moment coefficient with thrust coefficient. $M = 1.3$.

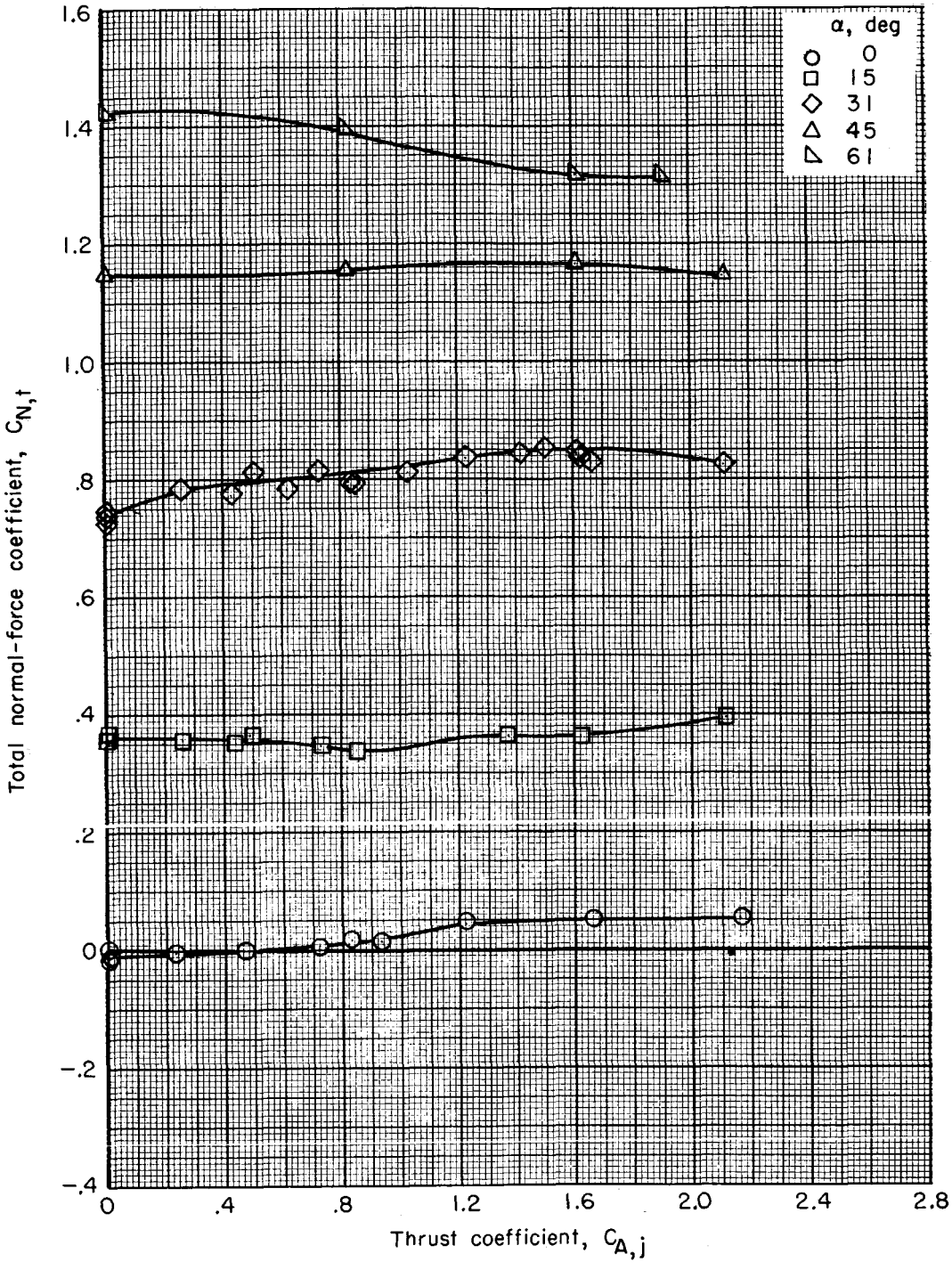

(b) Total normal-force coefficient.

Figure 13.- Continued.

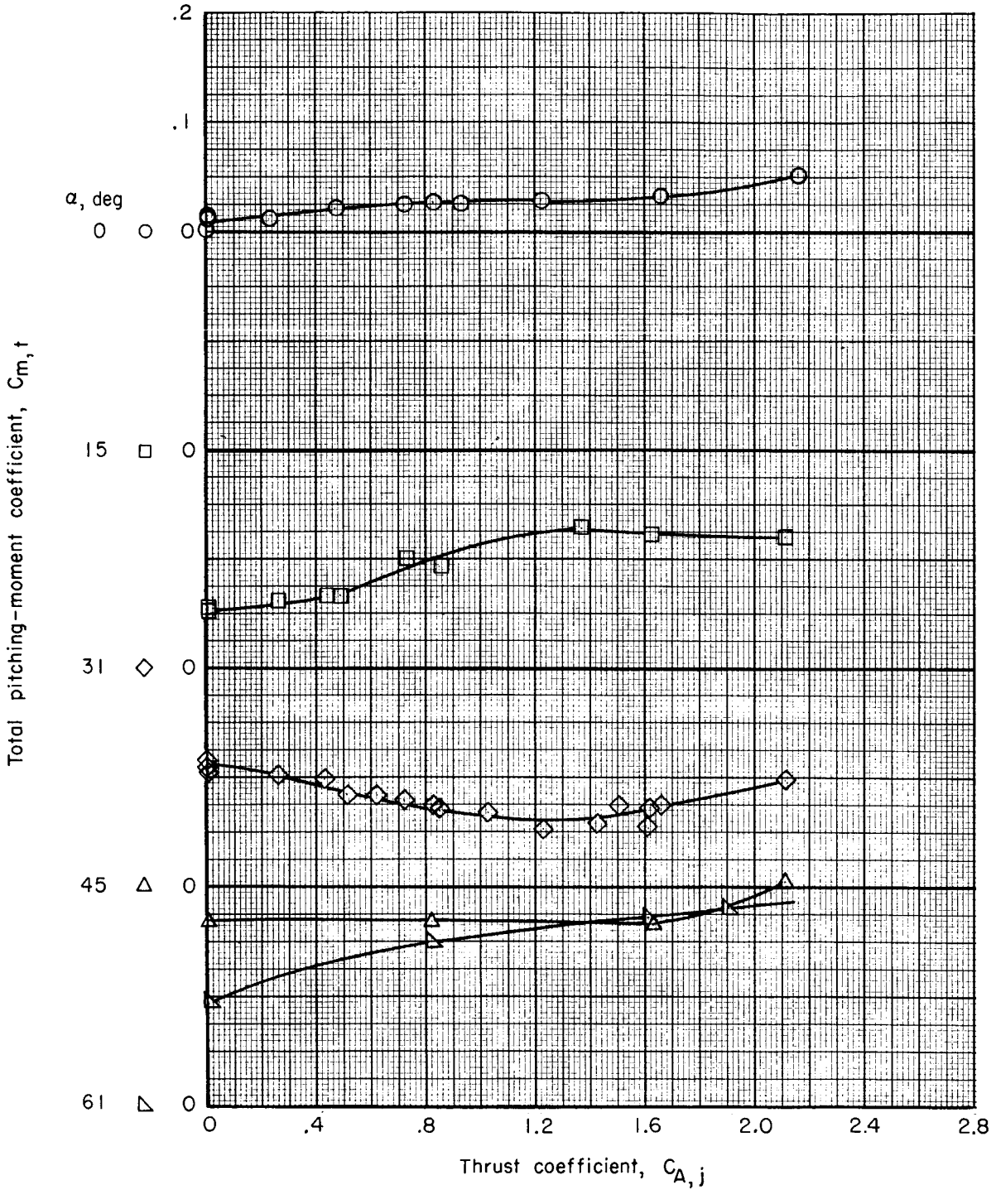

(c) Total pitching-moment coefficient.

Figure 13.- Concluded.

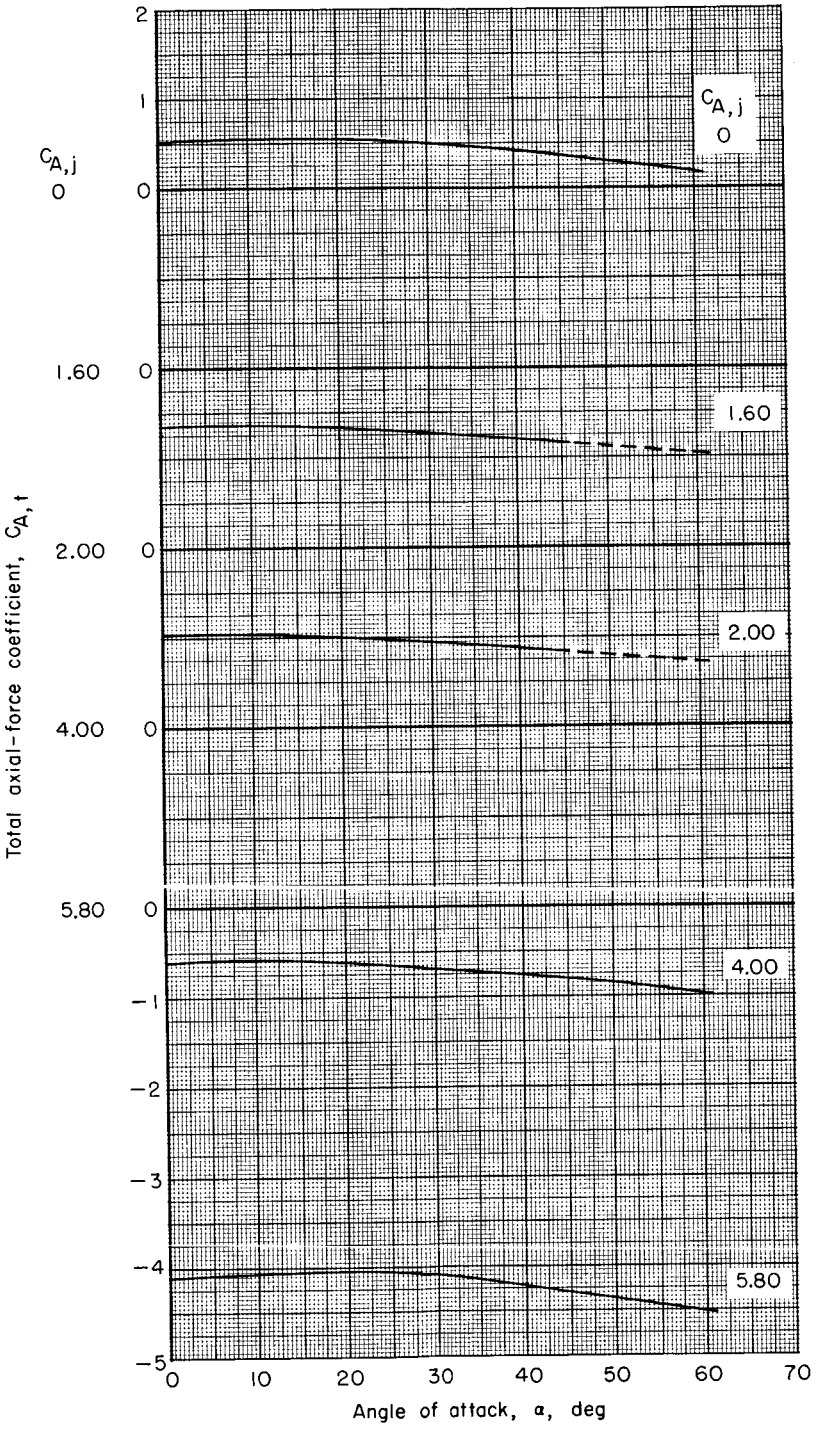

(a) Total axial-force coefficient.

Figure 14.- Variation of total force and moment coefficient with angle of attack. M = 0.50.

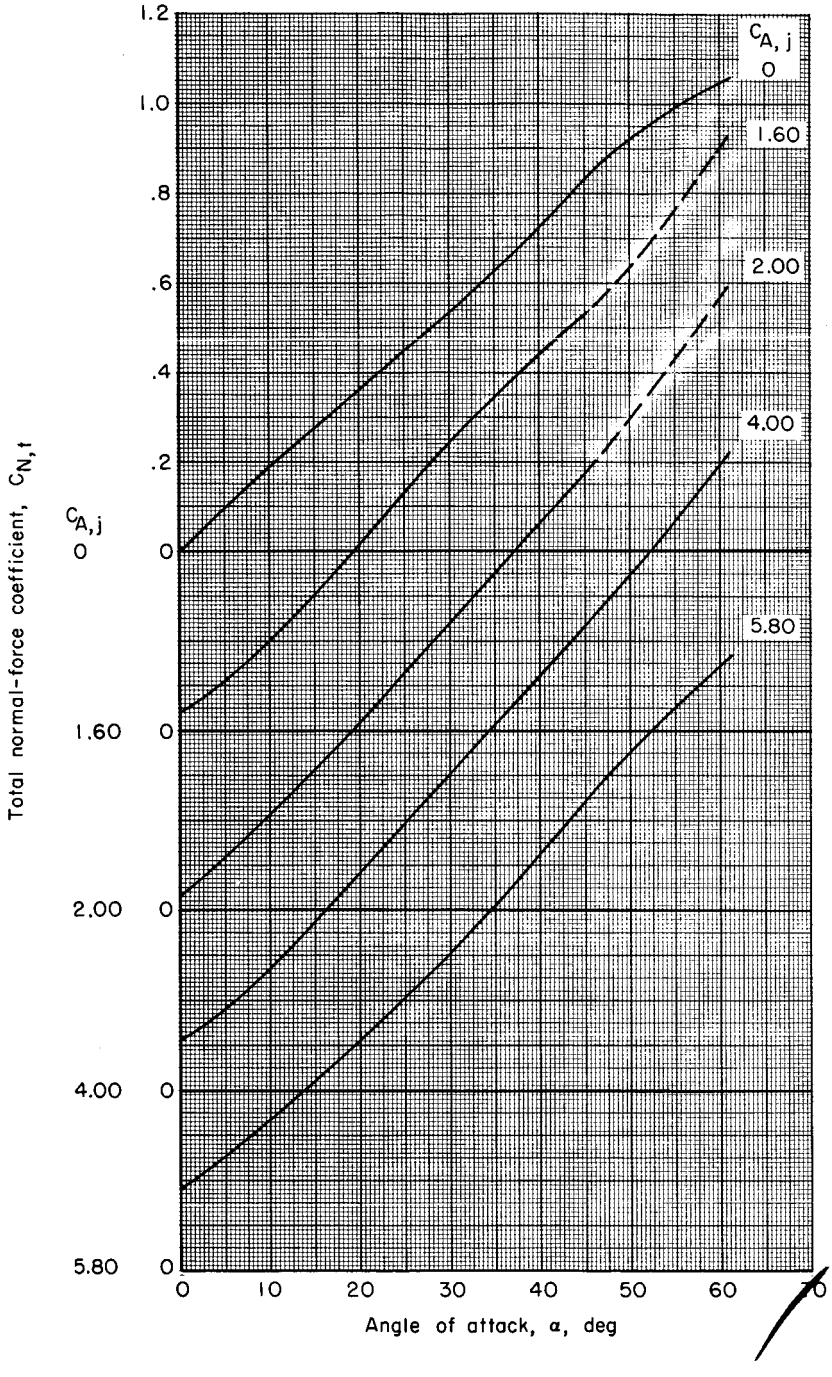

(b) Total normal-force coefficient.

Figure 14.- Continued.

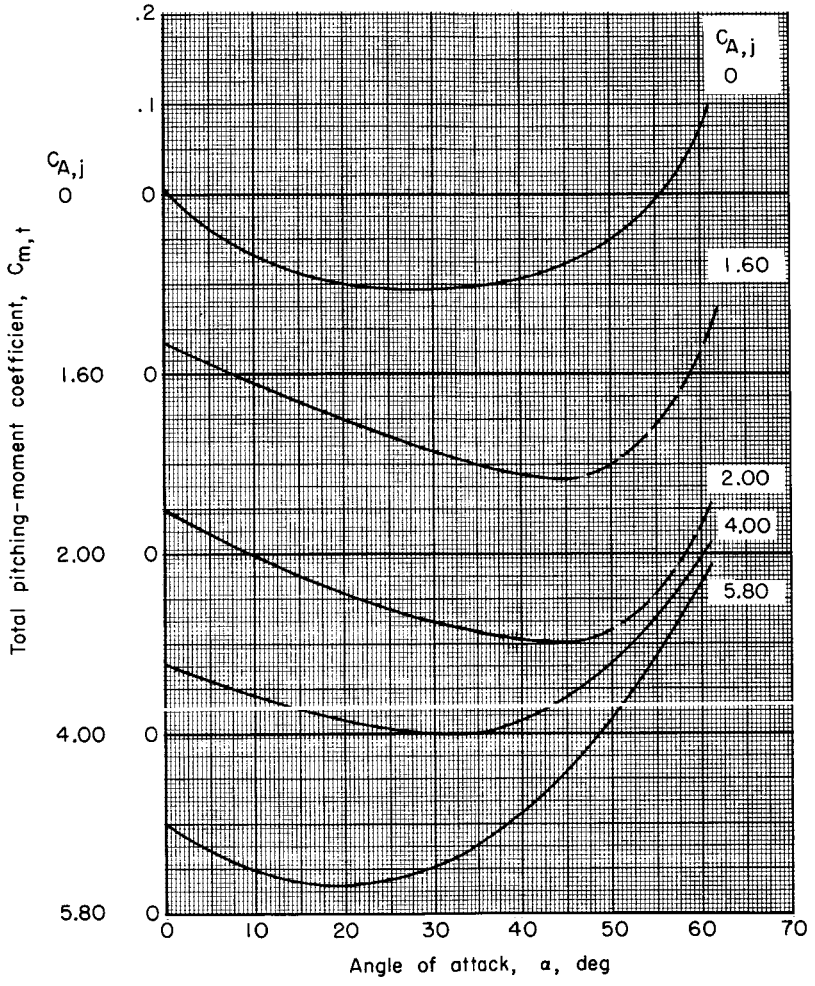

(c) Total pitching-moment coefficient.

Figure 14.- Concluded.

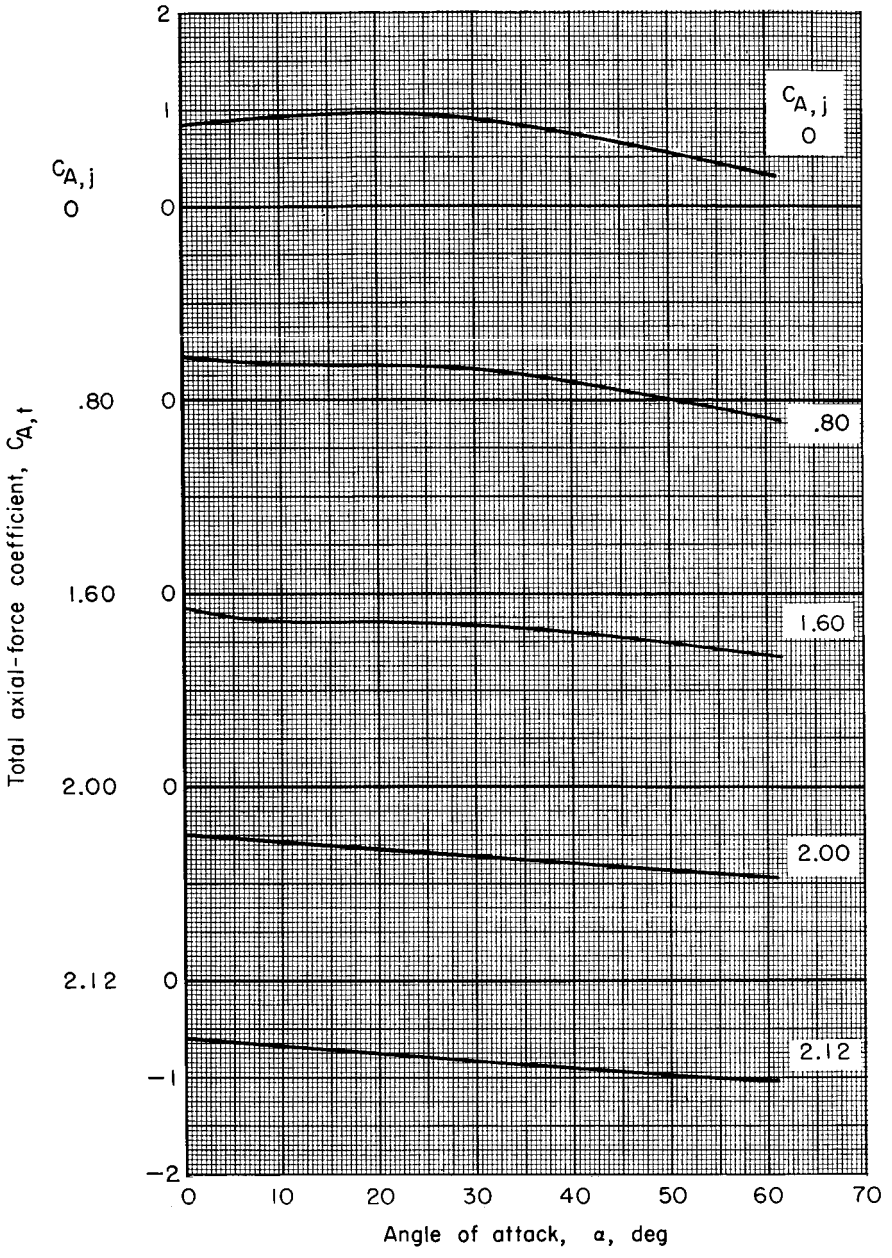

(a) Total axial-force coefficient.

Figure 15.- Variation of total force and moment coefficient with angle of attack. M = 1.3.

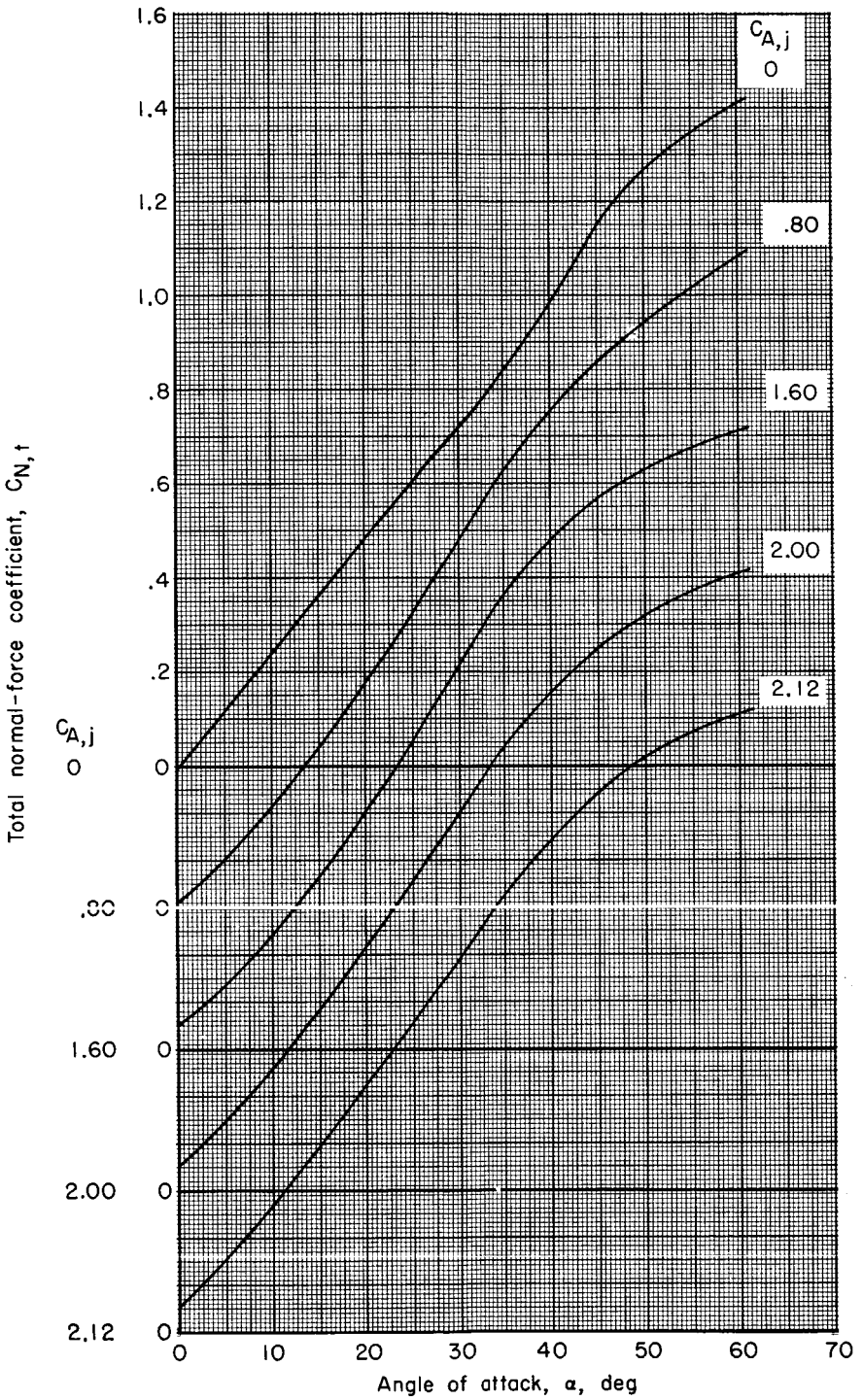

(b) Total normal-force coefficient.

Figure 15.- Continued.

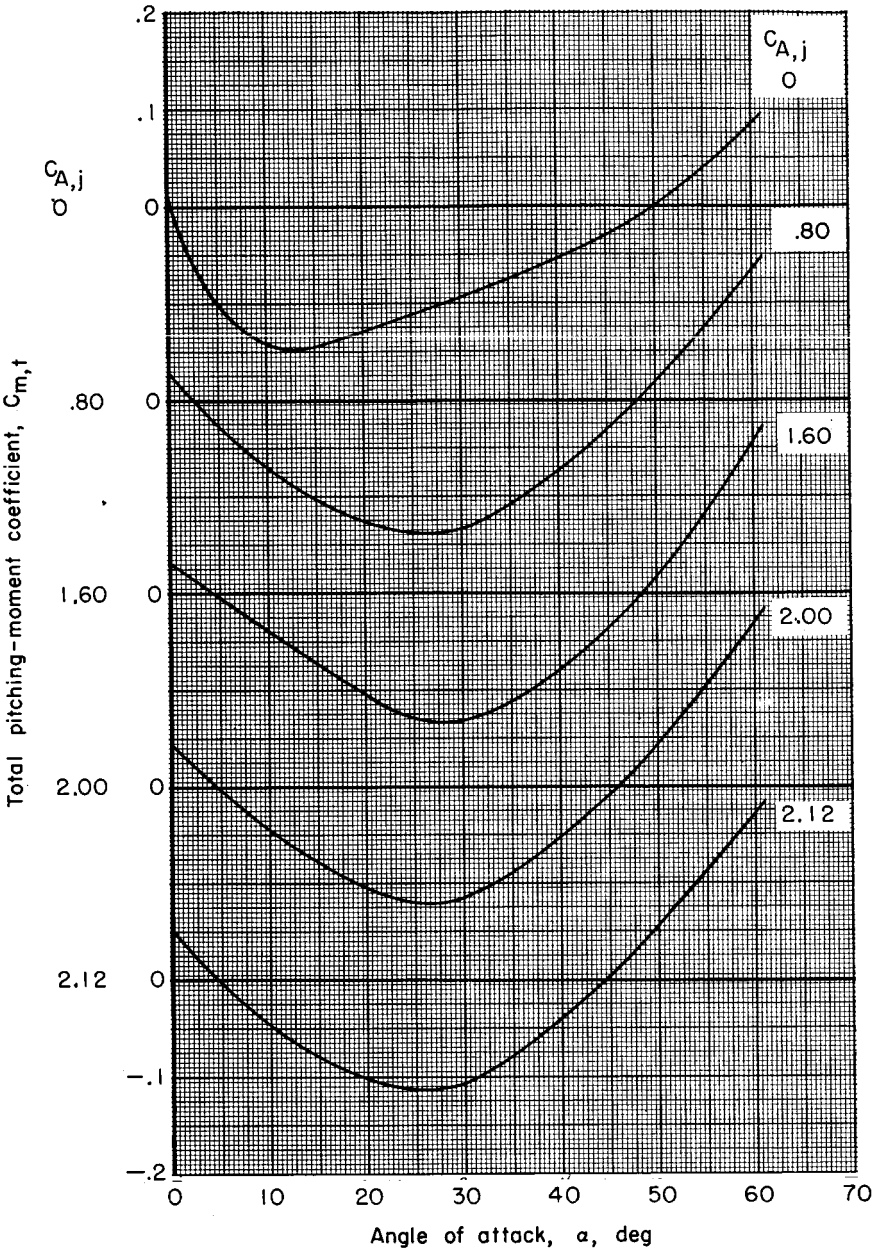

(c) Total pitching-moment coefficient.

Figure 15.- Concluded.

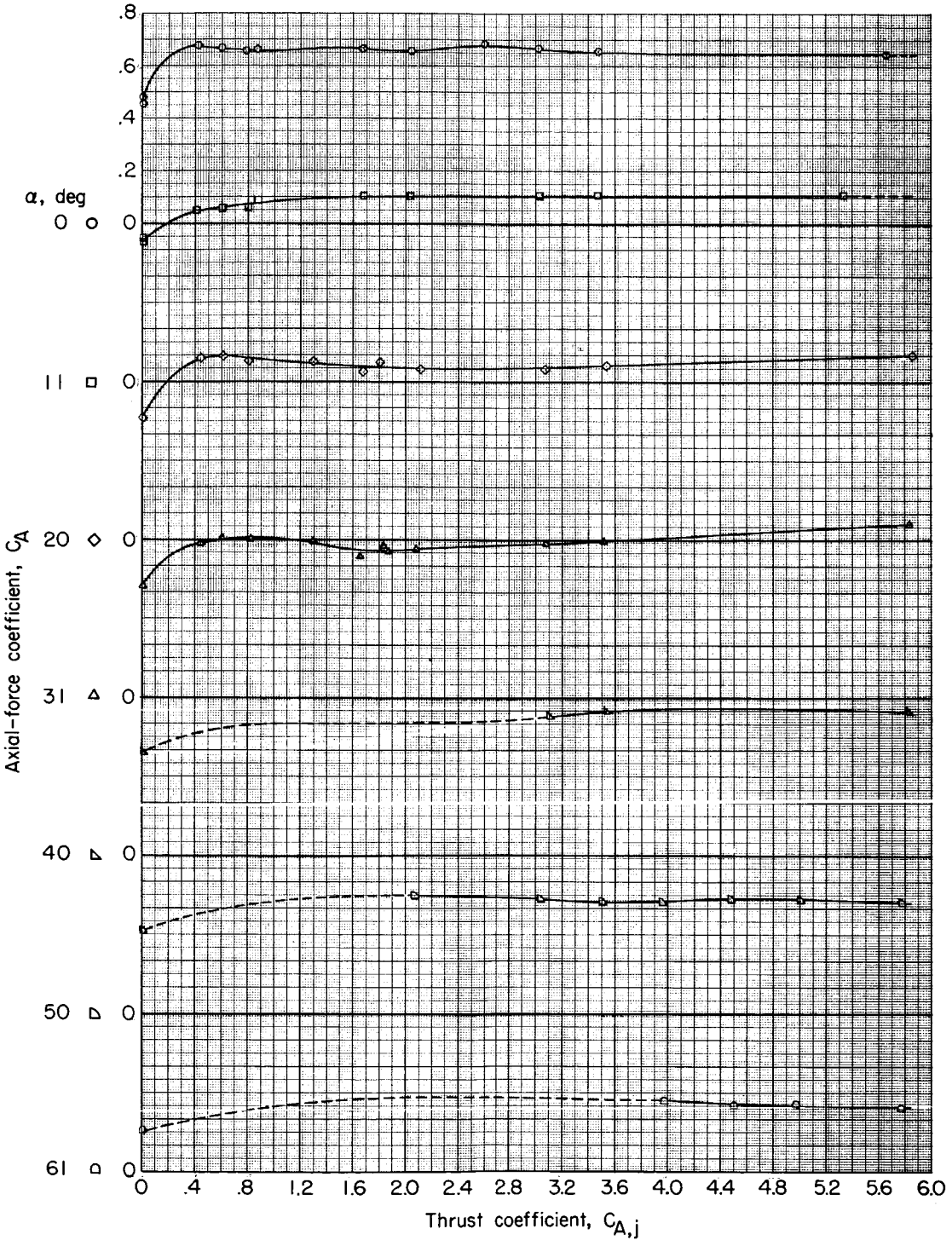

(a) M = 0.50.

Figure 16.- Variation of axial-force coefficient with thrust coefficient.

CON[redacted]L

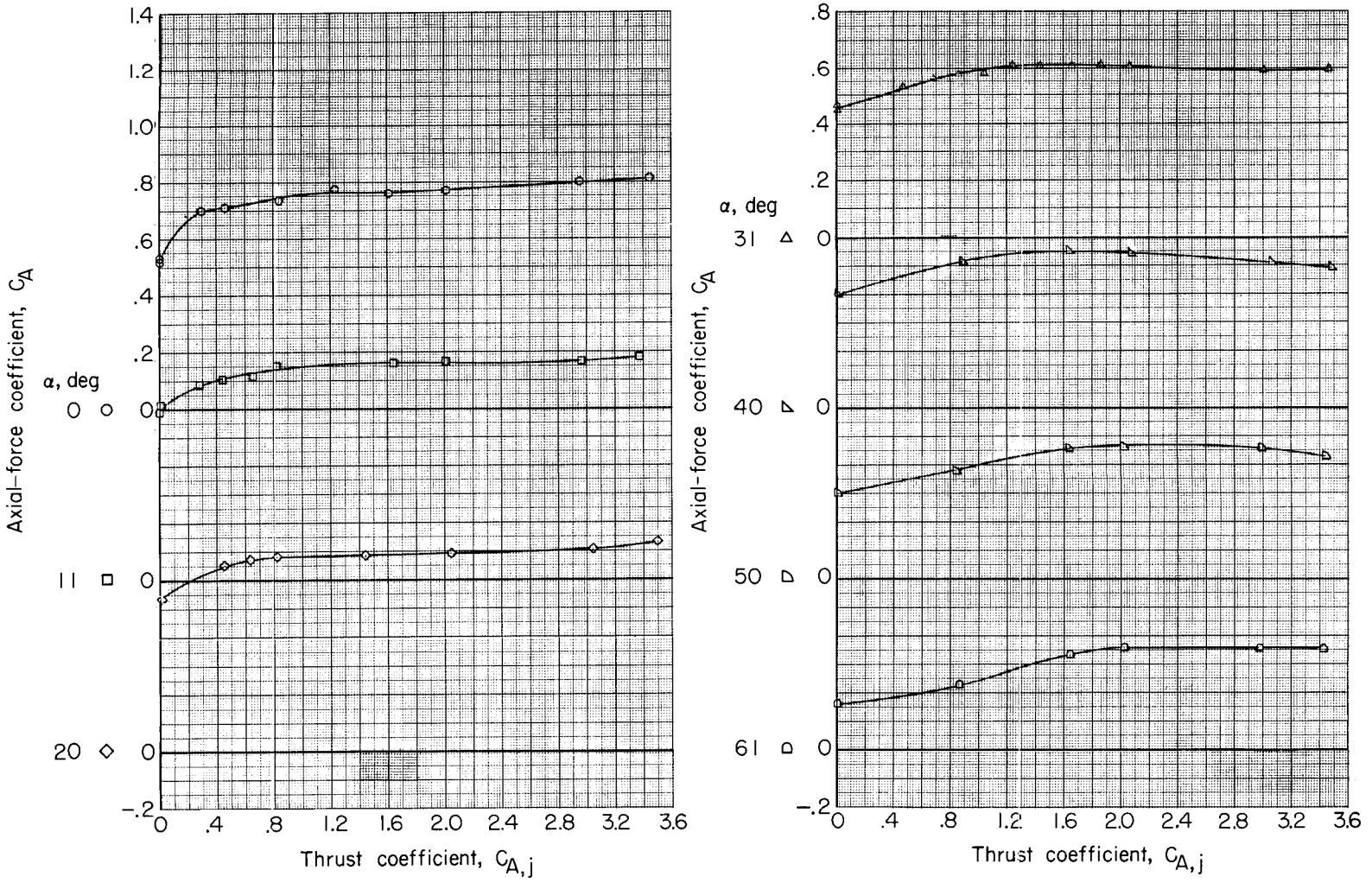

(b) M = 0.70.

Figure 16.- Continued.

CON[redacted]L

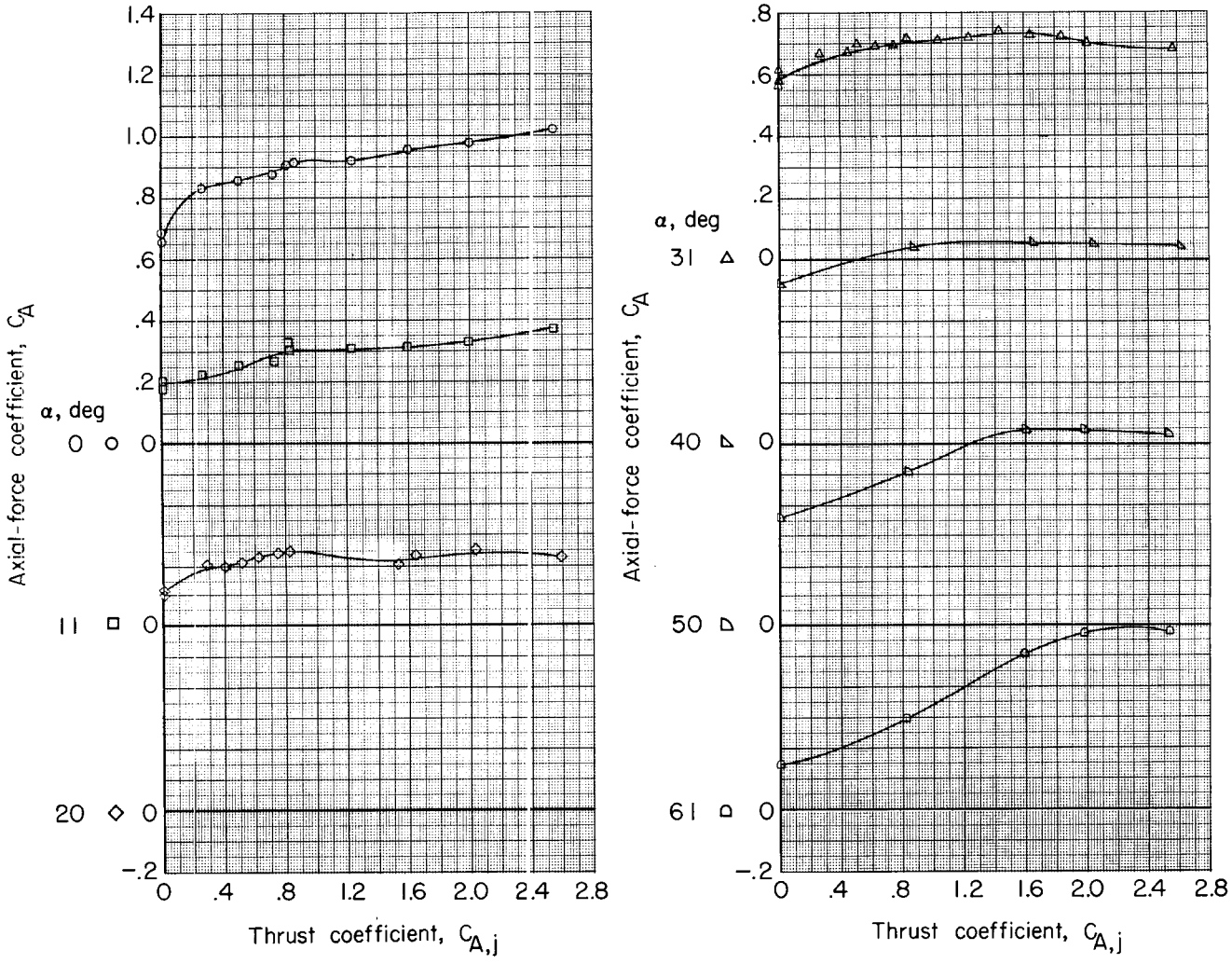

(c) M = 0.90.

Figure 16.- Continued.

CONFIDENTIAL

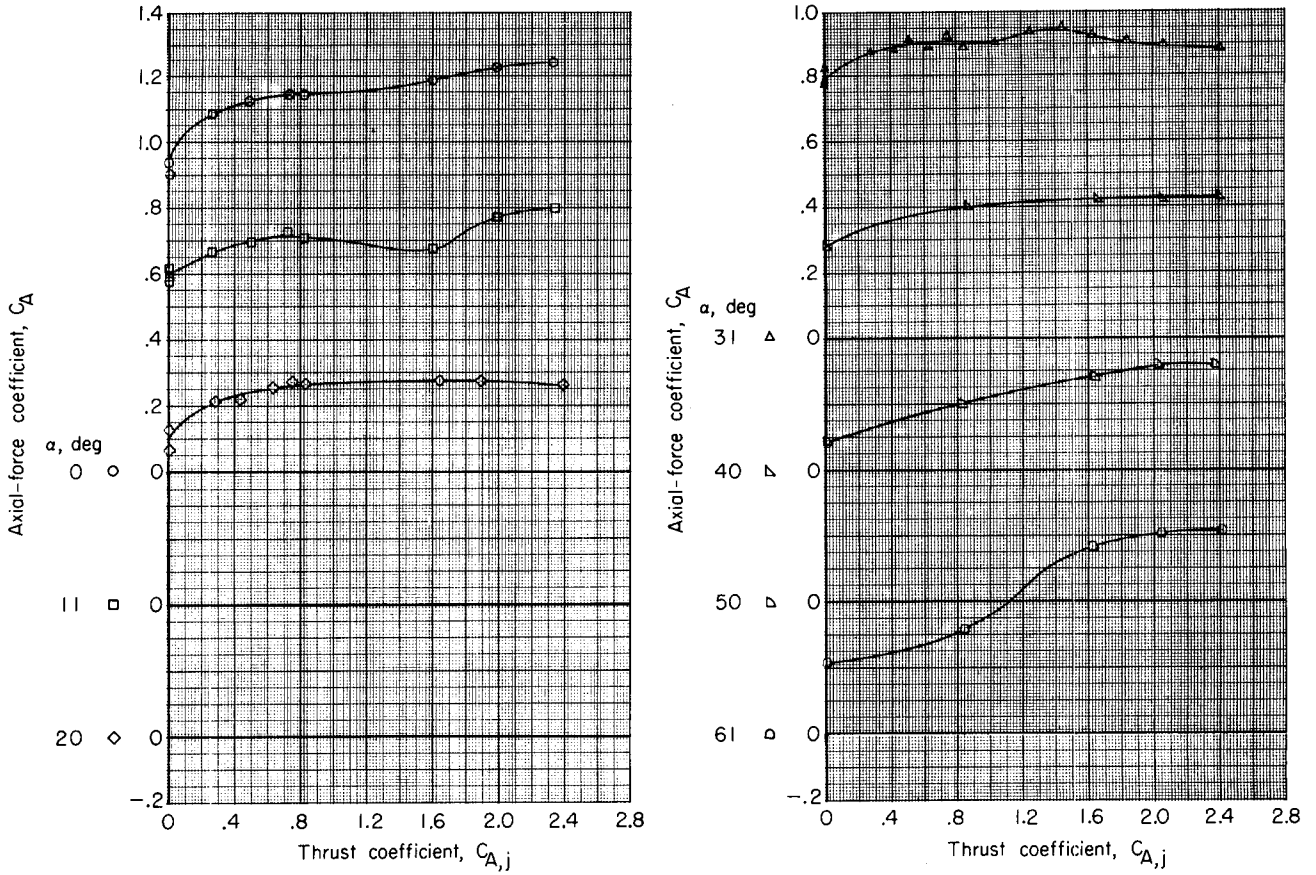

(d) M = 1.00.

Figure 16.- Continued.

CONFIDENTIAL

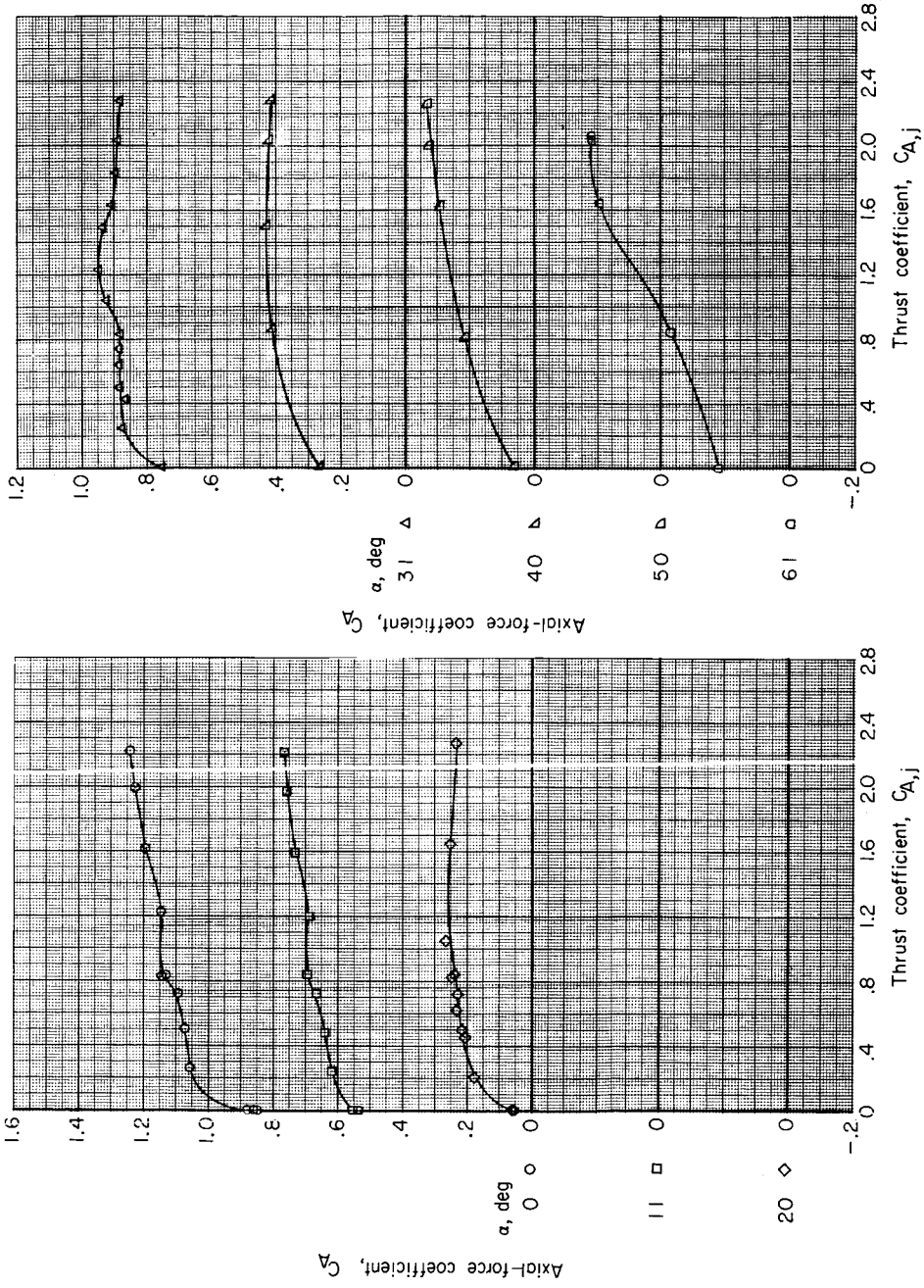

(e) M = 1.1.

Figure 16.- Continued.

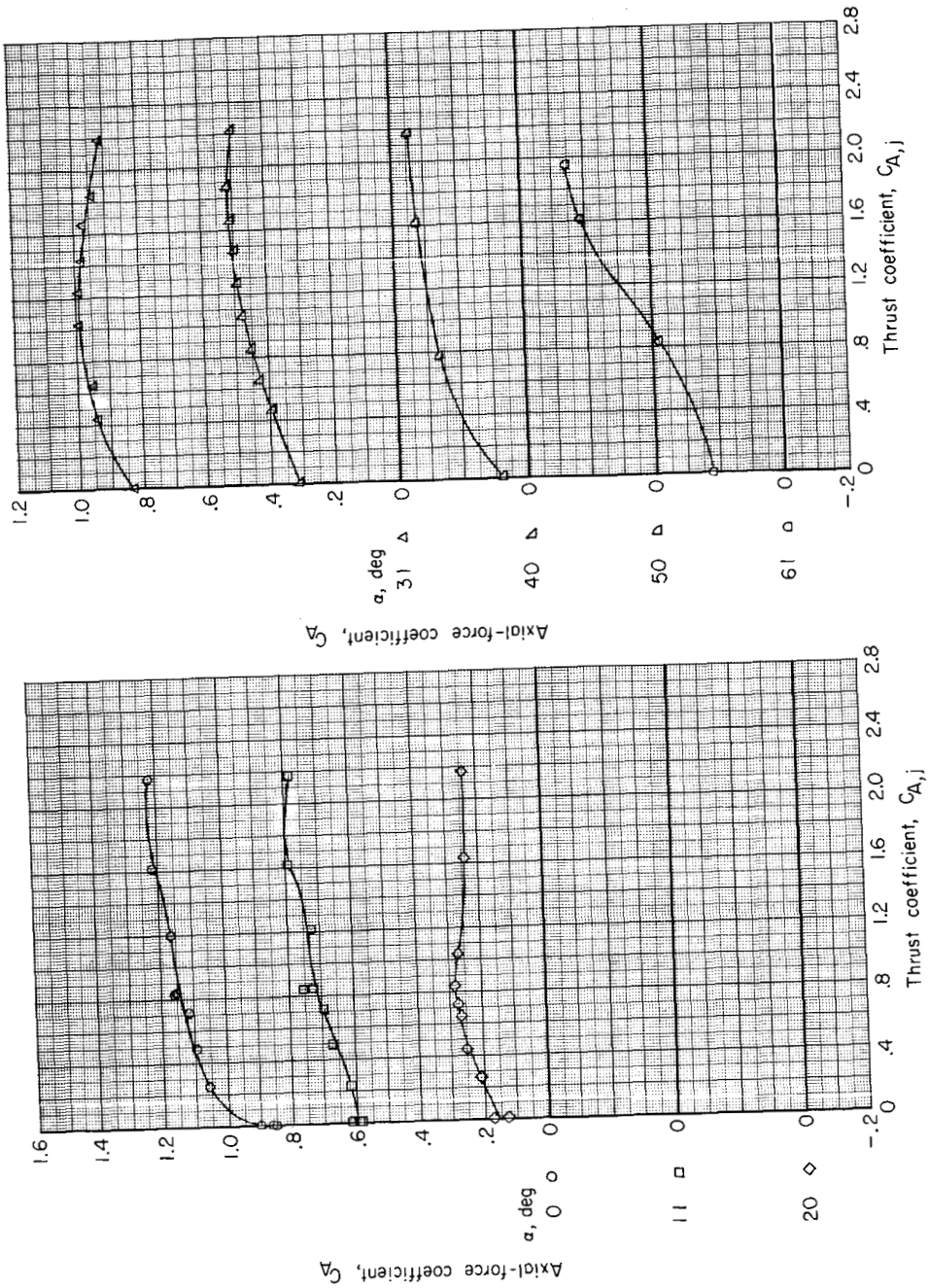

(f) M = 1.2.

Figure 16.- Continued.

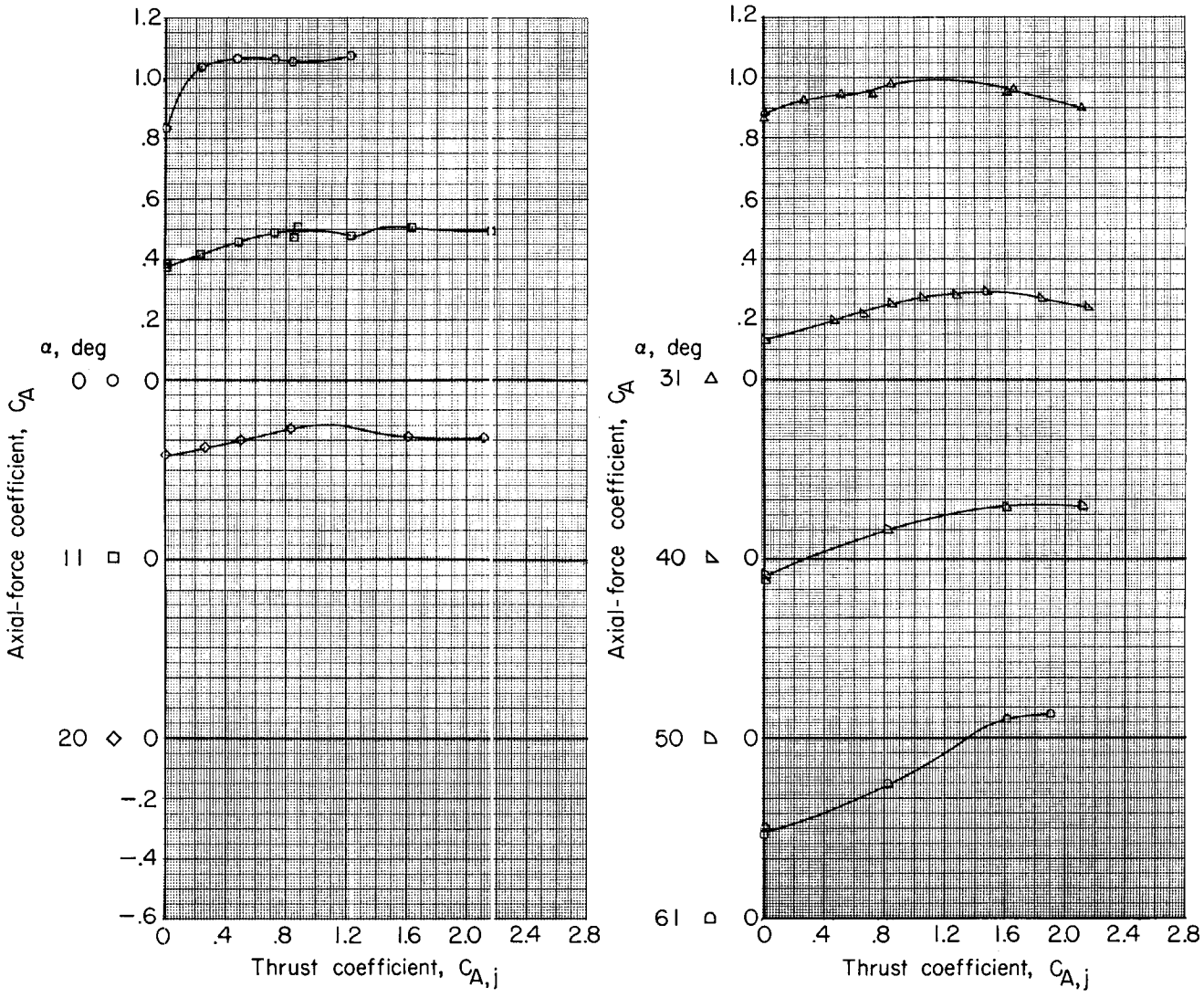

(g) M = 1.3.

Figure 16.- Concluded.

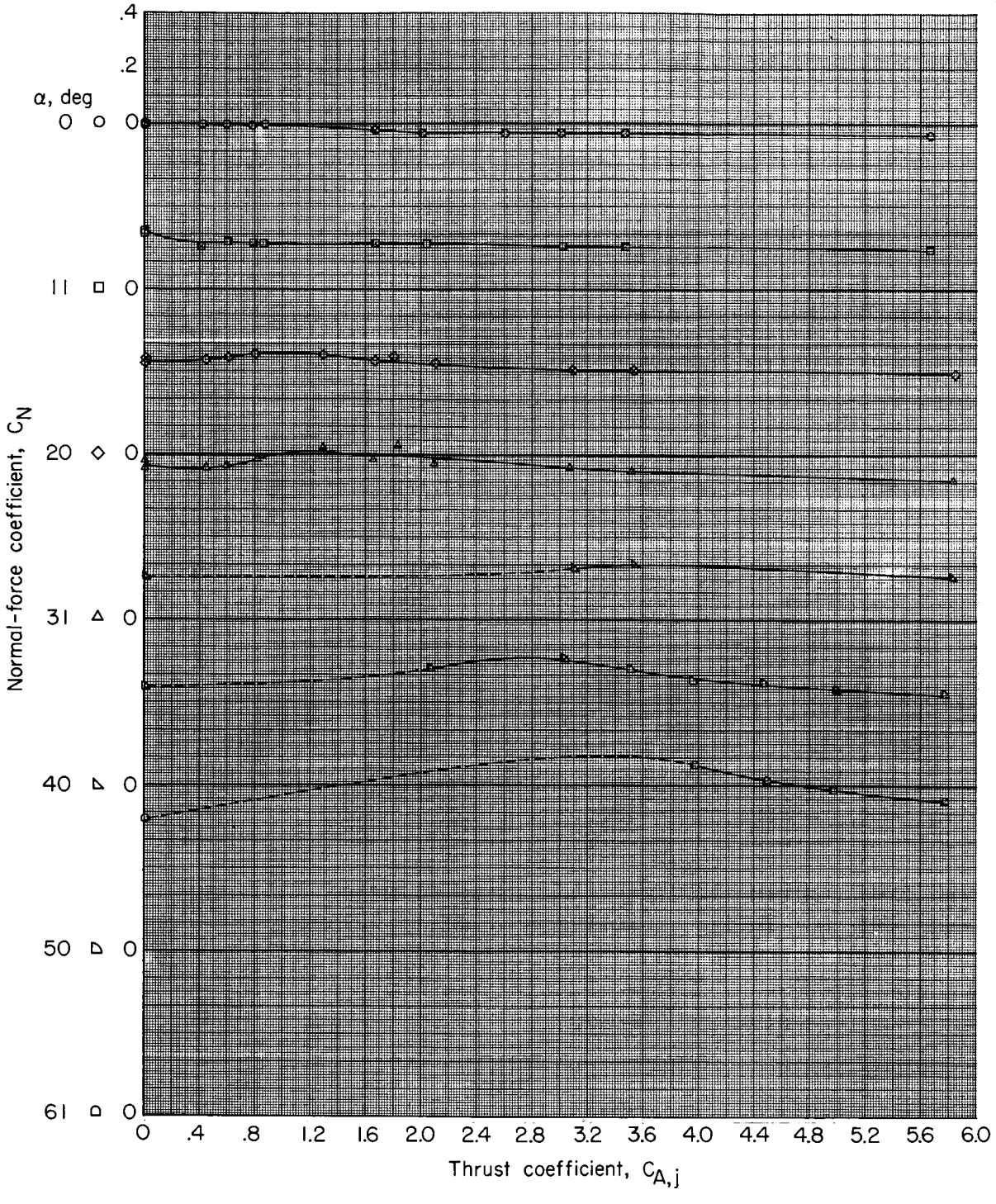

(a) M = 0.50.

Figure 17.- Variation of normal-force coefficient with thrust coefficient.

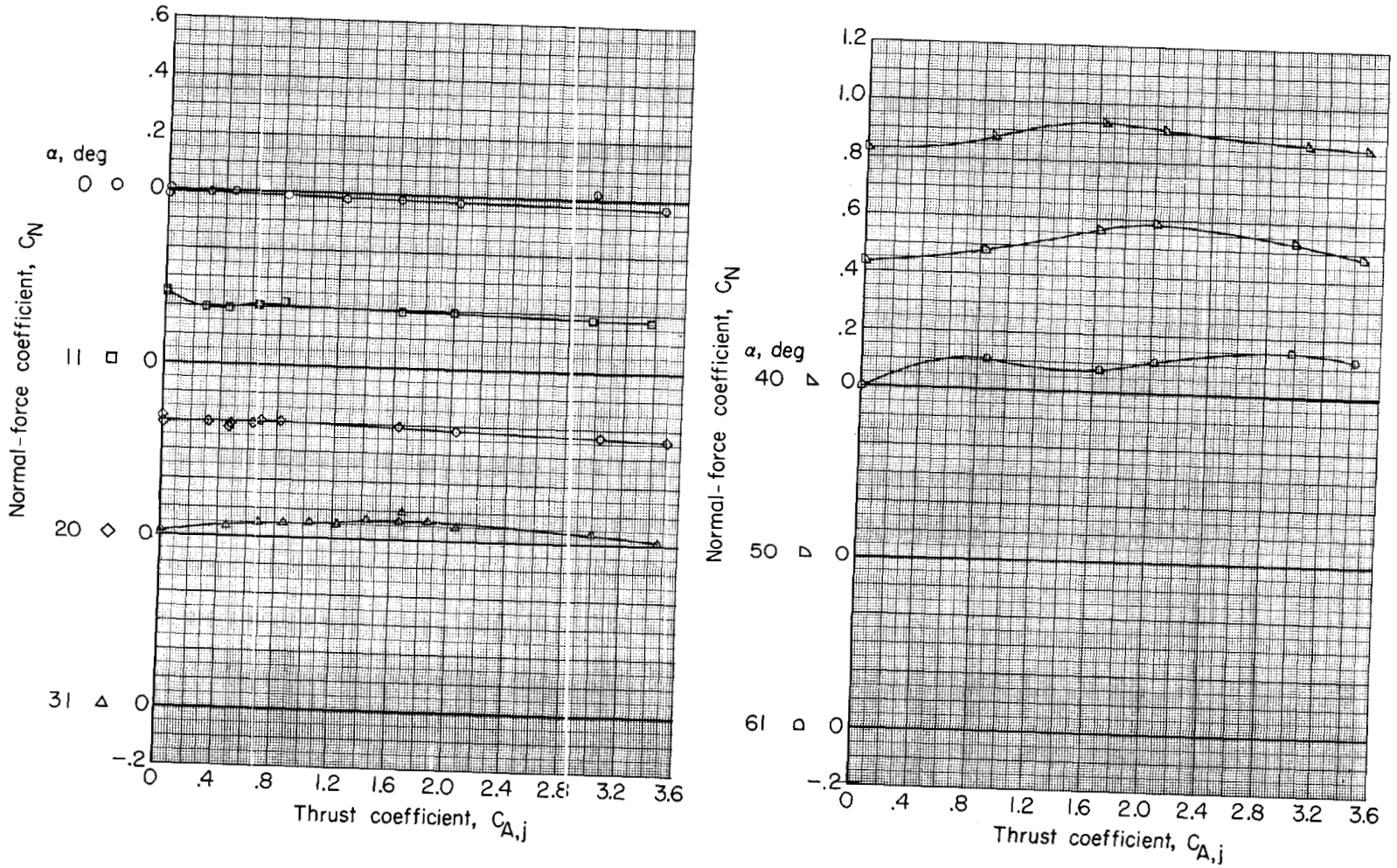

(b) M = 0.70.

Figure 17.- Continued.

CO[redacted]

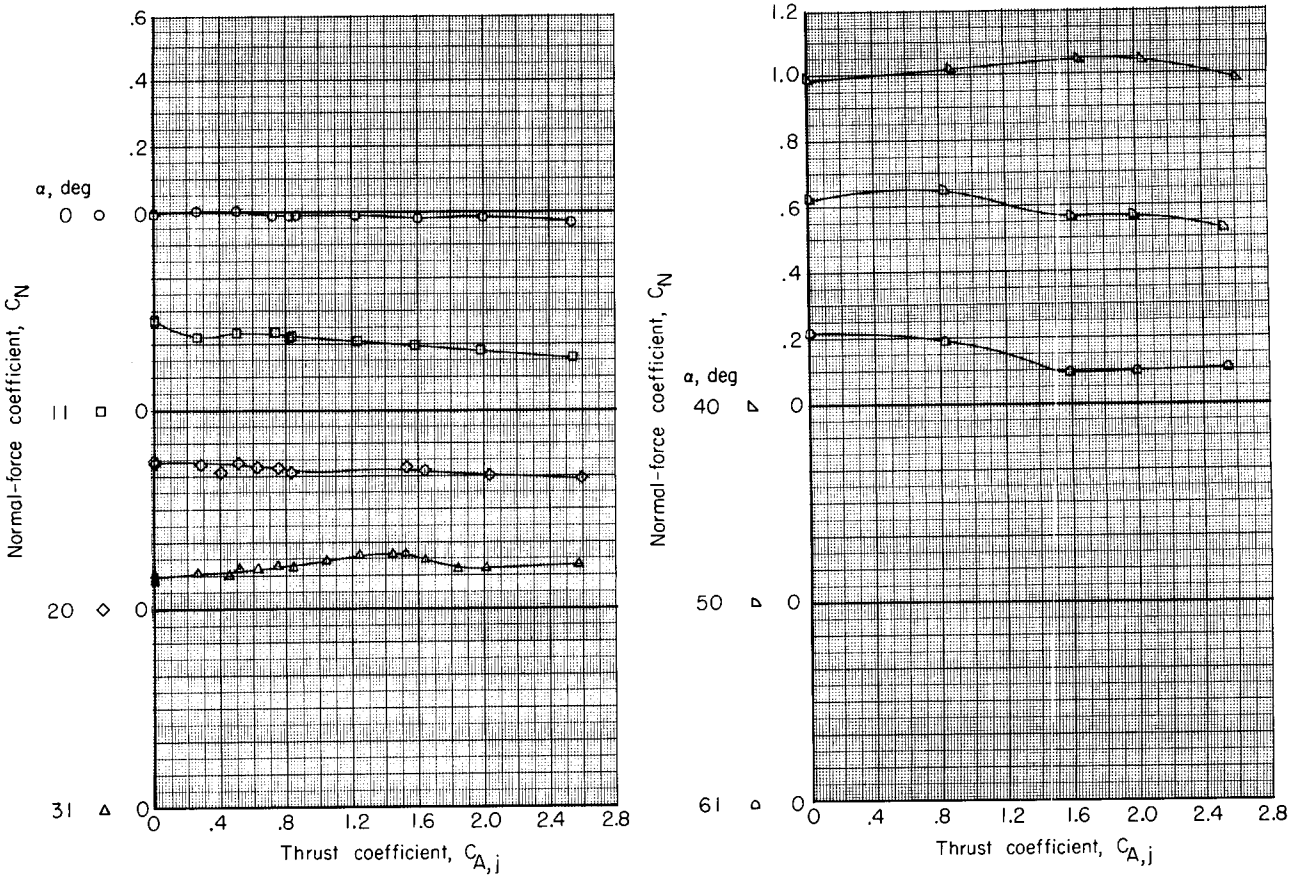

(c) M = 0.90.

Figure 17.- Continued.

CO[redacted]L

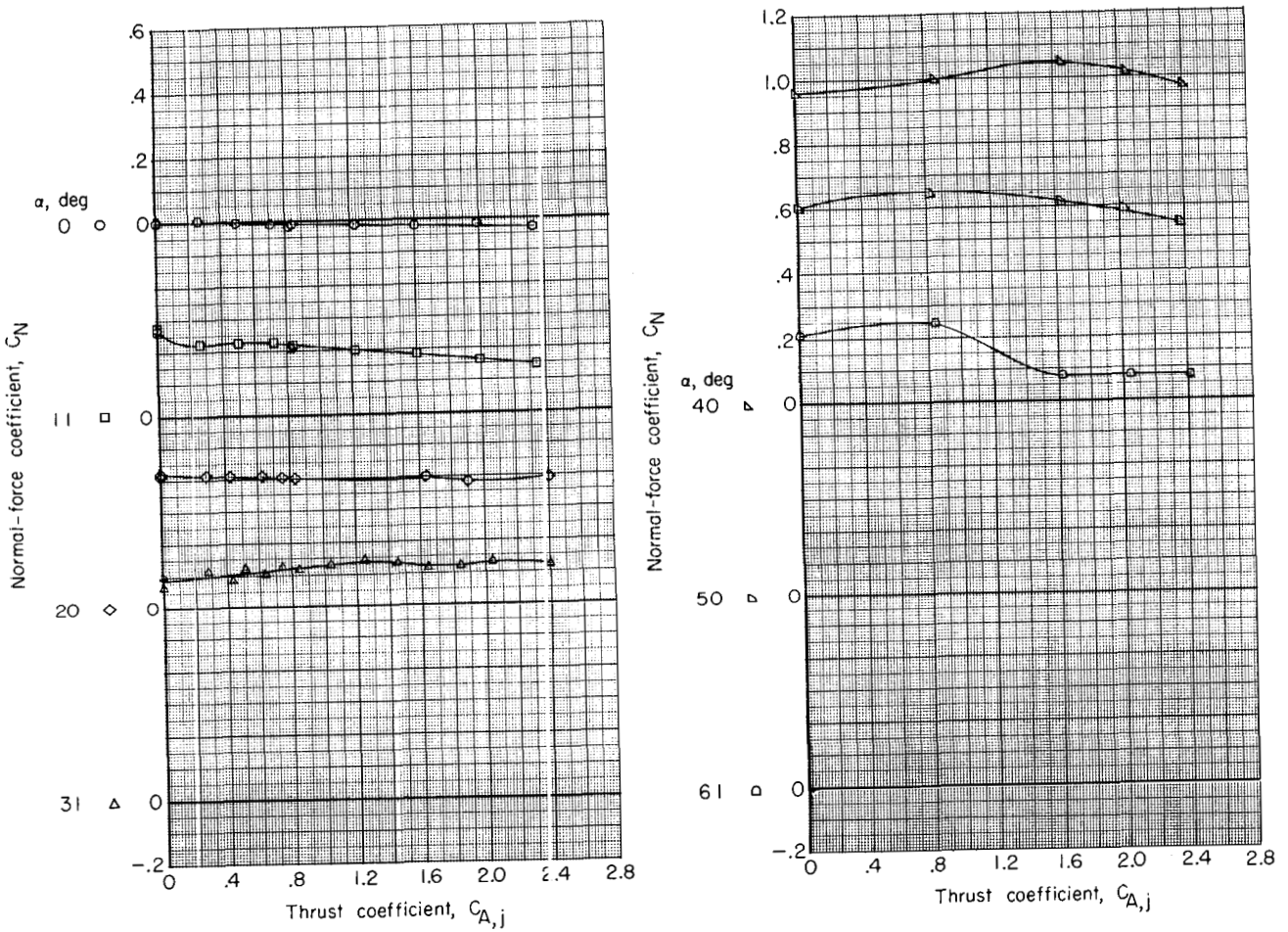

(d) M = 1.00.

Figure 17.- Continued.

CONFIDENTIAL

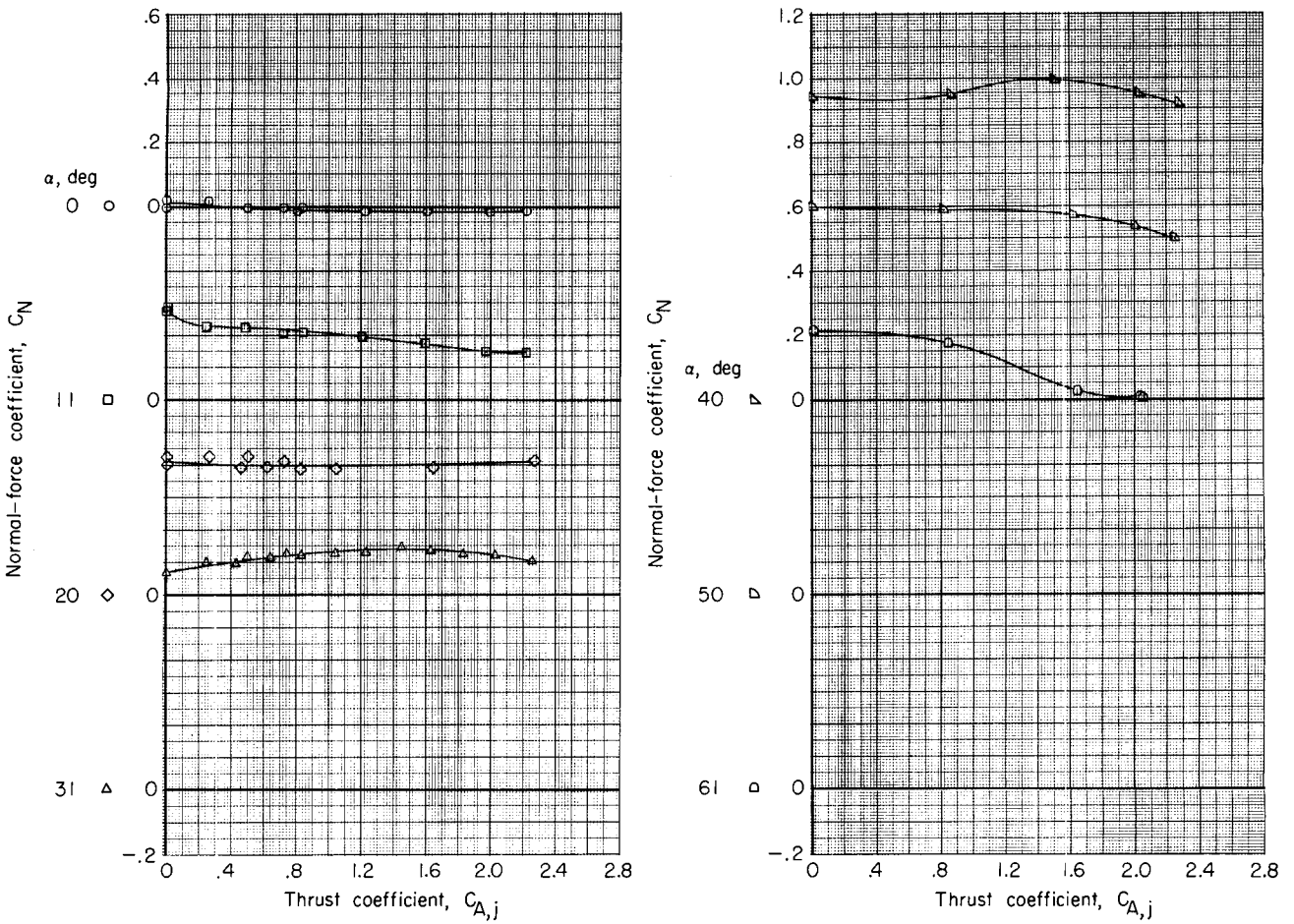

(e) M = 1.1.

Figure 17.- Continued.

CONFIDENTIAL

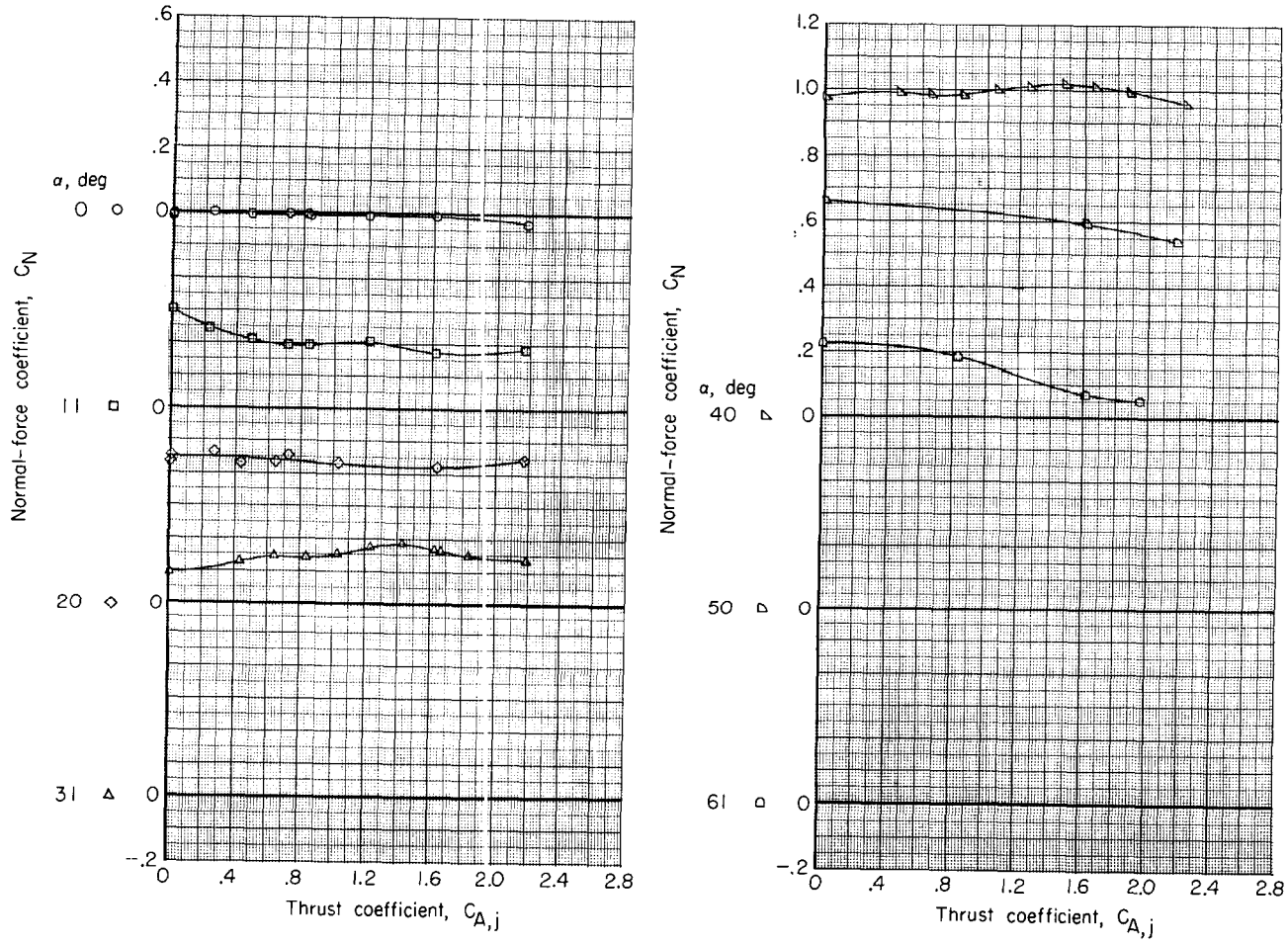

(f) M = 1.2.

Figure 17.- Continued.

CON[redacted]TIAL

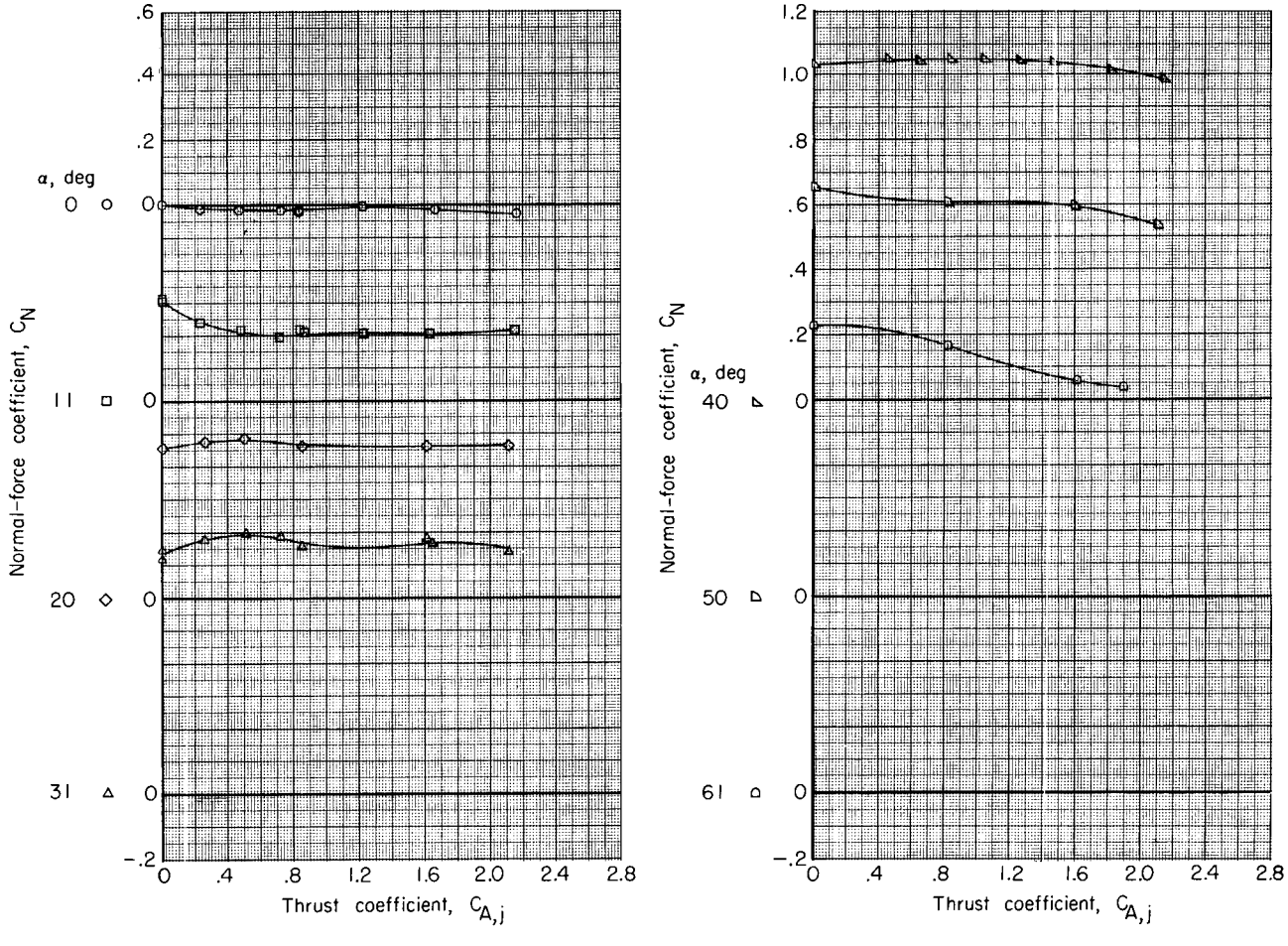

(g) M = 1.3.

Figure 17.- Concluded.

CO[redacted]AL

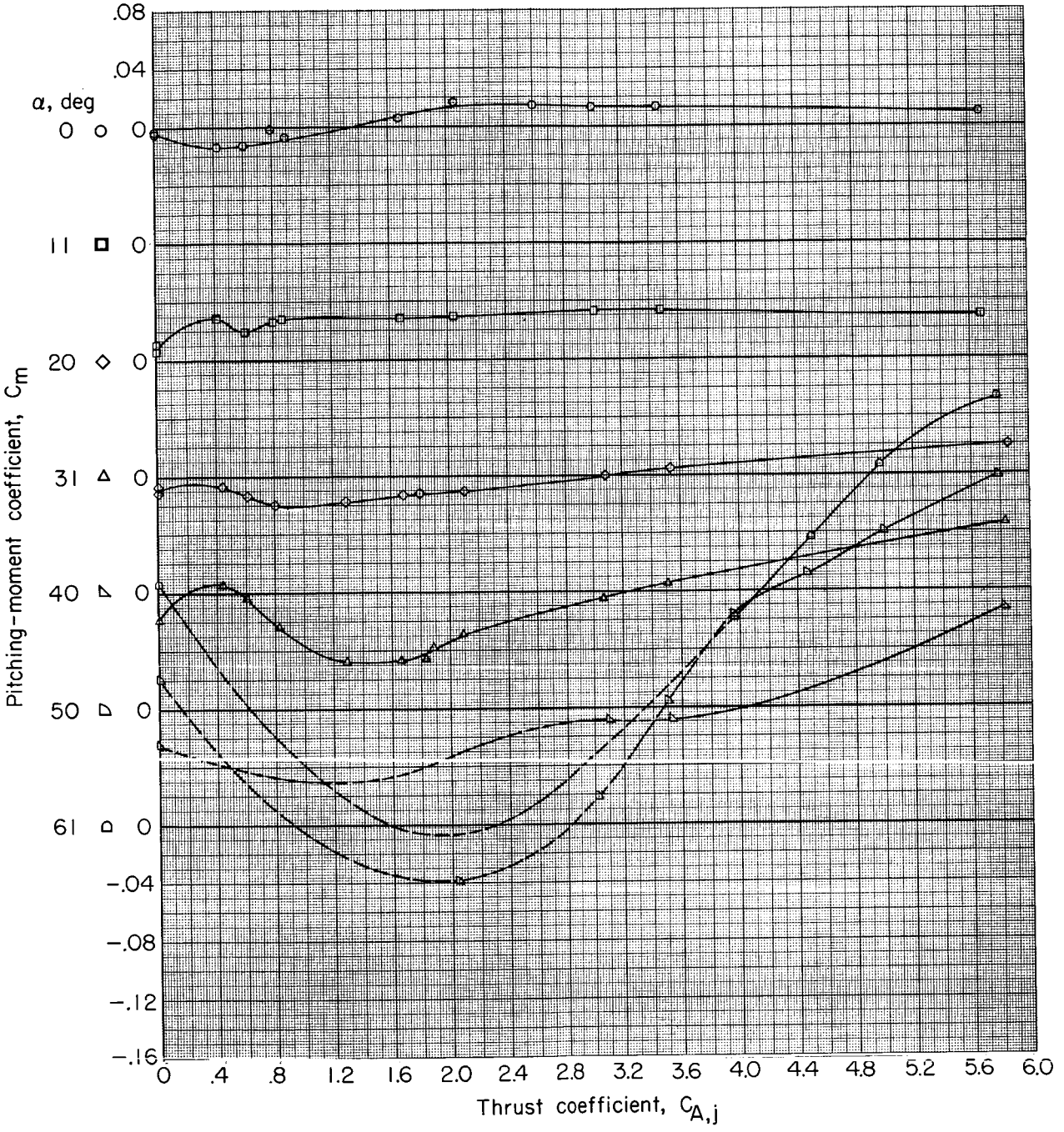

(a) M = 0.50.

Figure 18.- Variation of pitching-moment coefficient with thrust coefficient.

CON[redacted]L

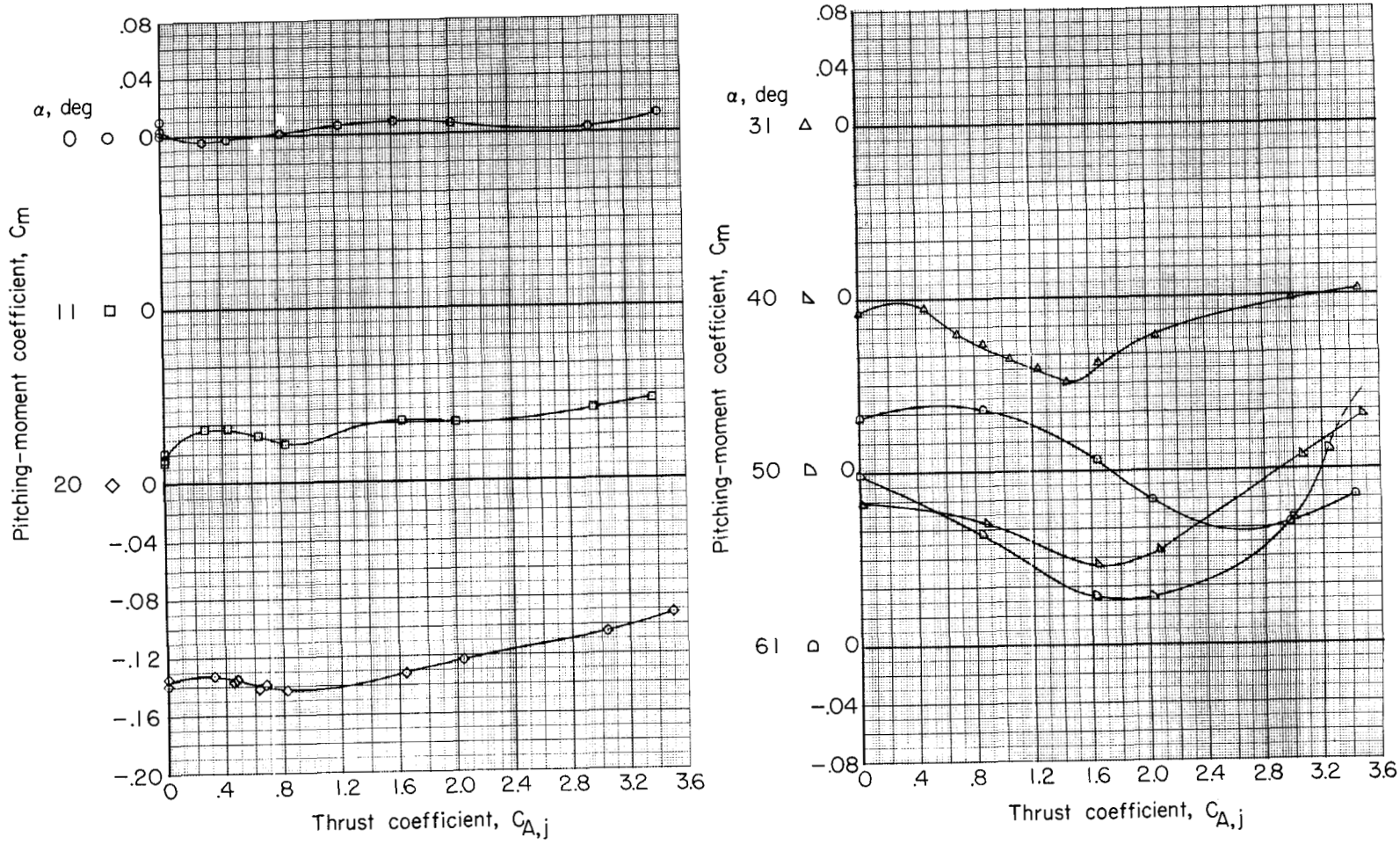

(b) M = 0.70.

Figure 18.- Continued.

CON[redacted]L

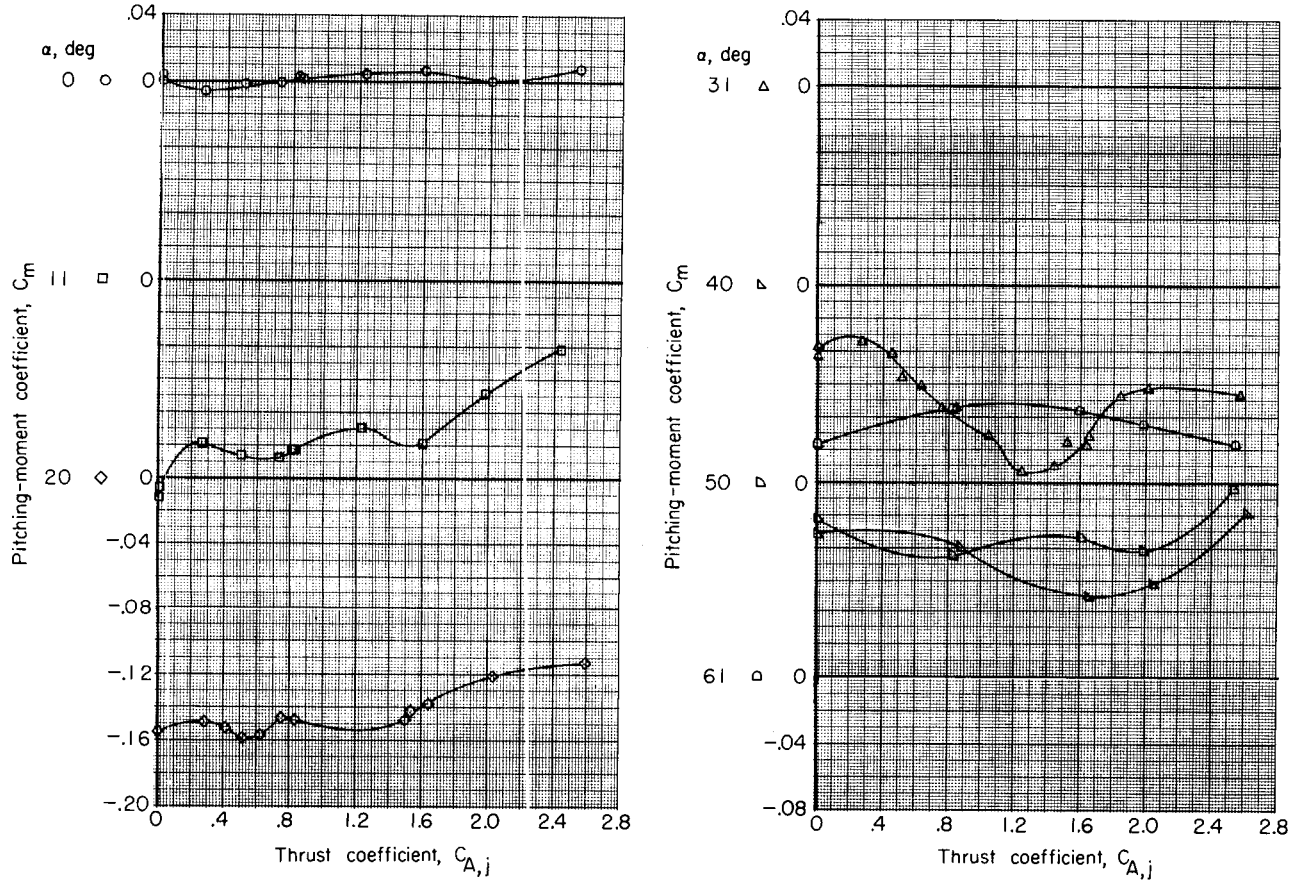

(c) M = 0.90.

Figure 18.- Continued.

CONFIDENTIAL

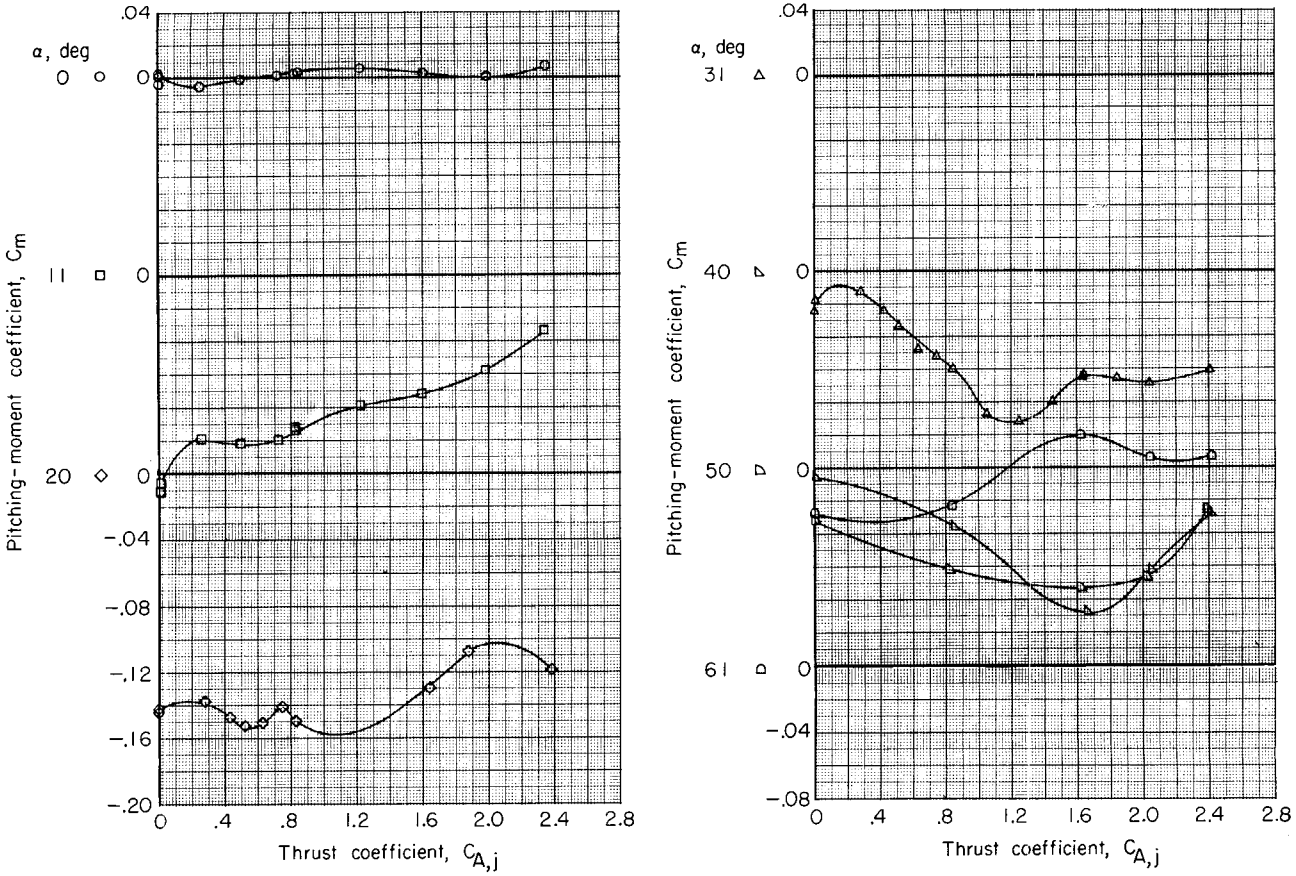

(d) M = 1.00.

Figure 18.- Continued.

CONFIDENTIAL

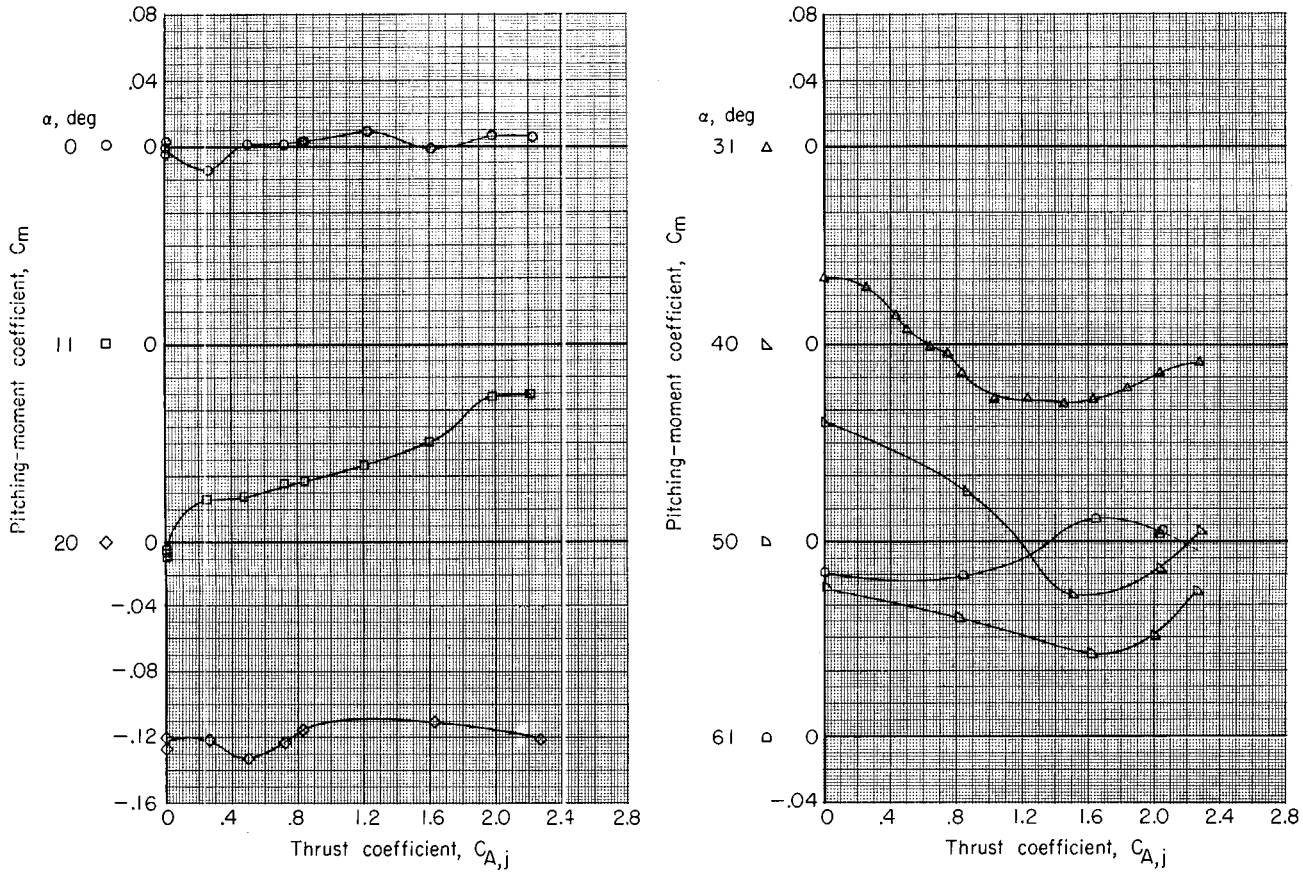

(e) M = 1.1.

Figure 18.- Continued.

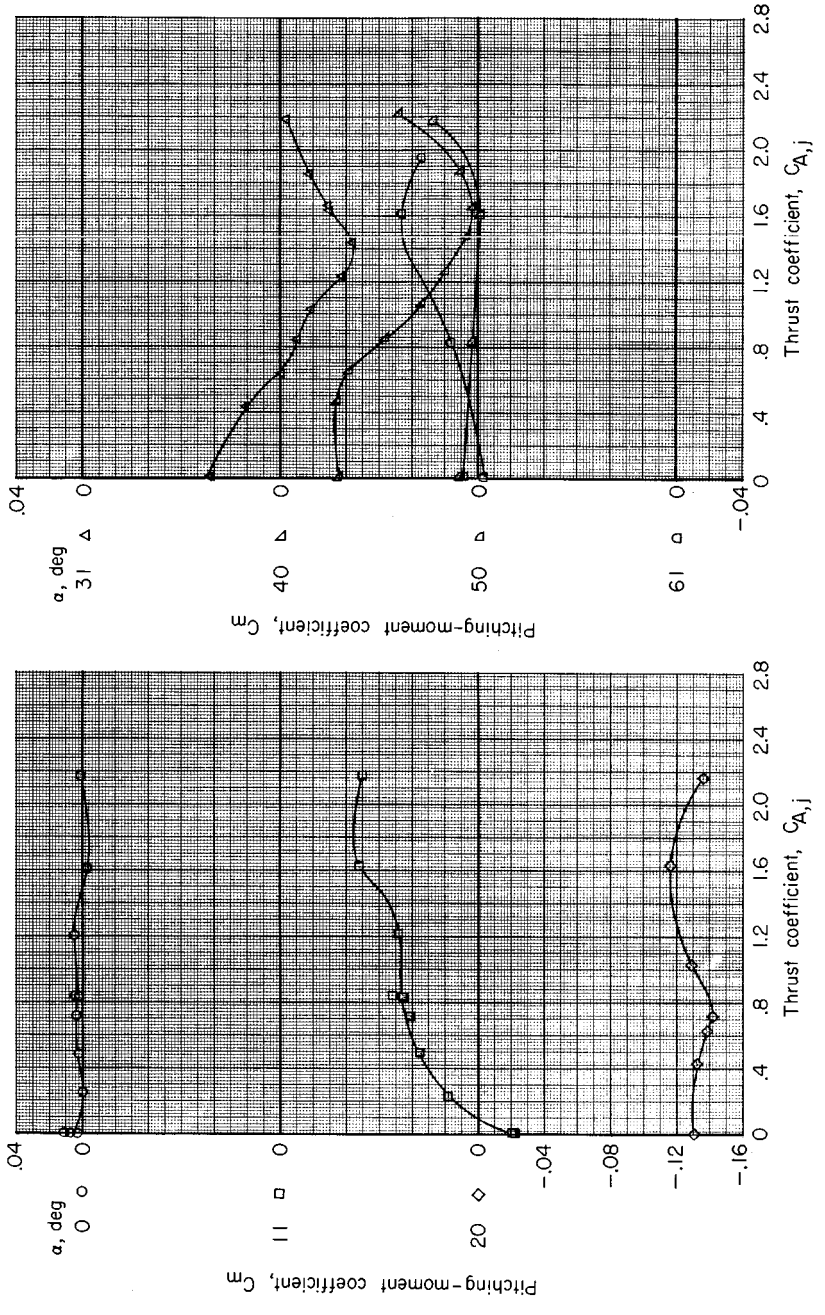

(f) M = 1.2.

Figure 18.- Continued.

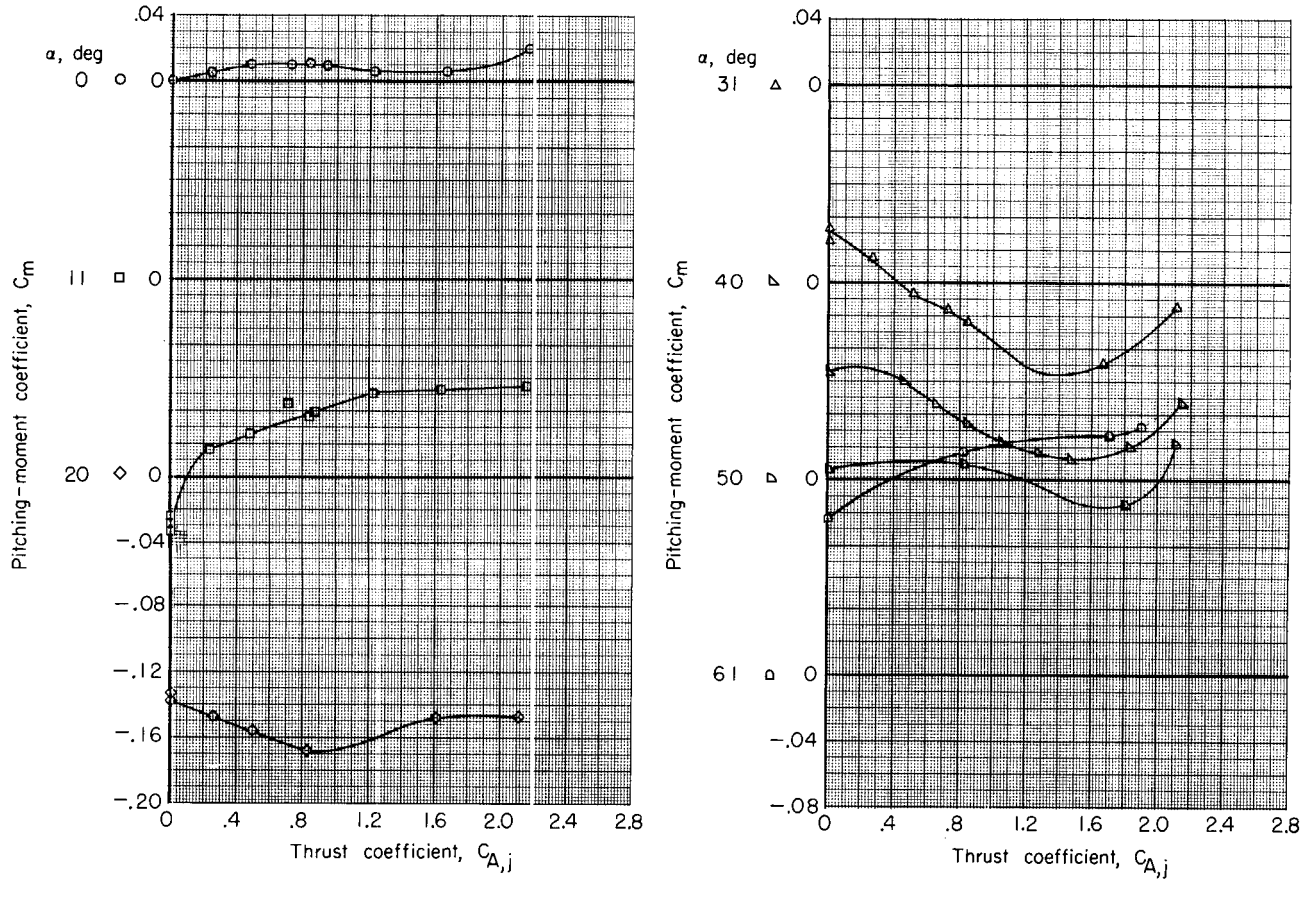

(g) M = 1.3.

Figure 18.- Concluded.

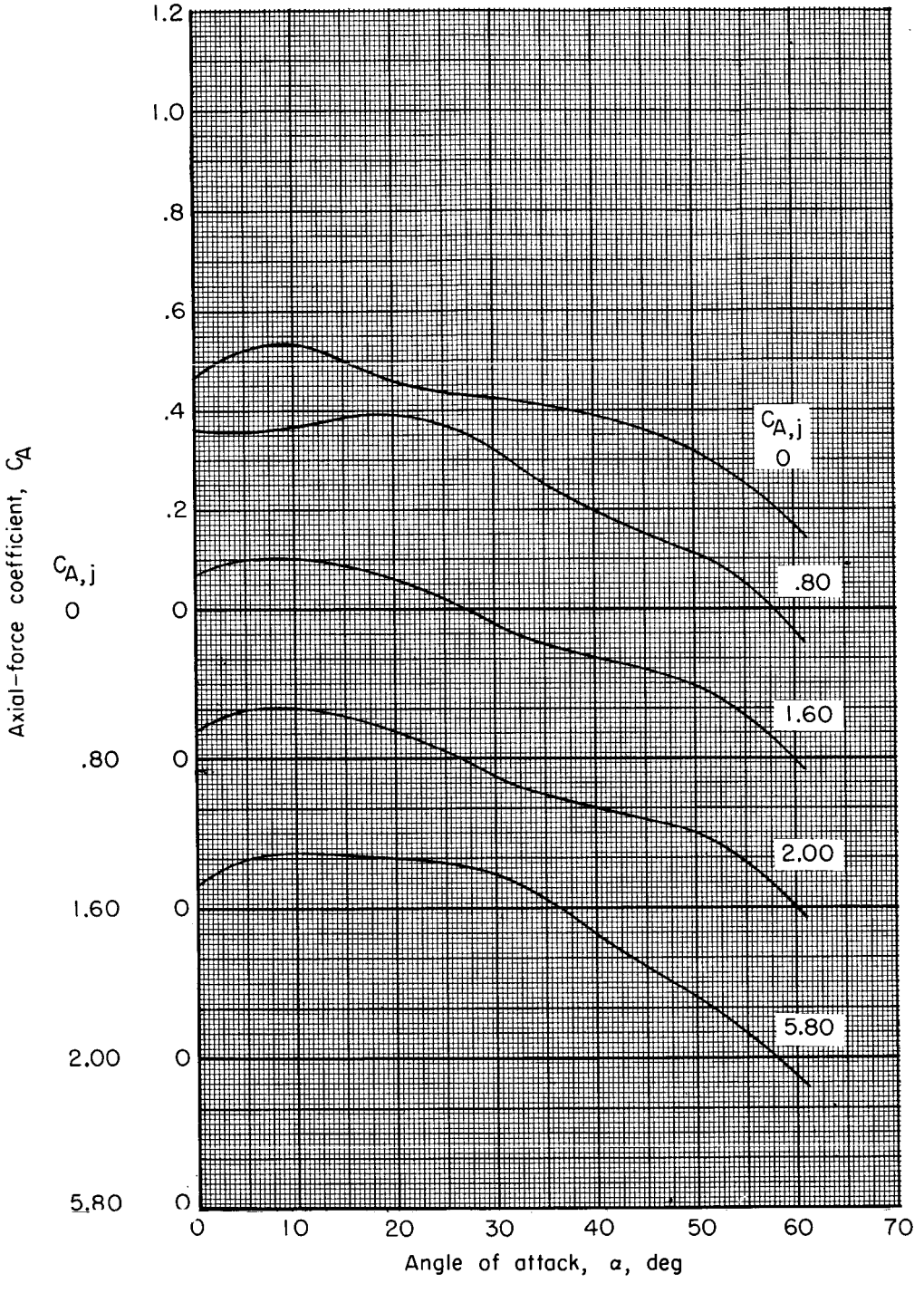

(a) M = 0.50.

Figure 19.- Variation of axial-force coefficient with angle of attack.

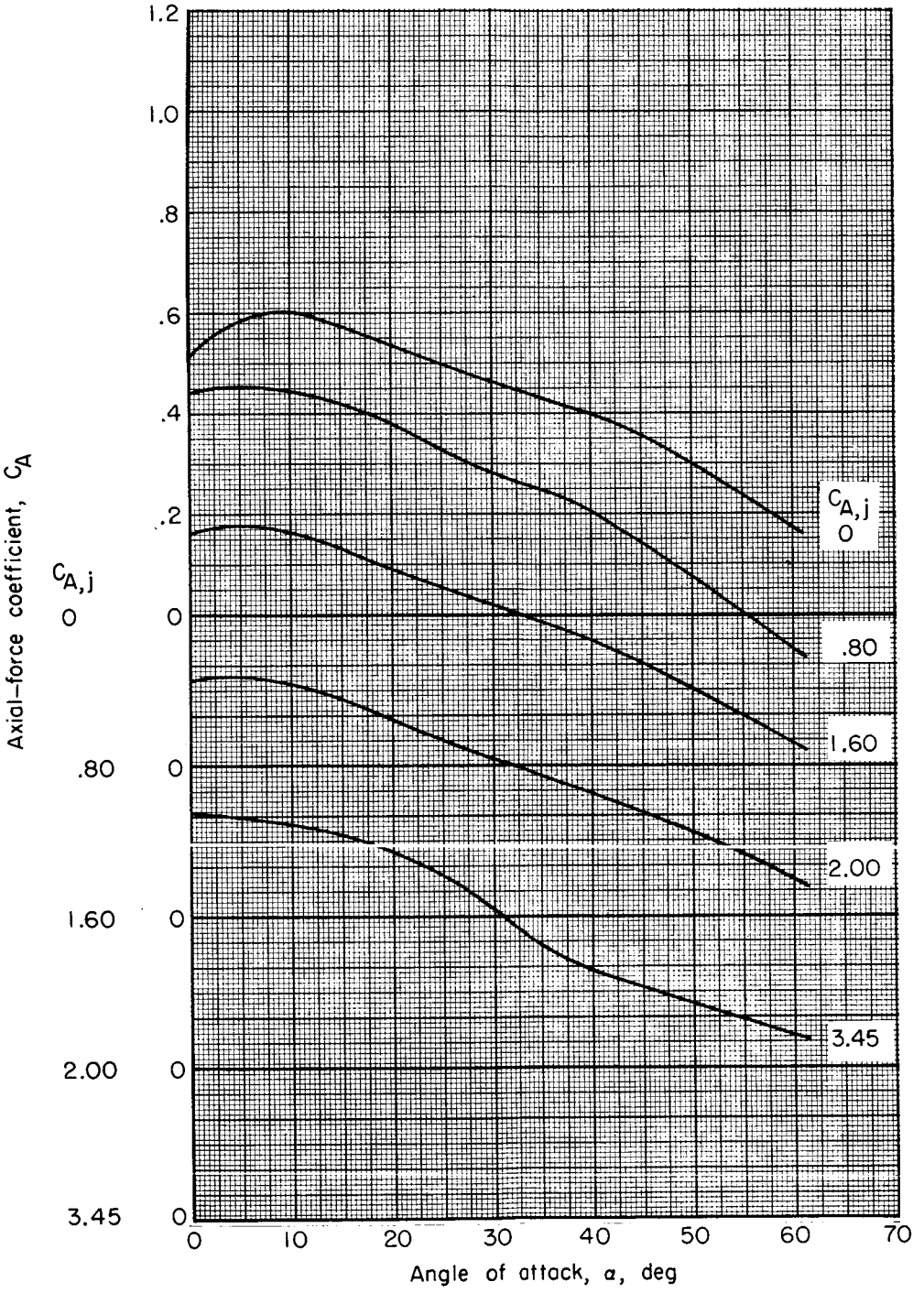

(b) M = 0.70.

Figure 19.- Continued.

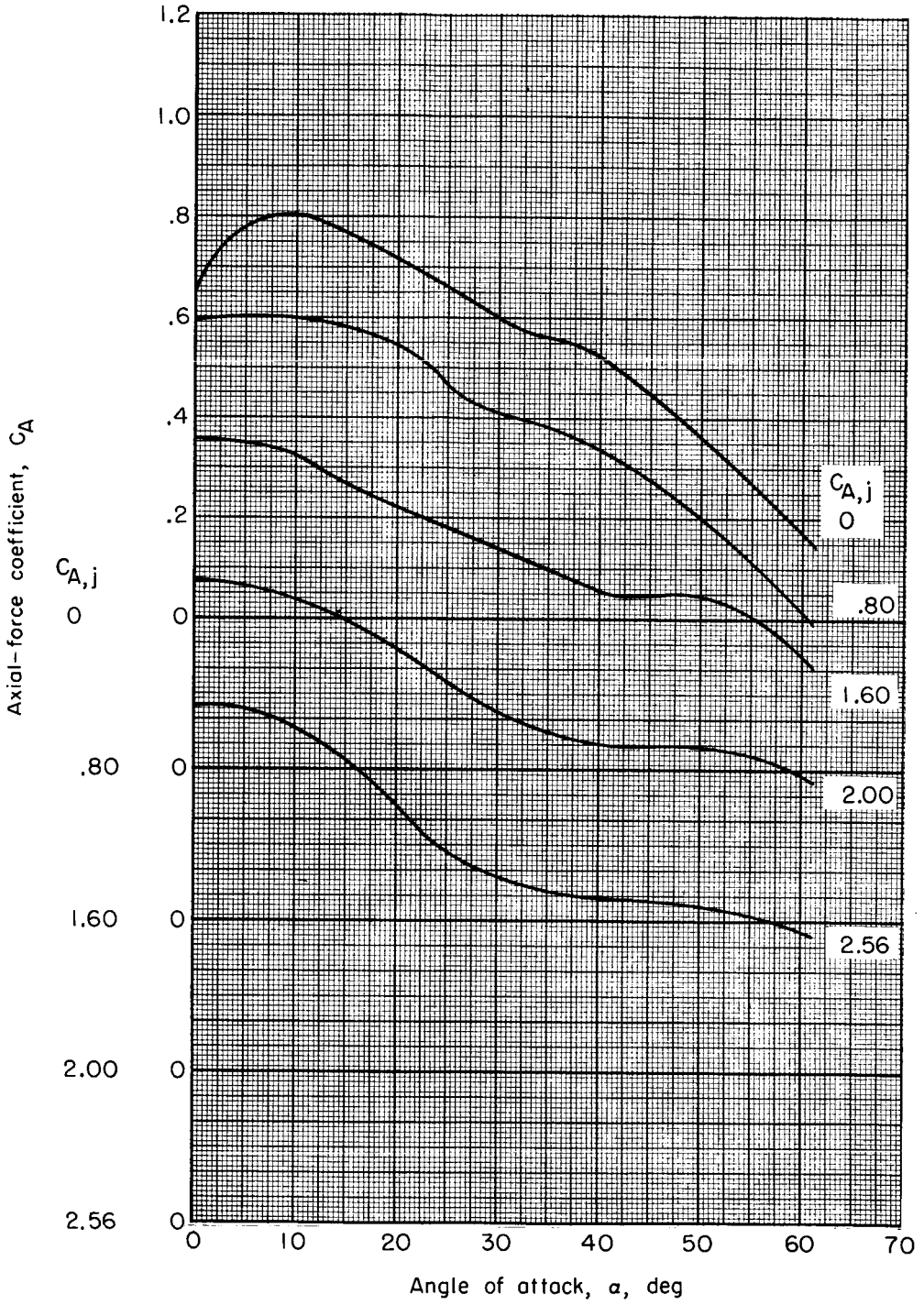

(c) M = 0.90.

Figure 19.- Continued.

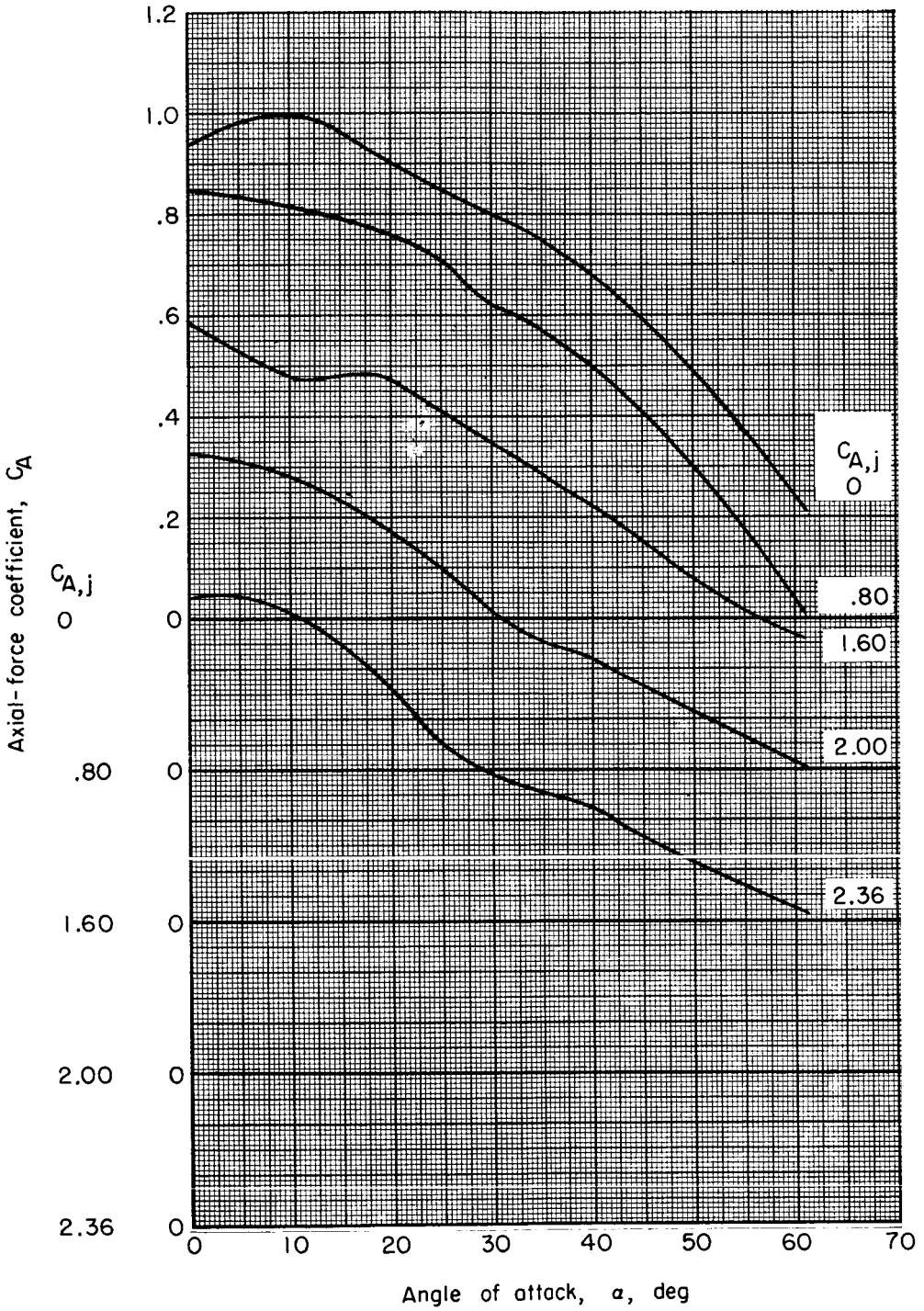

(d) M = 1.00.

Figure 19.- Continued.

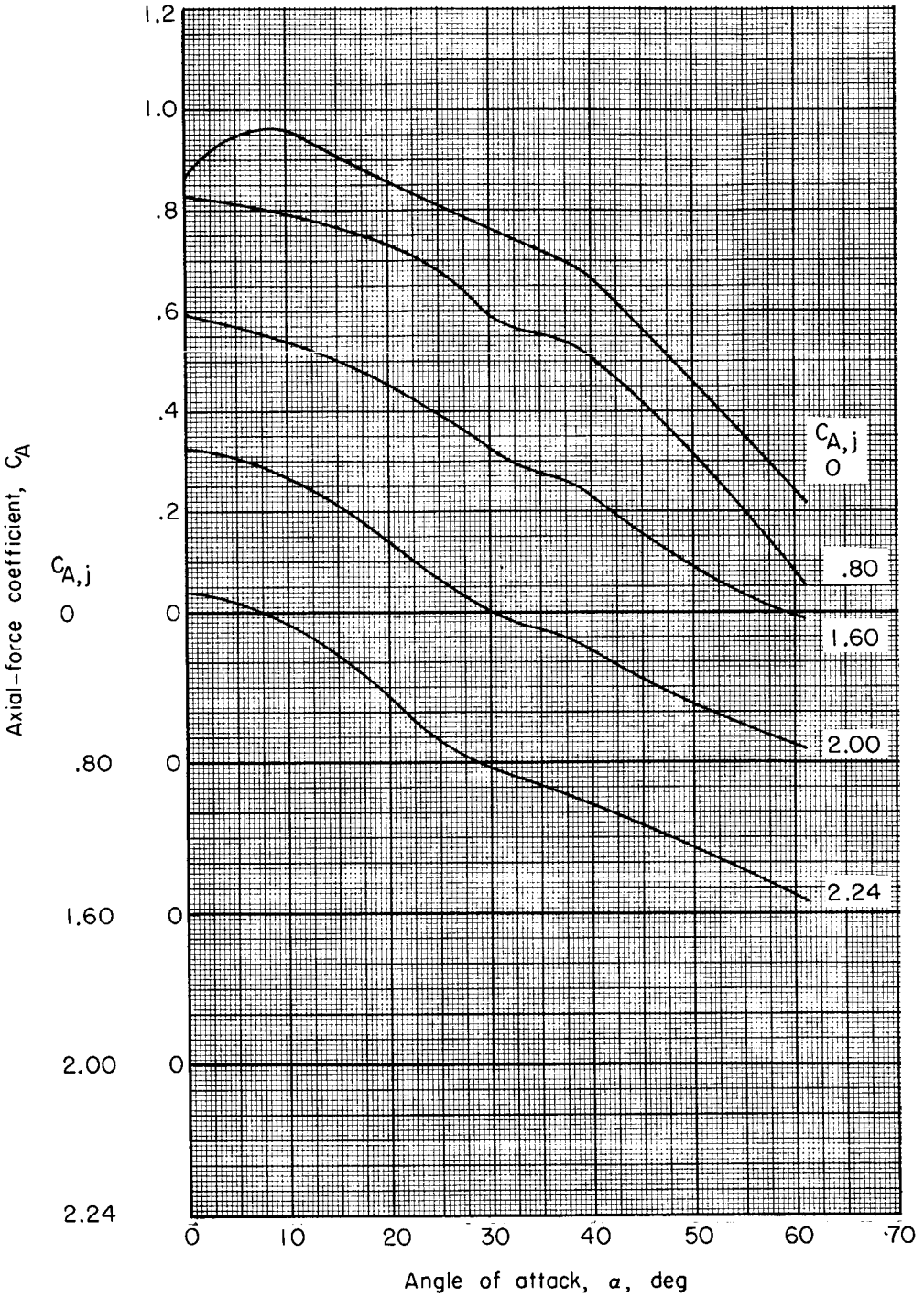

(e) M = 1.1.

Figure 19.- Continued.

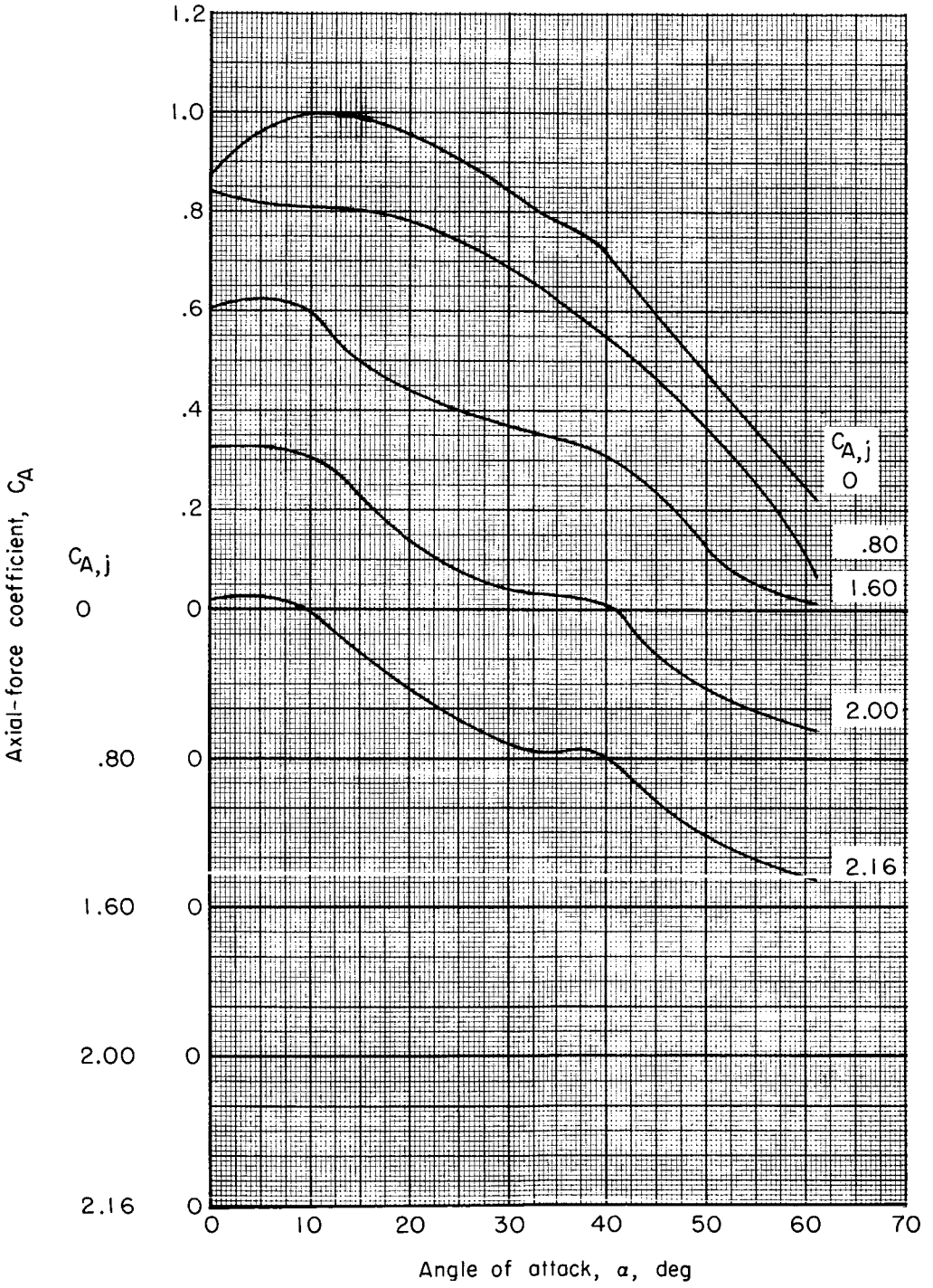

(f) M = 1.2.

Figure 19.- Continued.

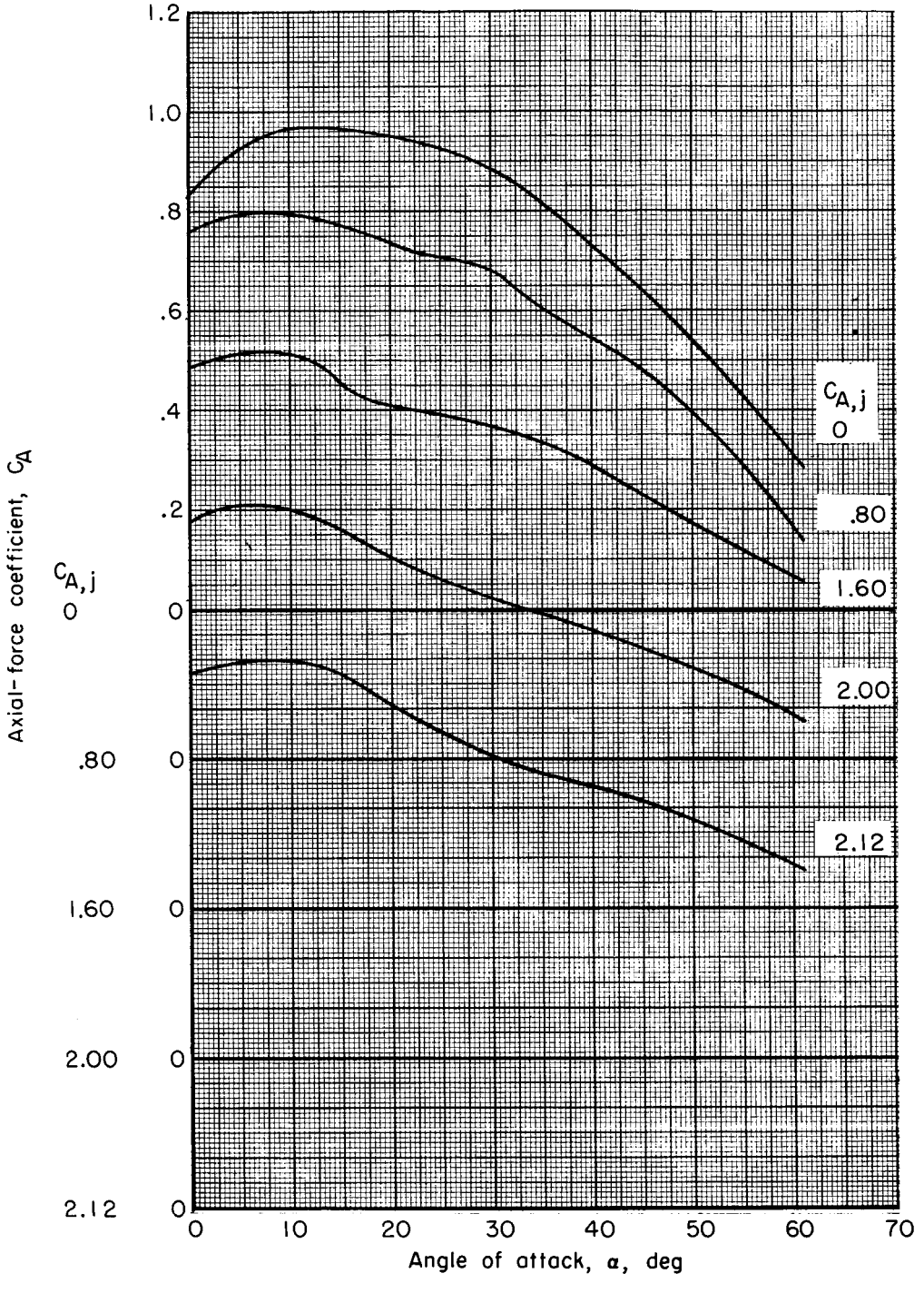

(g) M = 1.3.

Figure 19.- Concluded.

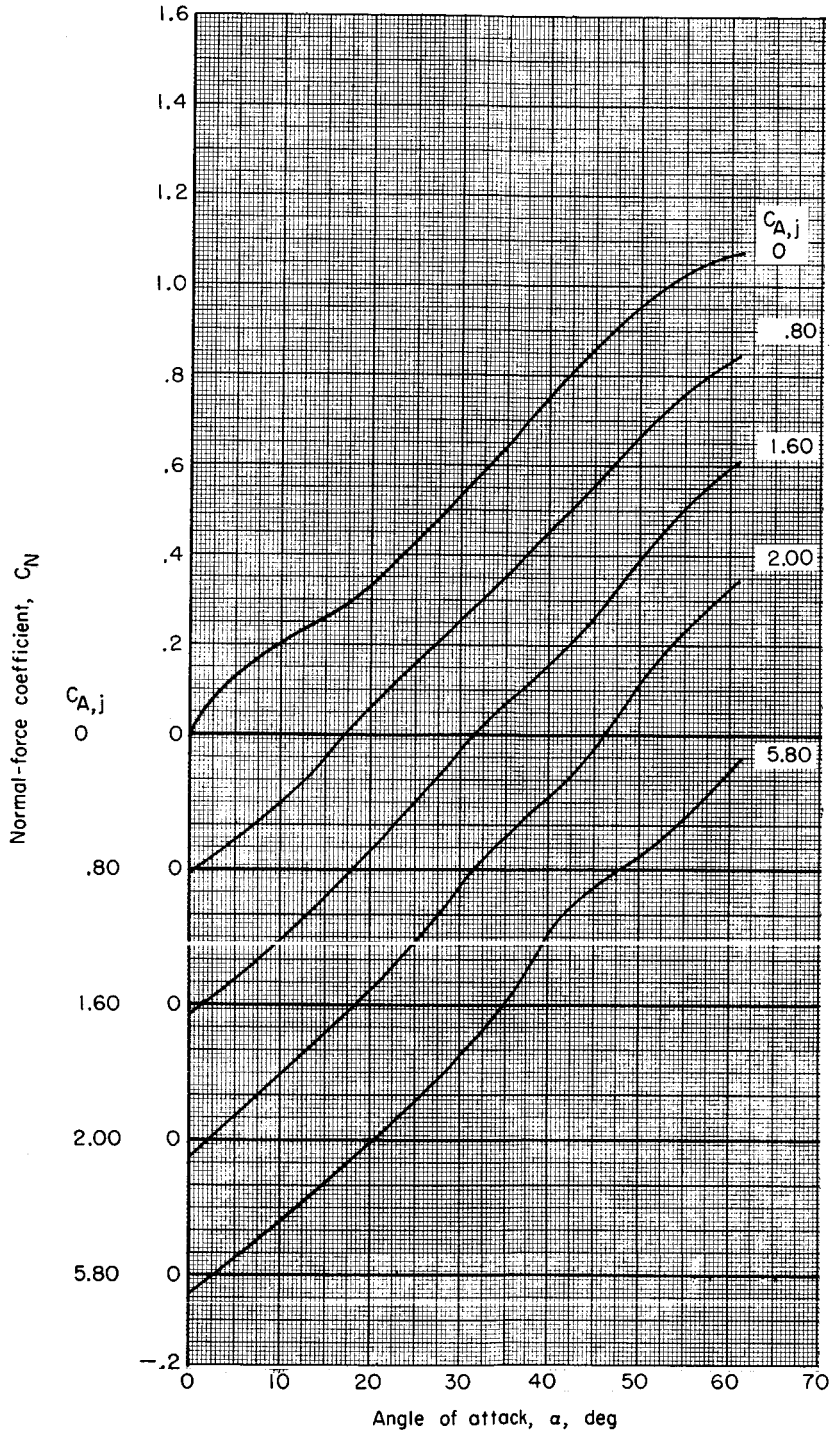

(a) M = 0.50.

Figure 20.- Variation of normal-force coefficient with angle of attack.

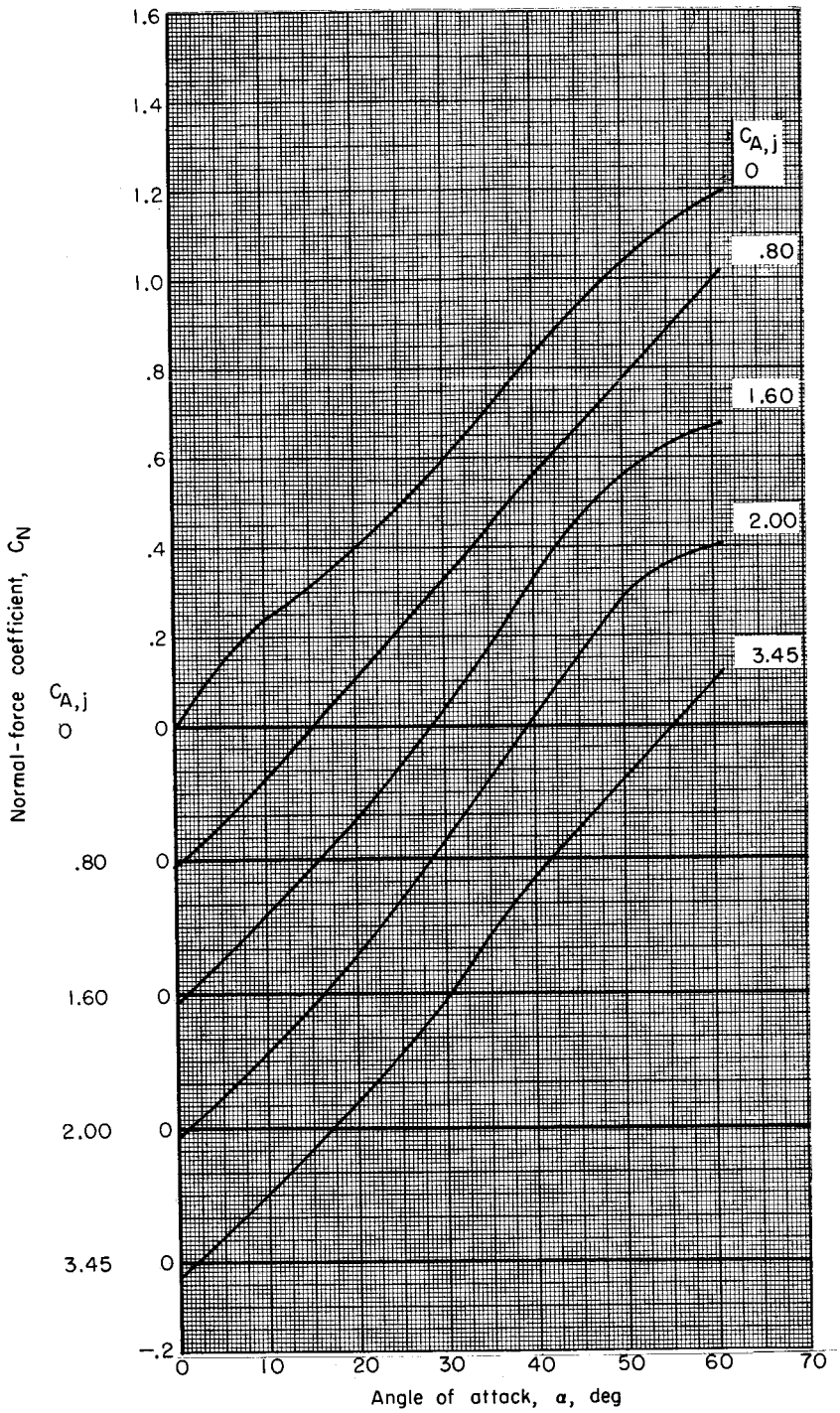

(b) M = 0.70.

Figure 20.- Continued.

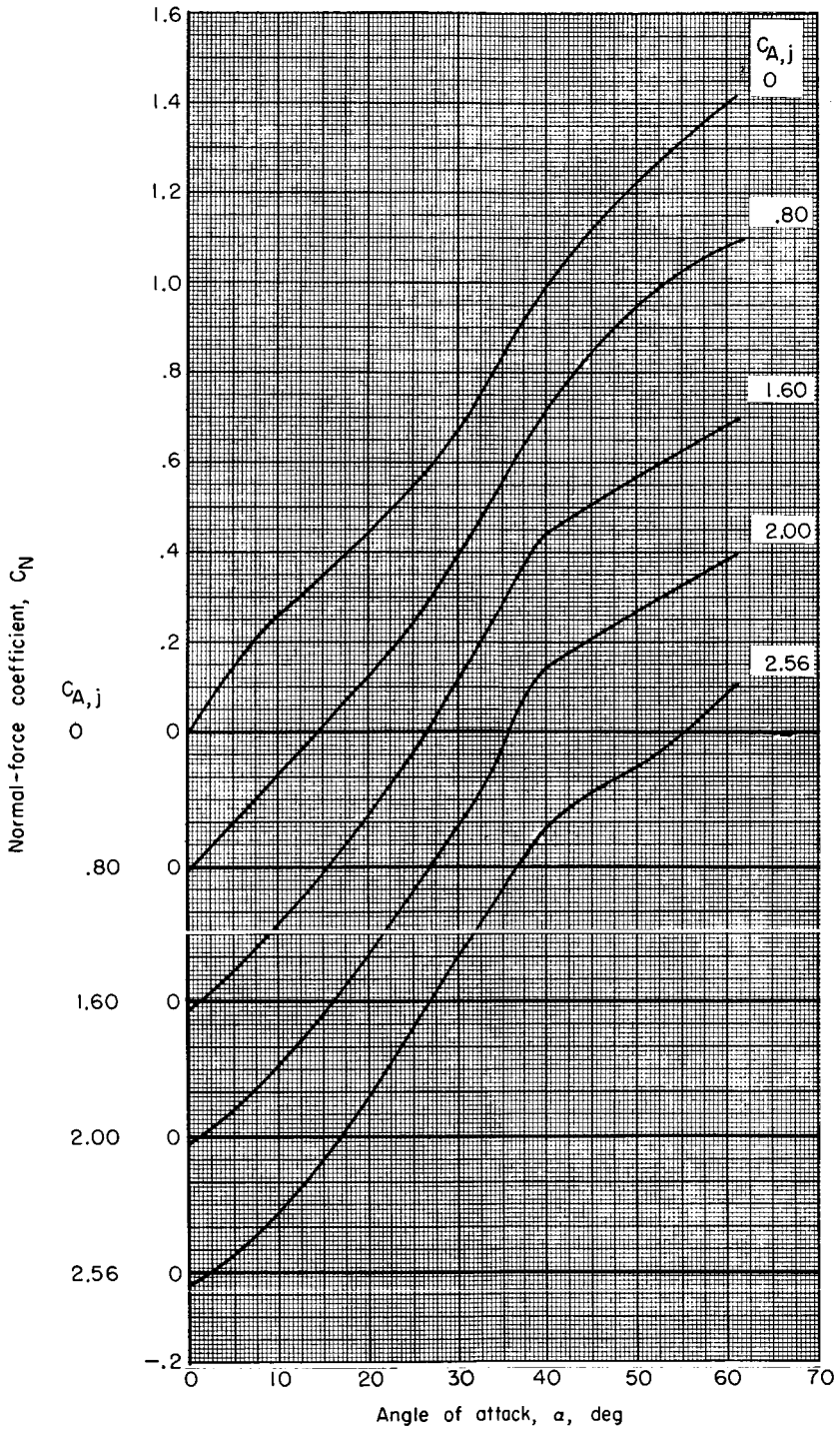

(c) M = 0.90.

Figure 20.- Continued.

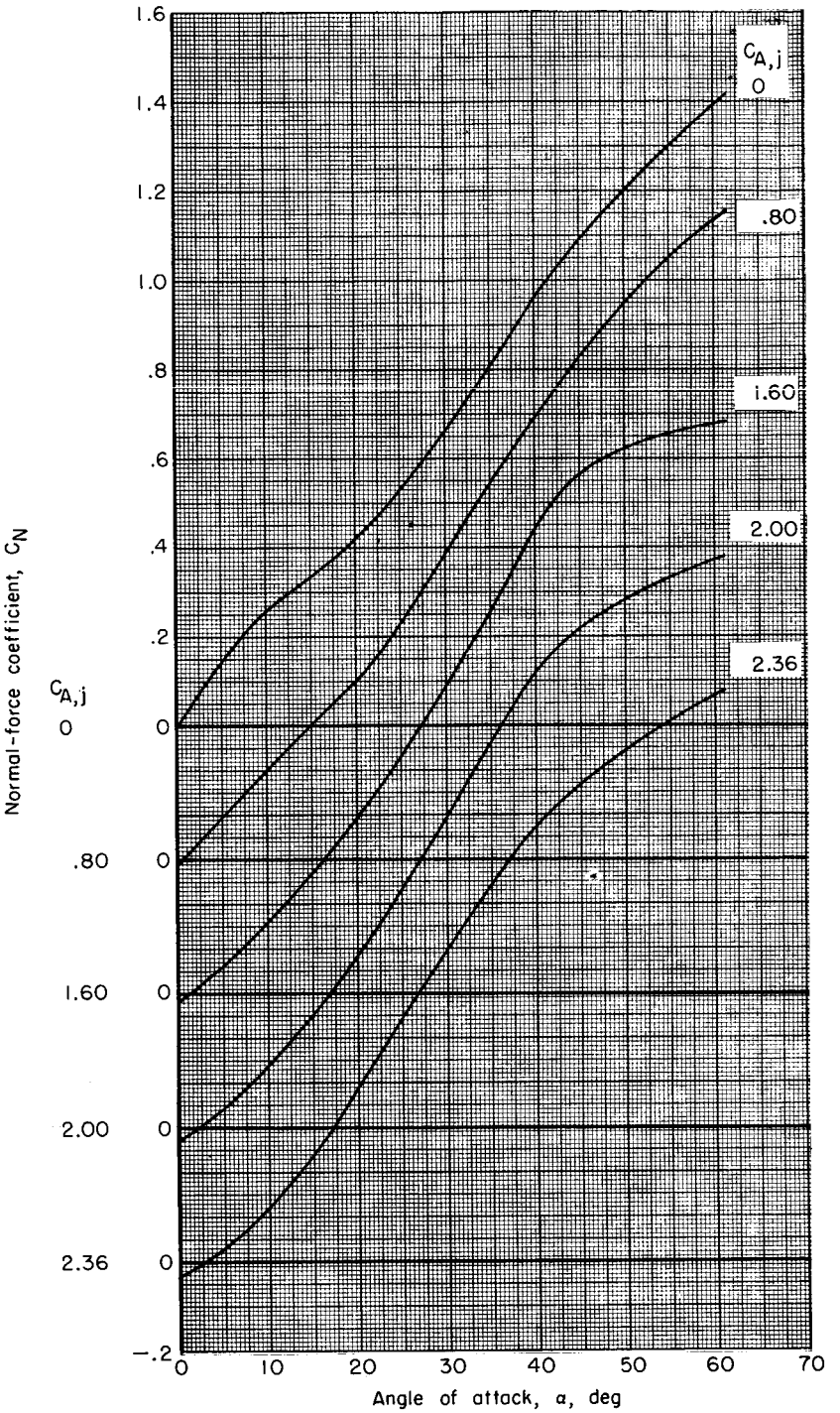

(d) M = 1.00.

Figure 20.- Continued.

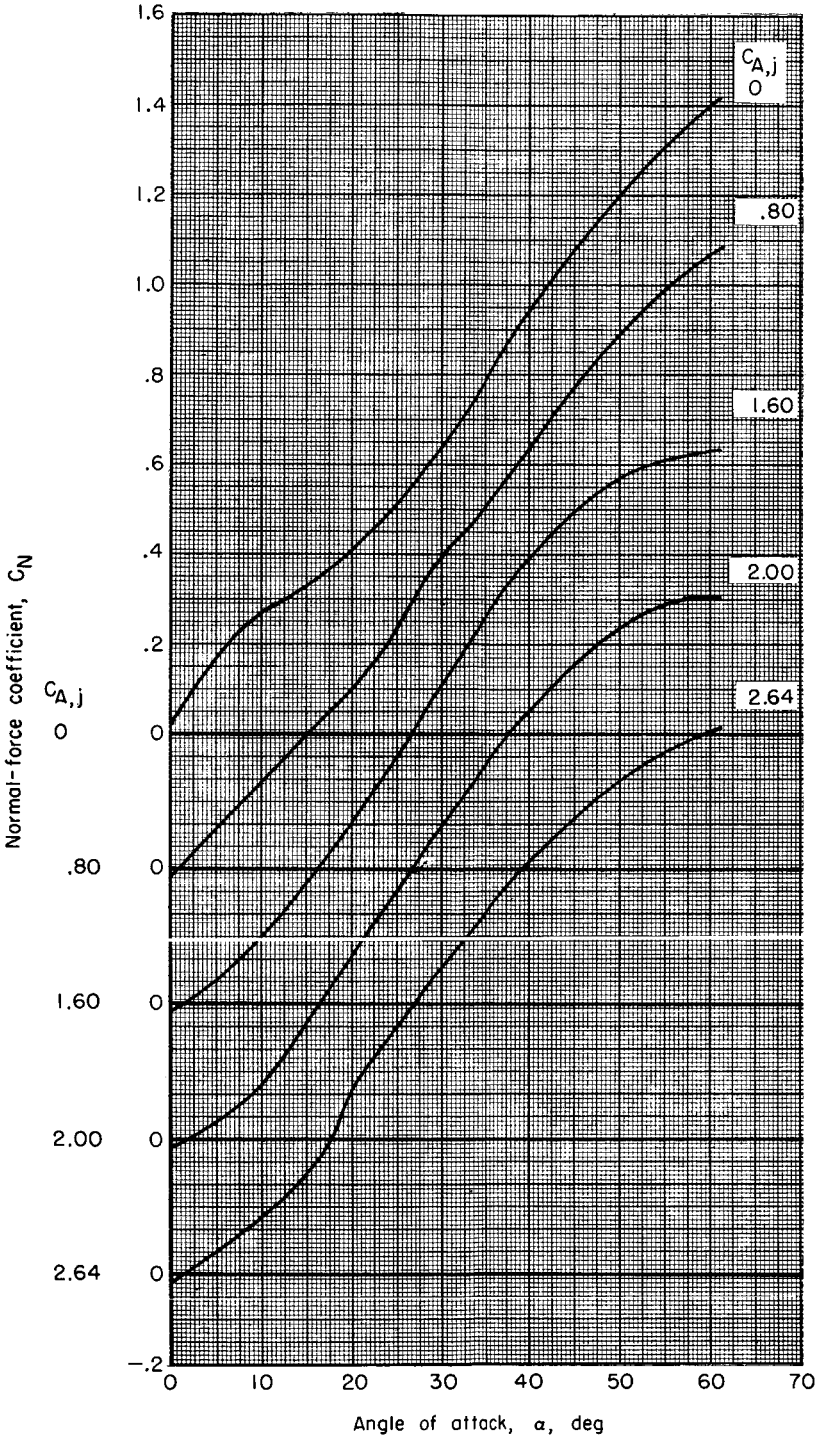

(e) M = 1.1.

Figure 20.- Continued.

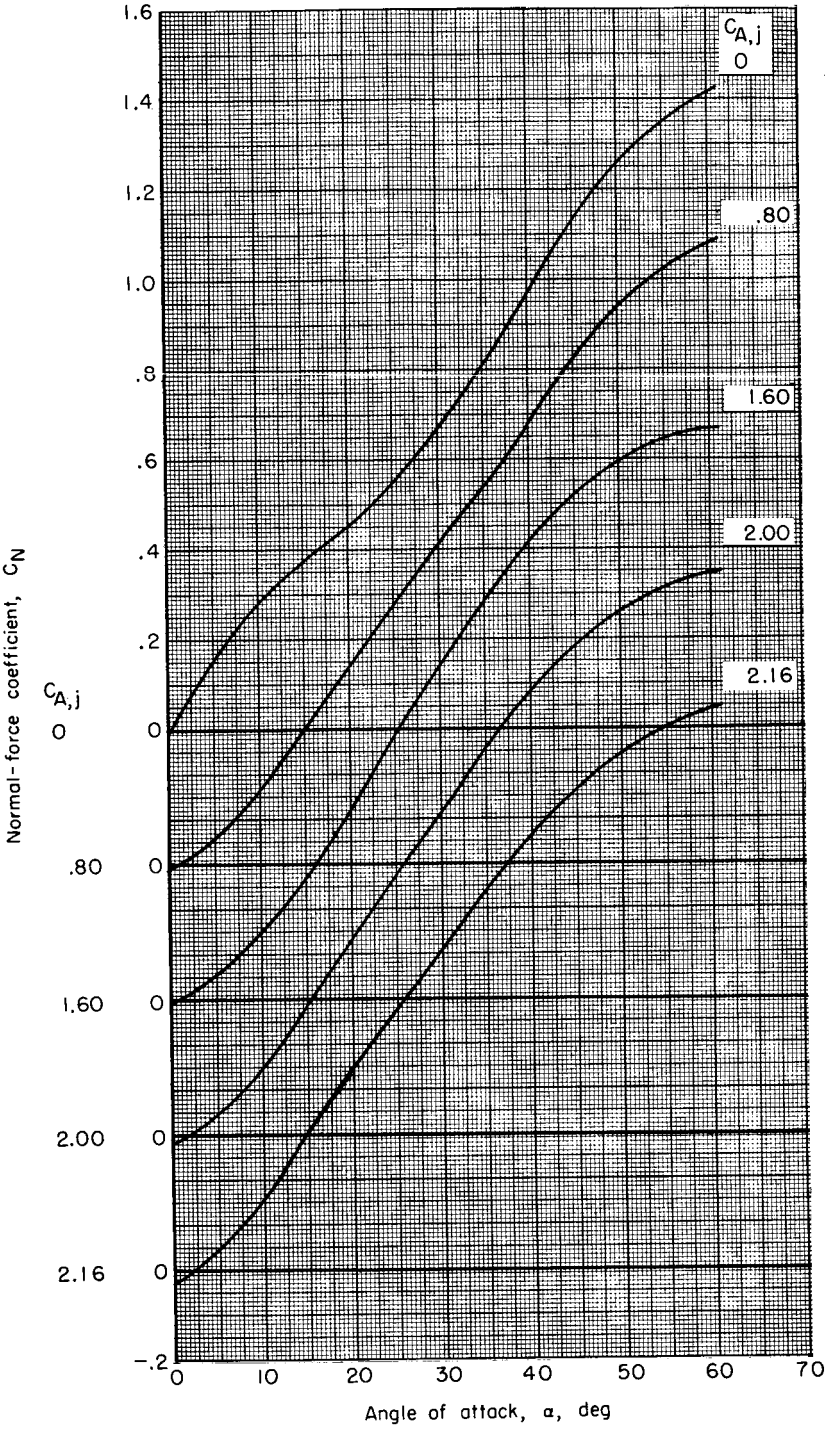

(f) M = 1.1.

Figure 20.- Continued.

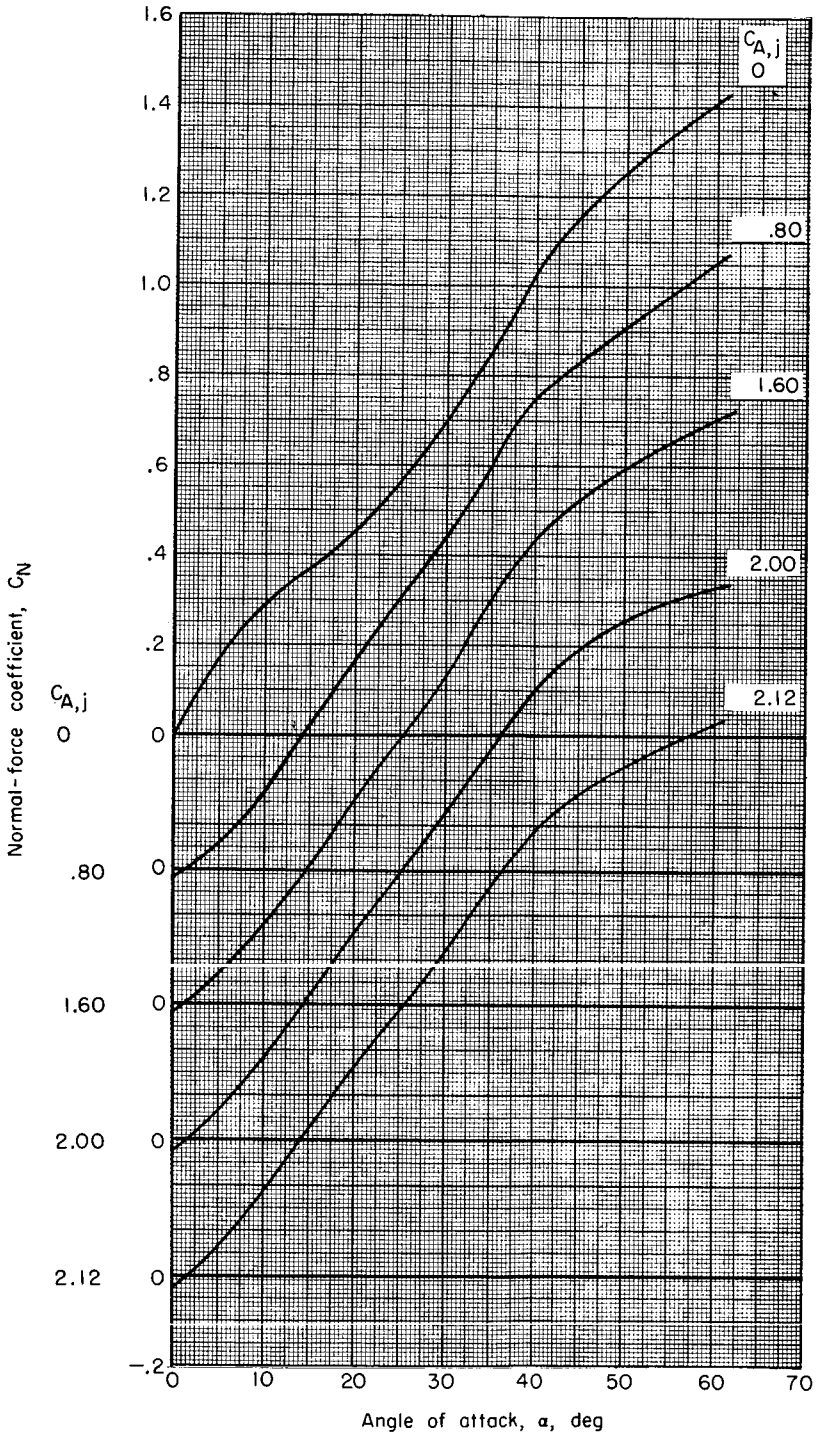

(g) M = 1.3.

Figure 20.- Concluded.

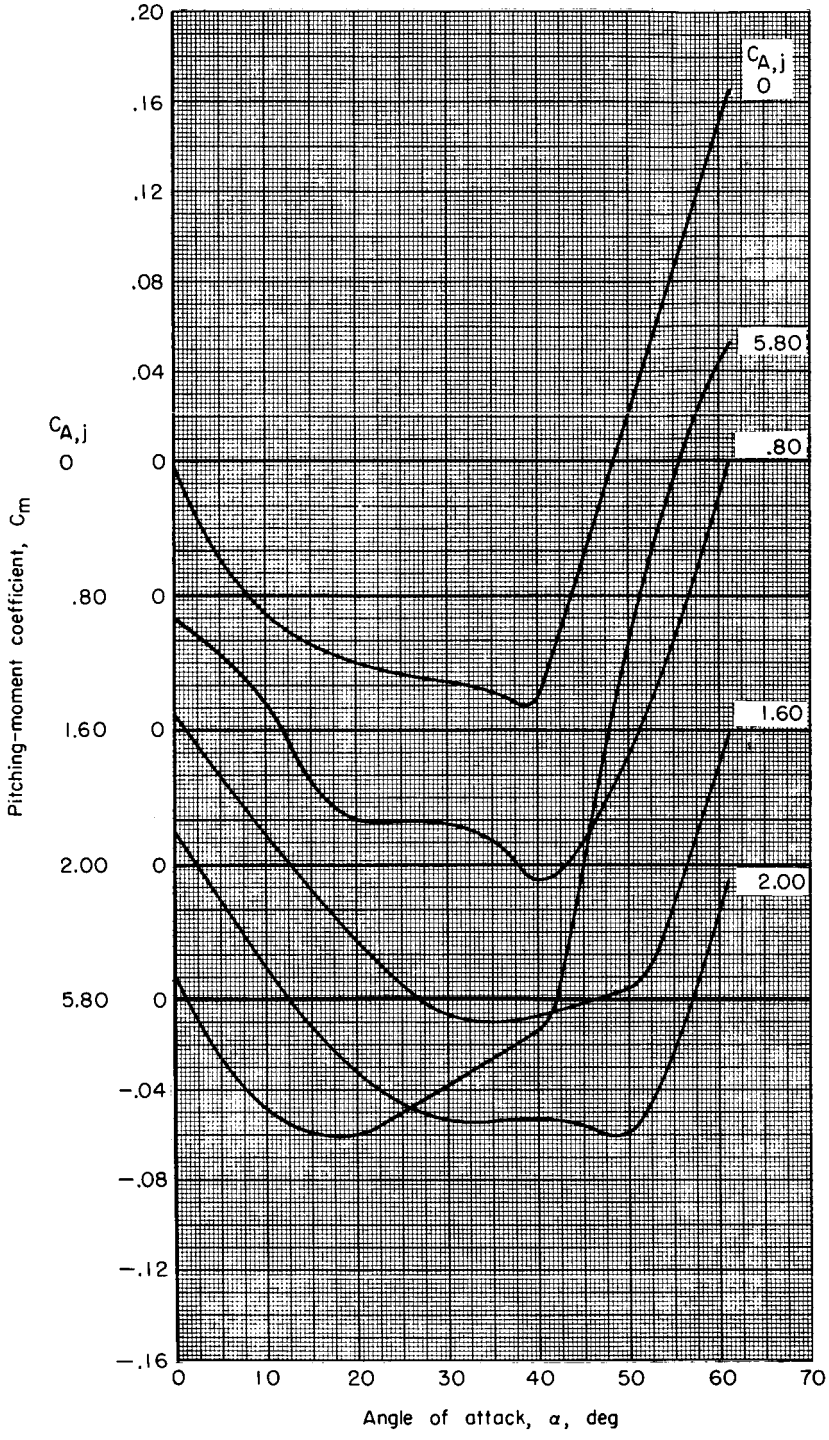

(a) M = 0.50.

Figure 21.- Variation of pitching-moment coefficient with angle of attack.

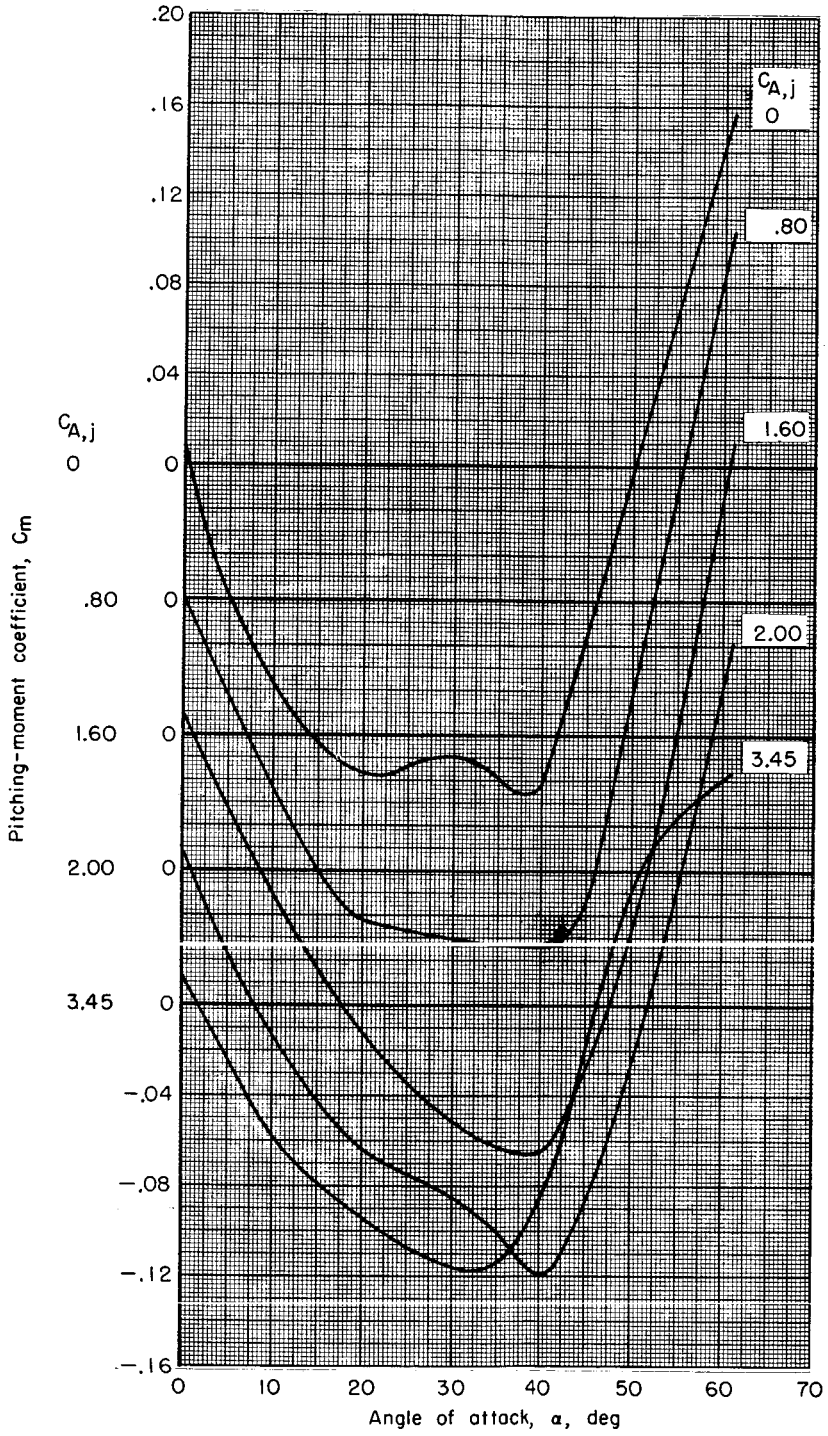

(b) M = 0.70.

Figure 21.- Continued.

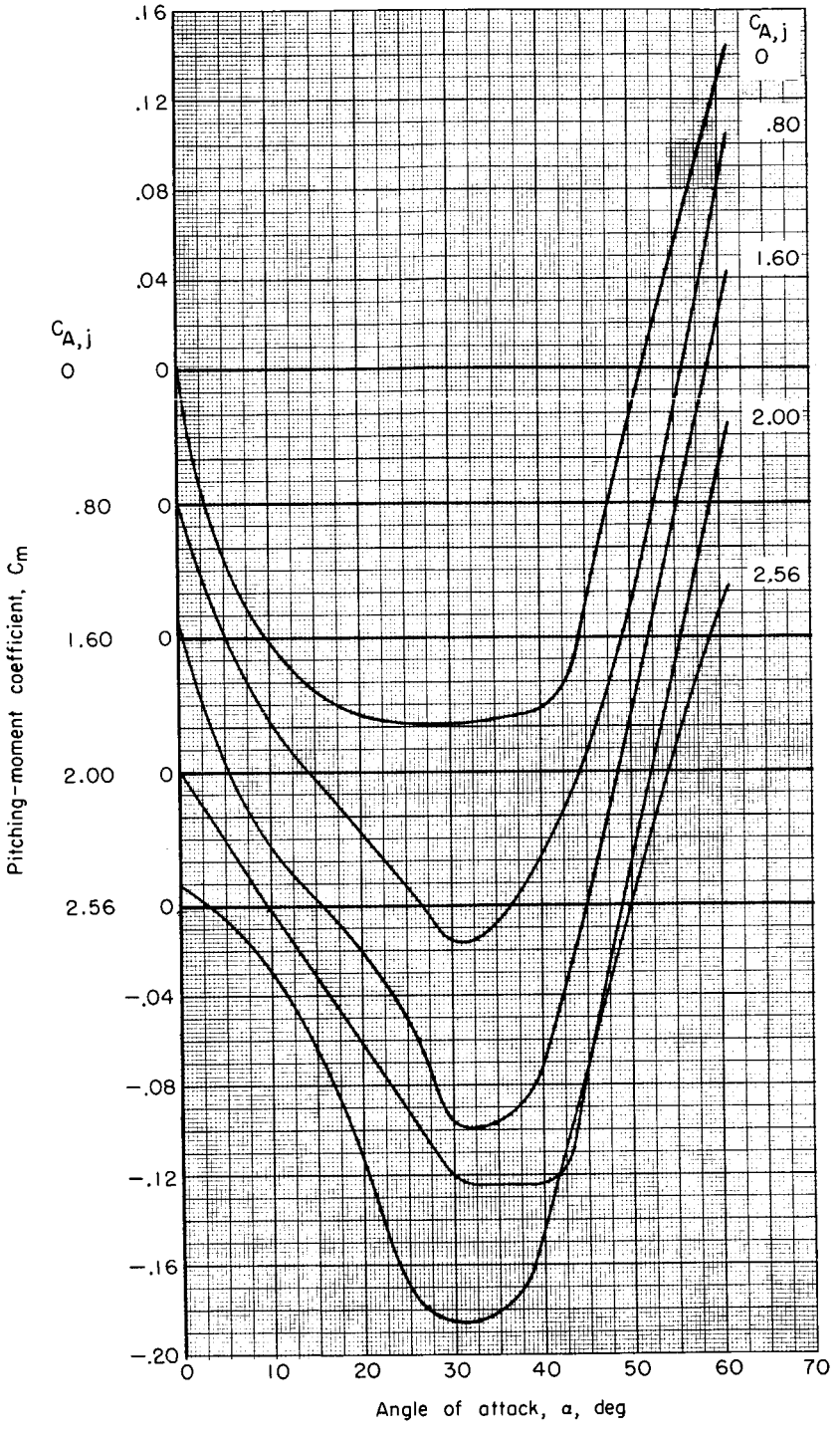

(c) M = 0.90.

Figure 21.- Continued.

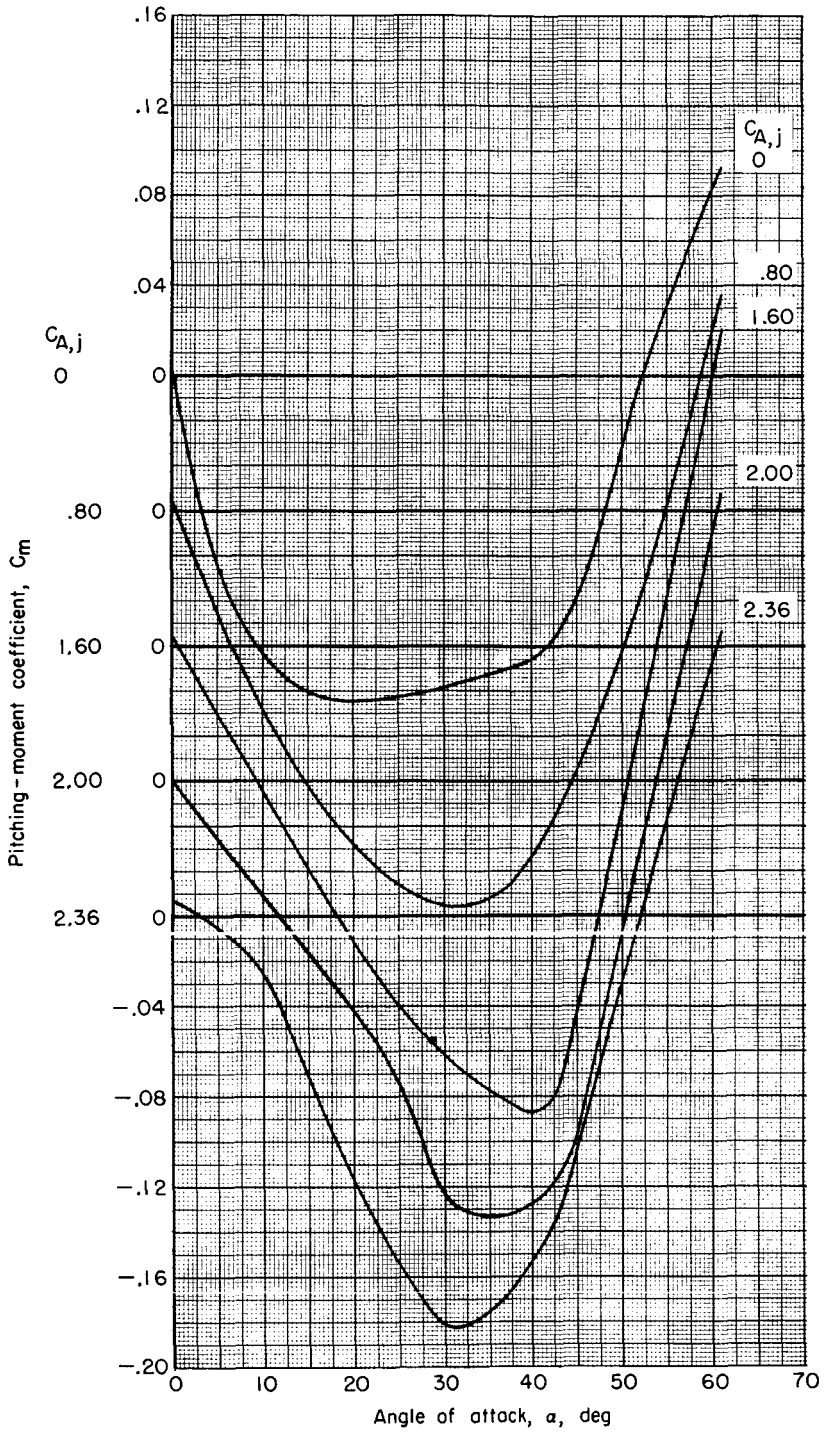

(d) M = 1.00.

Figure 21.- Continued.

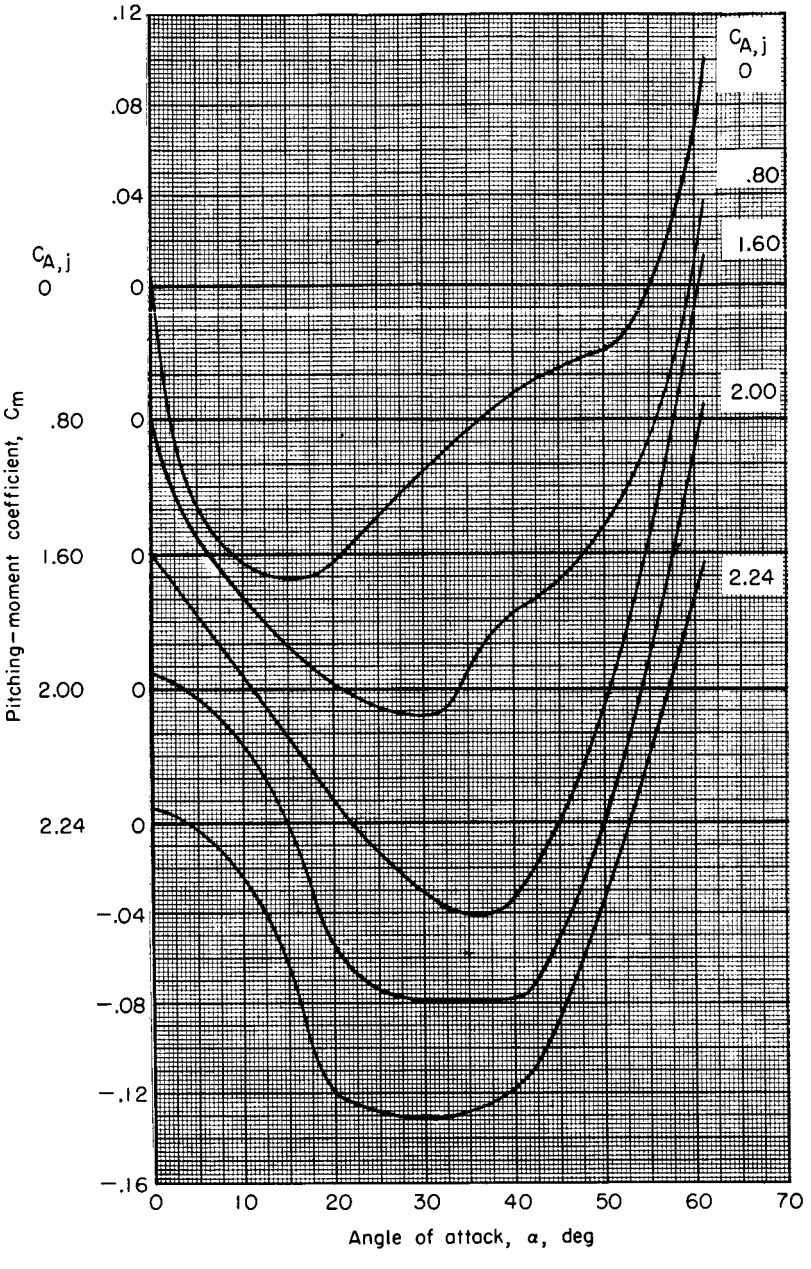

(e) M = 1.1.

Figure 21.- Continued.

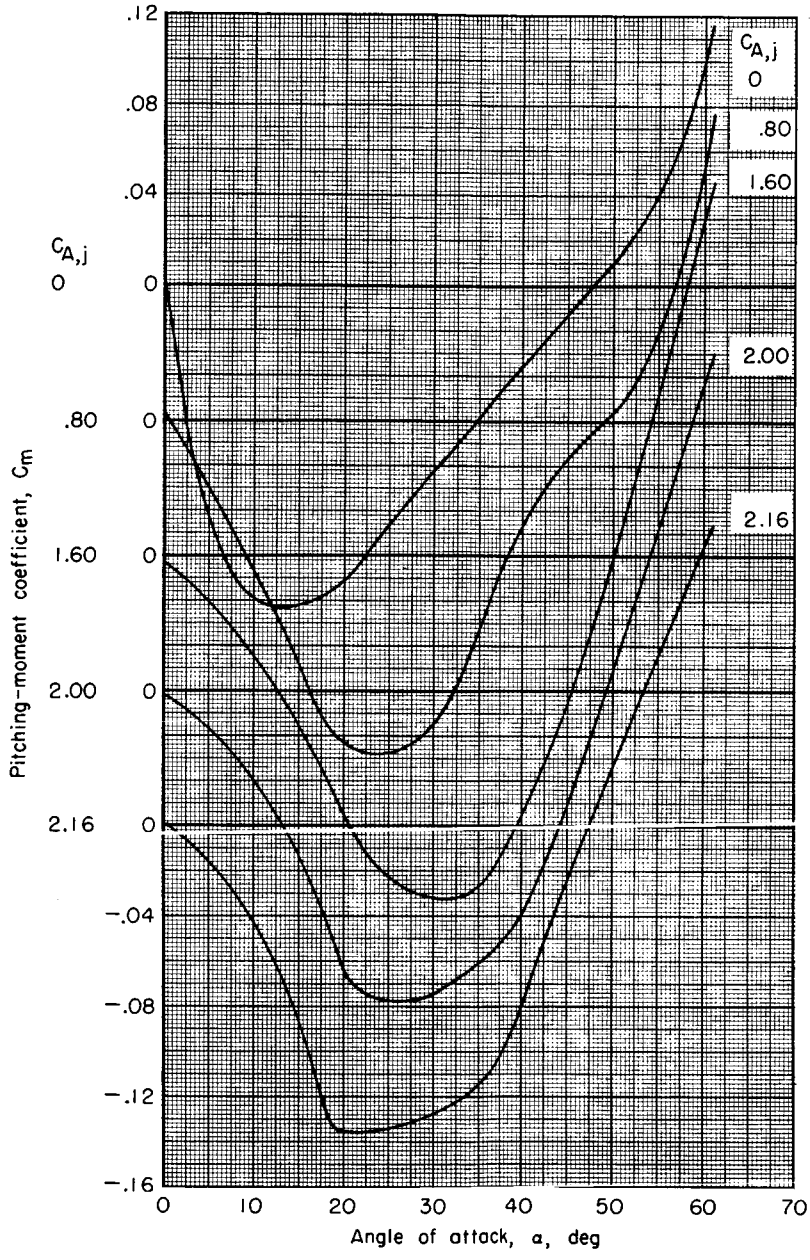

(f) M = 1.2.

Figure 21.- Continued.

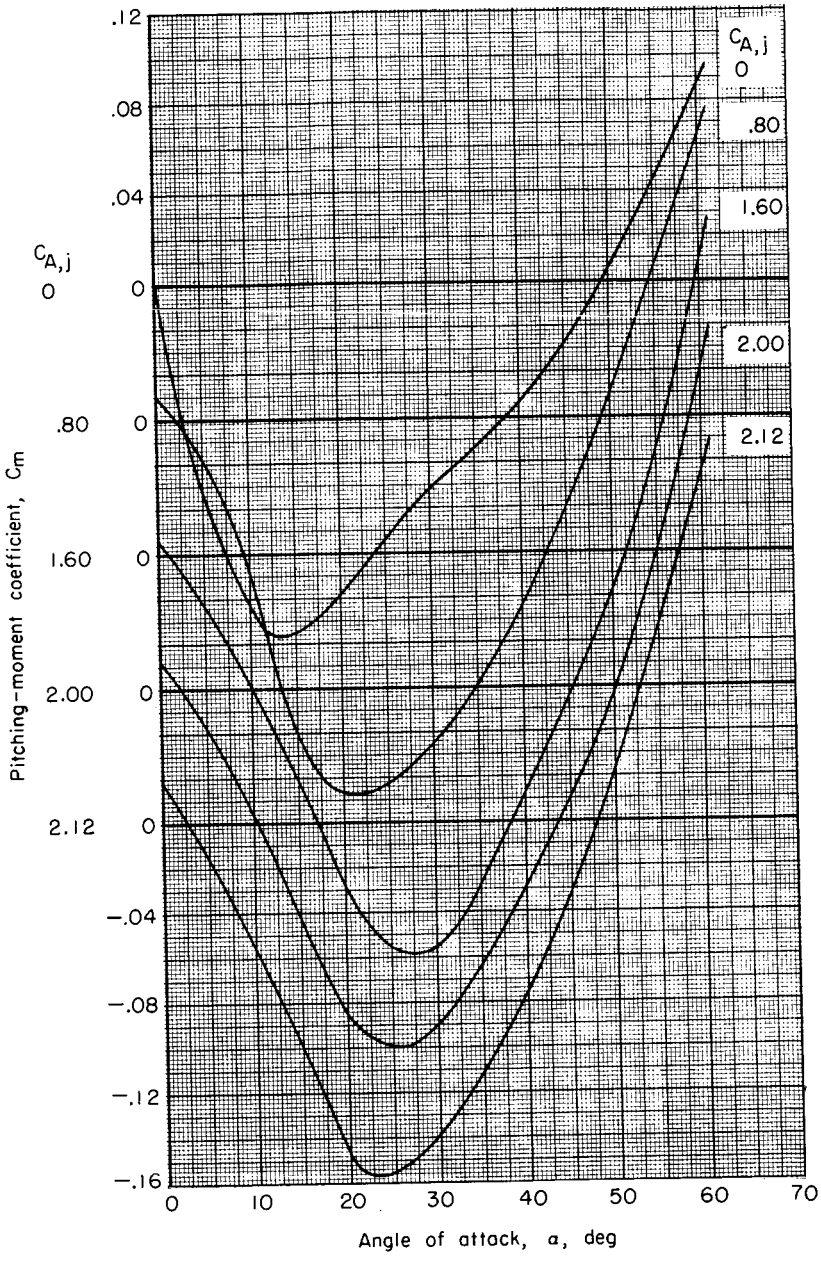

(g) M = 1.3.

Figure 21.- Concluded.

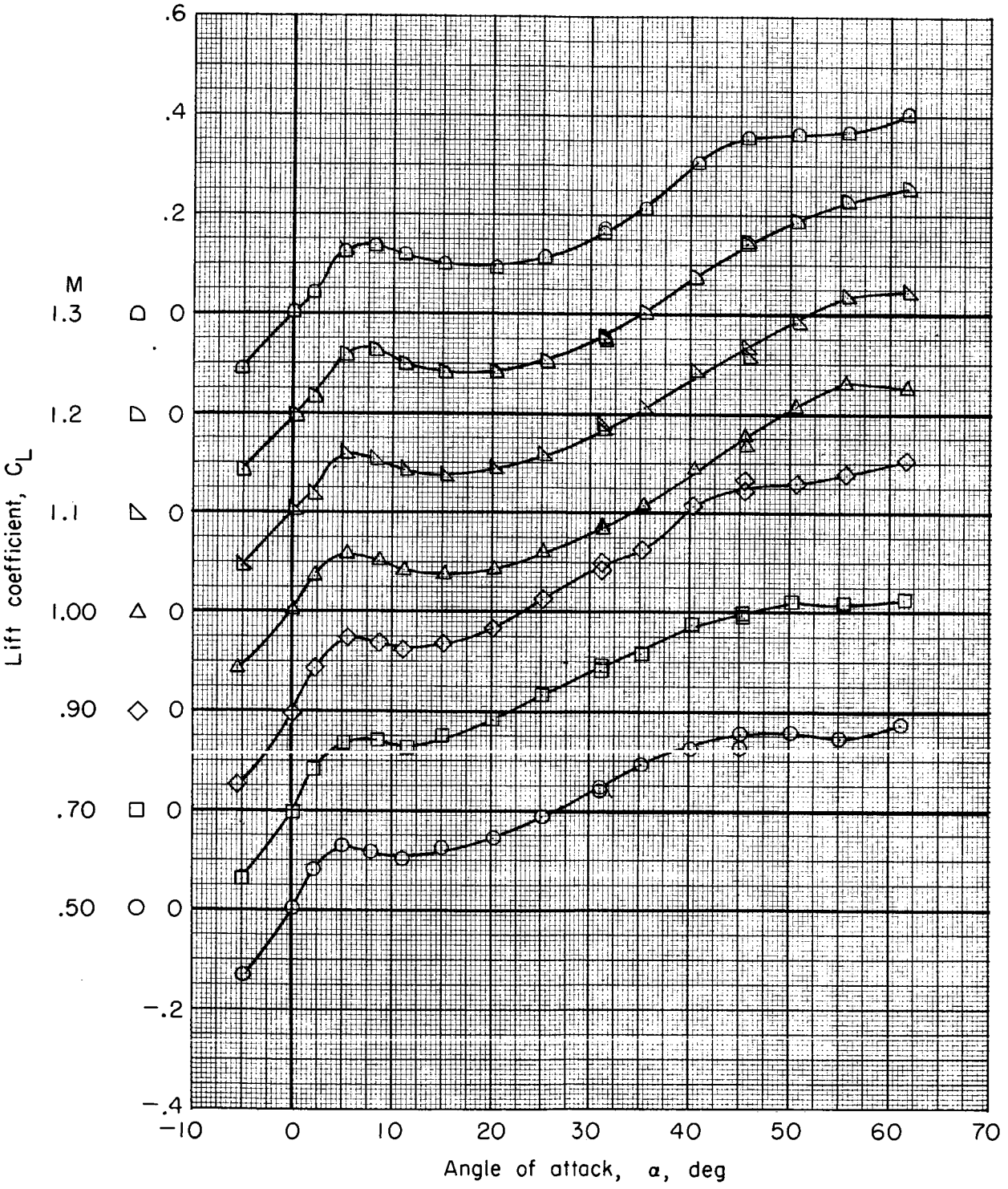

Figure 22.- Variation of lift coefficient with angle of attack. $C_{A,j} = 0$.

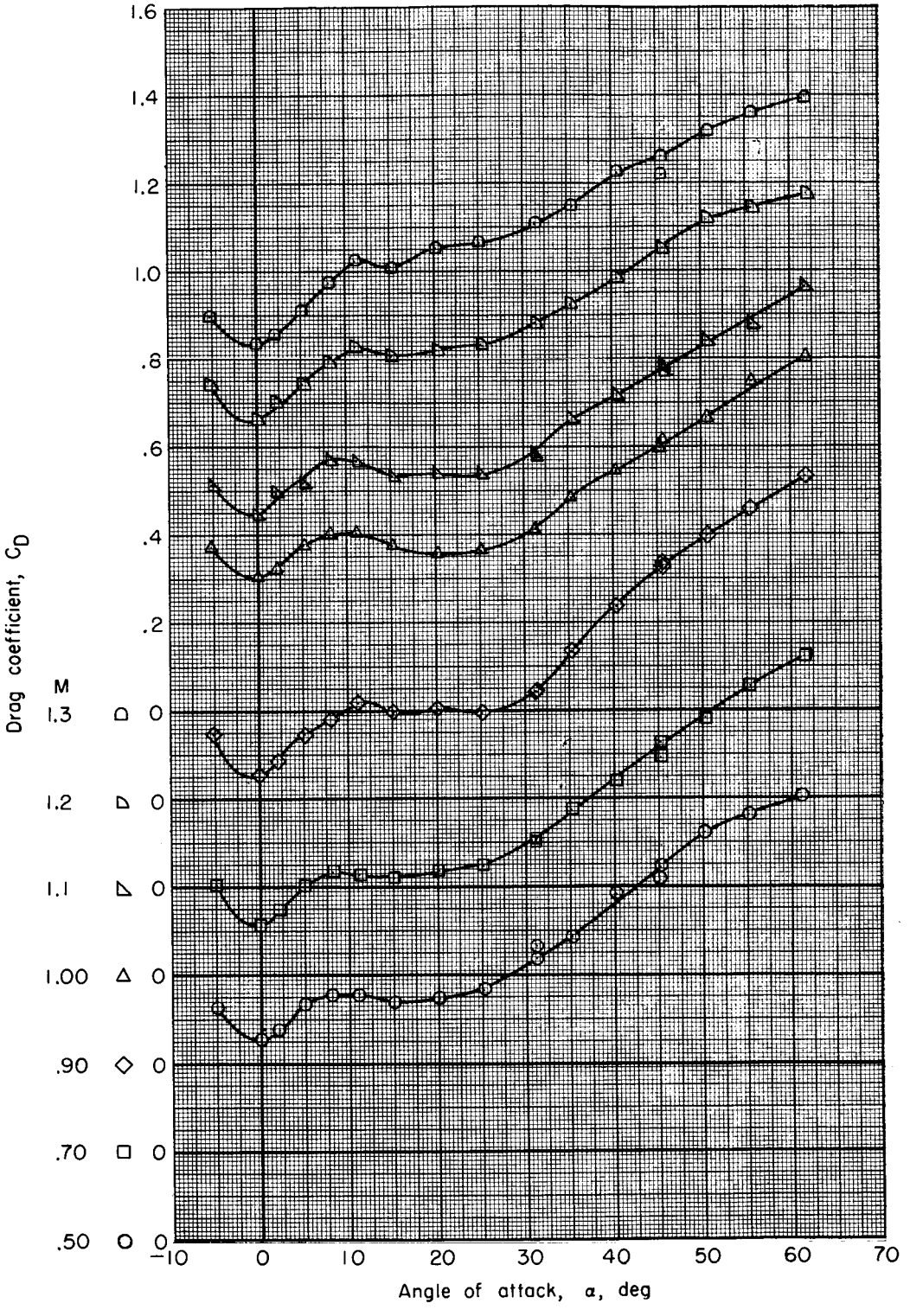

Figure 23.- Variation of drag coefficient with angle of attack. $C_{A,j} = 0$.

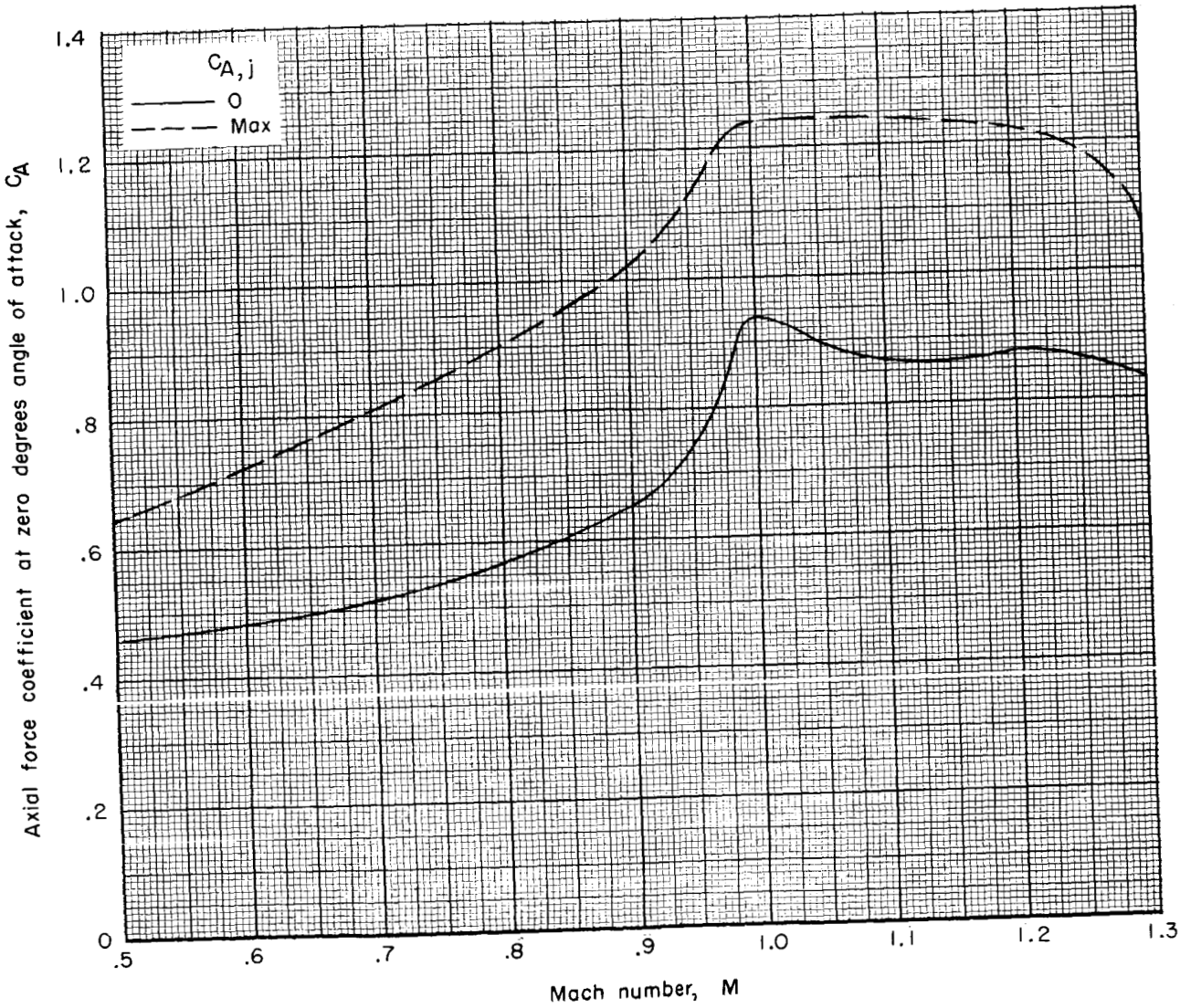

Figure 24.- Variation of total axial-force coefficient at zero angle of attack with Mach number.

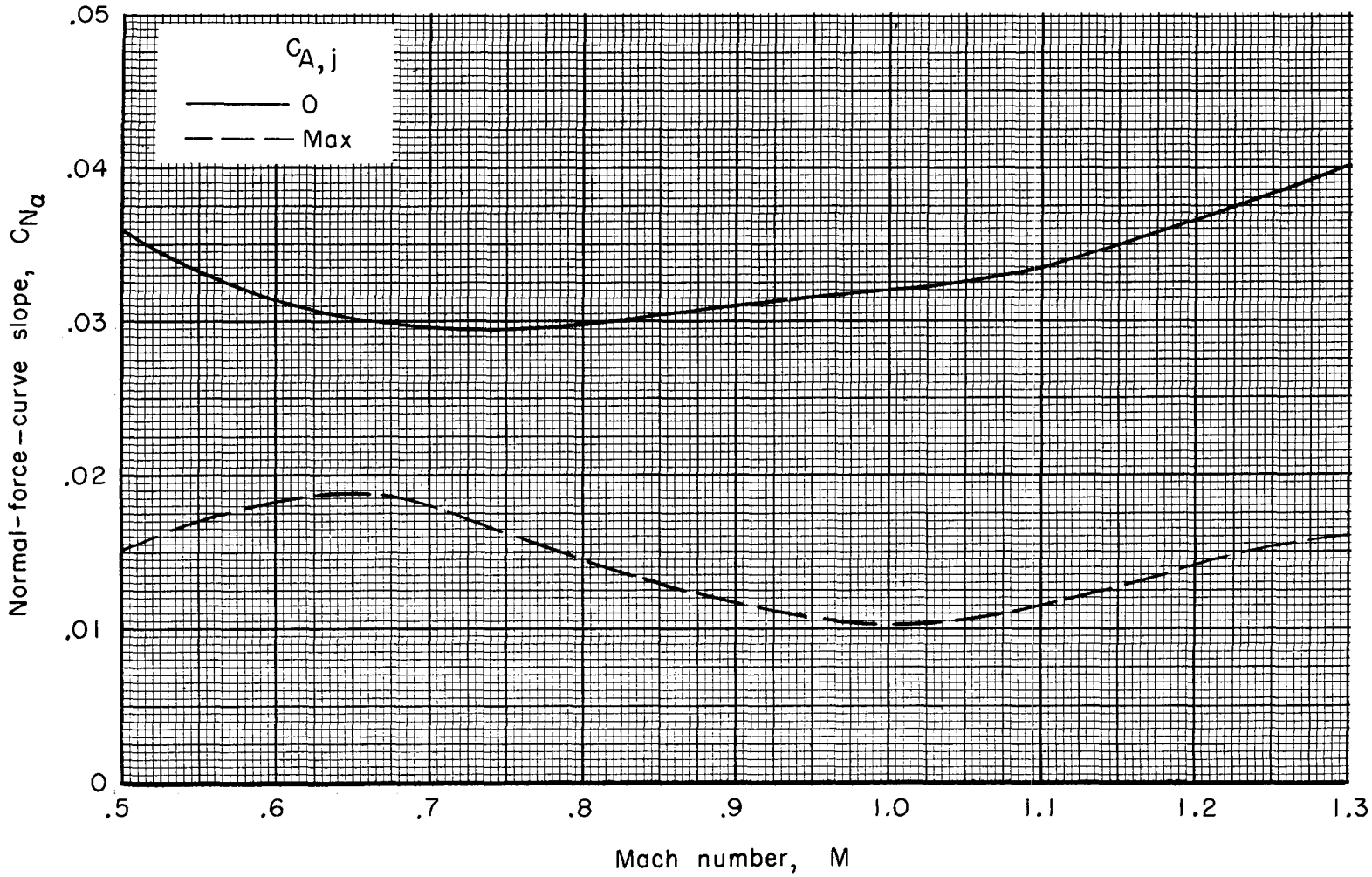

Figure 25.- Variation of total normal-force-curve slope with Mach number.

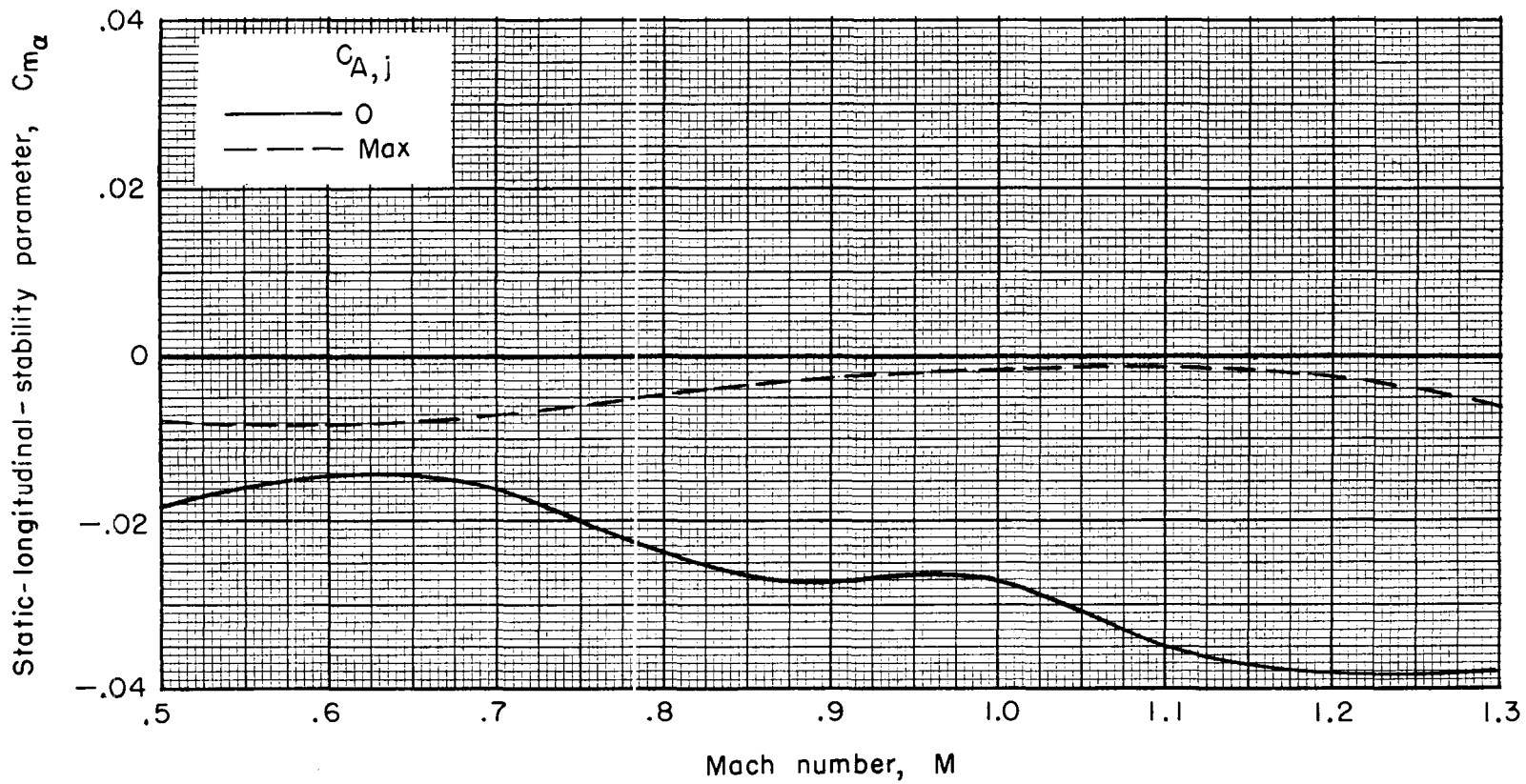

Figure 26.- Variation of total static-longitudinal-stability parameter with Mach number.

CO[redacted]

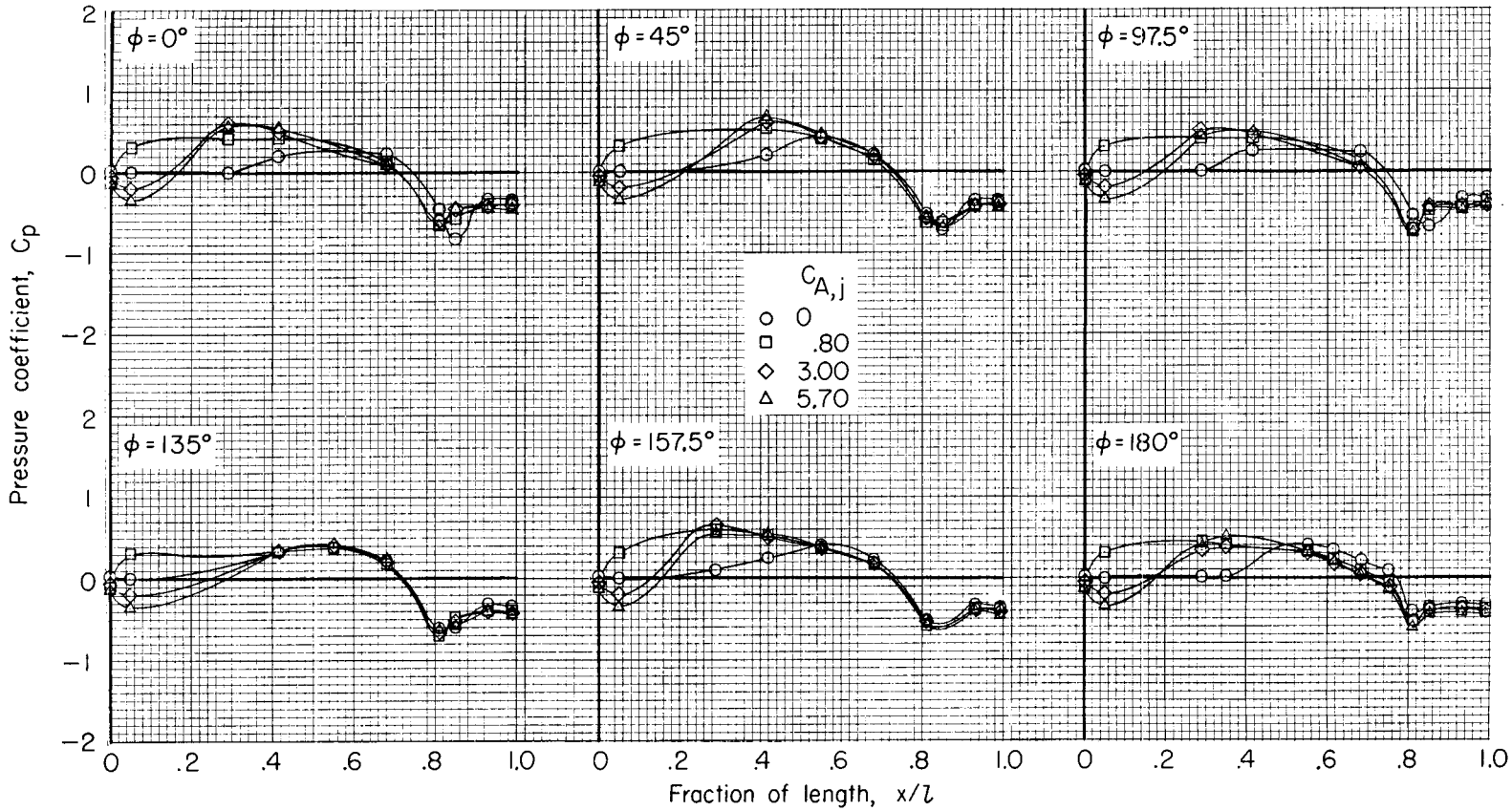

(a) $\alpha = 0^0$.

Figure 27.- Pressure distributions around command module at $M = 0.5$.

CON[redacted]

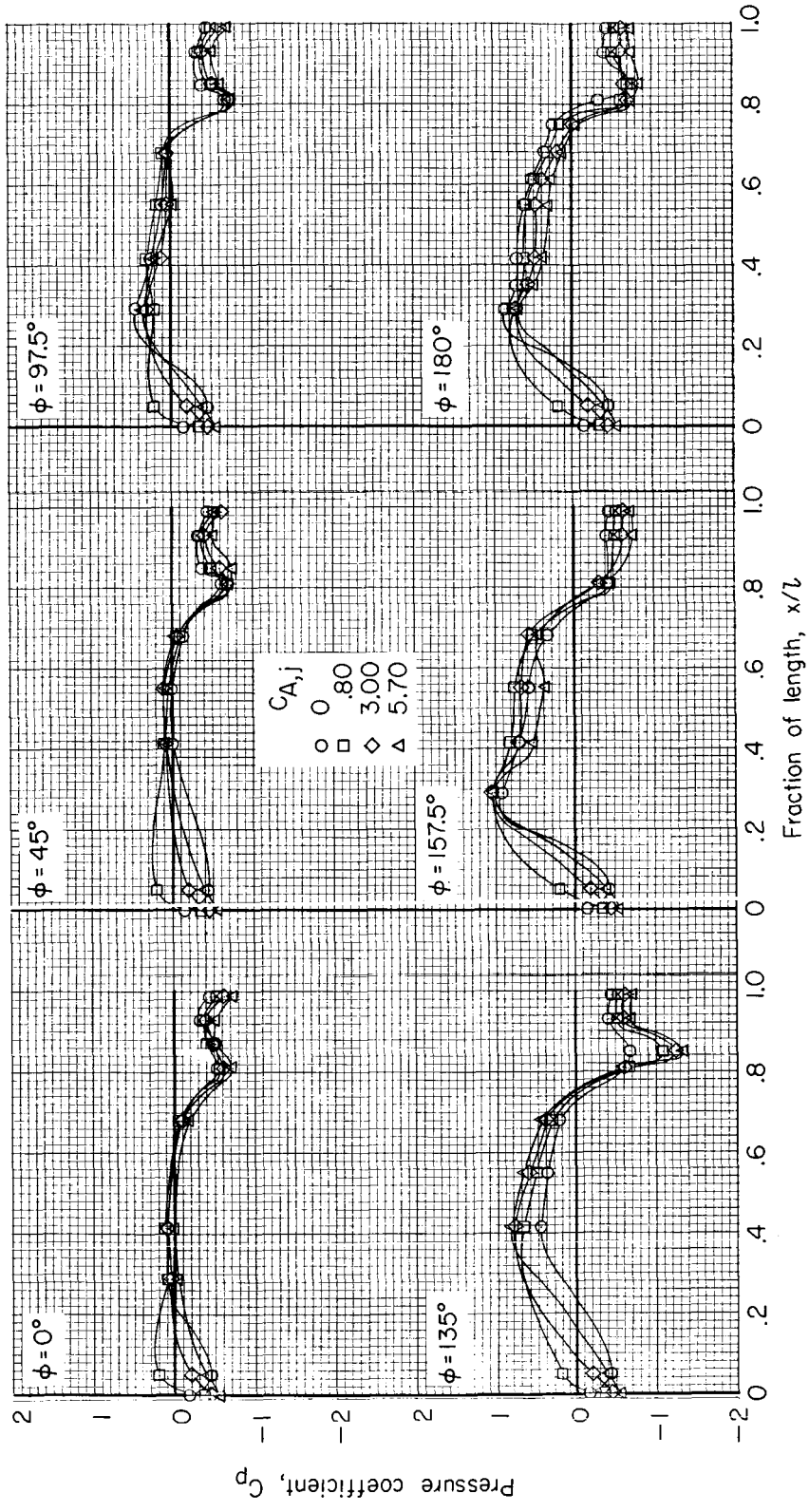

(b) $\alpha = 15^0$.

Figure 27.- Continued.

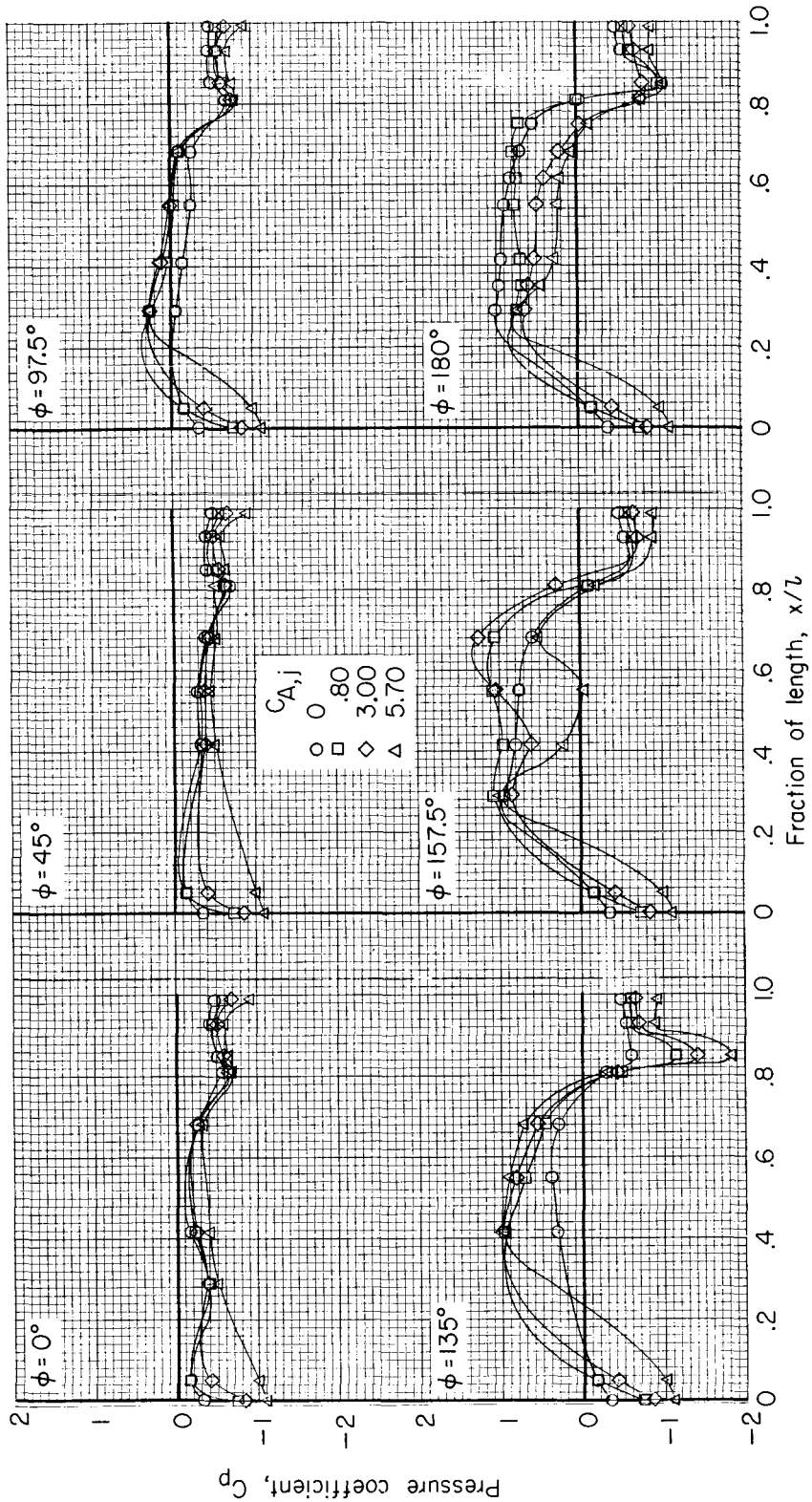

(c) $\alpha = 31°$.

Figure 27.- Continued.

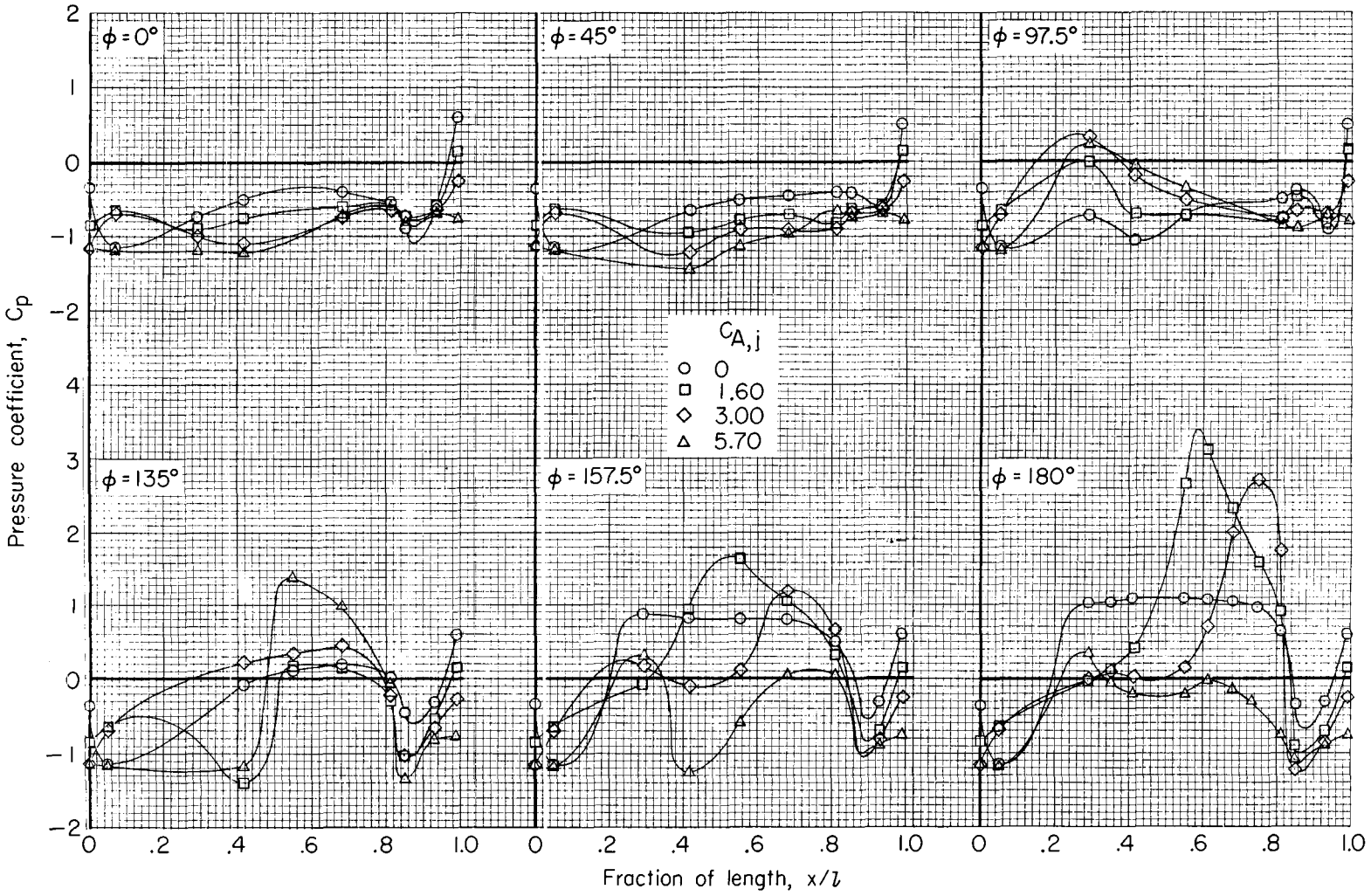

(d) $\alpha = 55^0$.

Figure 27.- Concluded.

CONFIDENTIAL

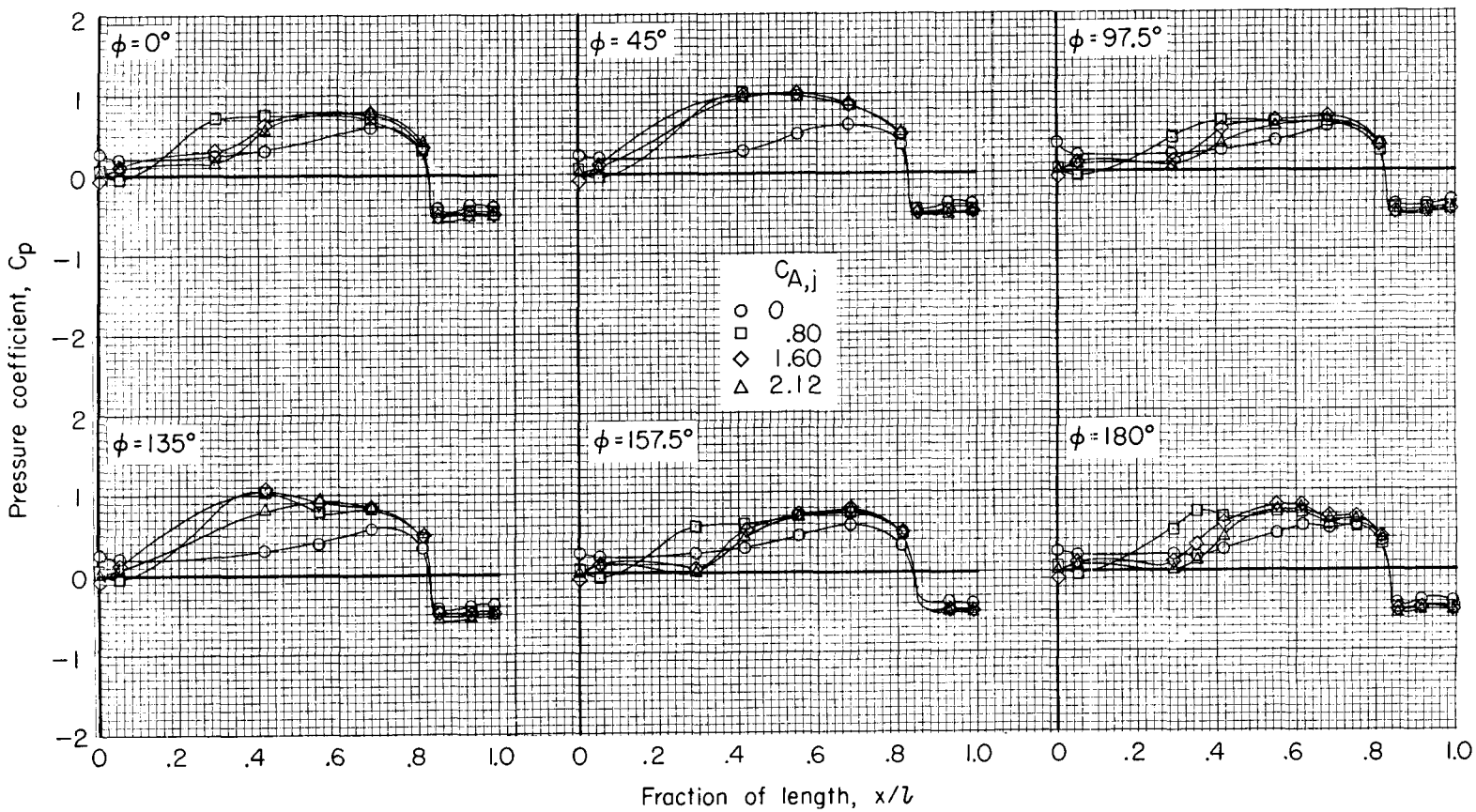

(a) $\alpha = 0^0$.

Figure 28.- Pressure distributions around command module at M = 1.3.

CONFIDENTIAL

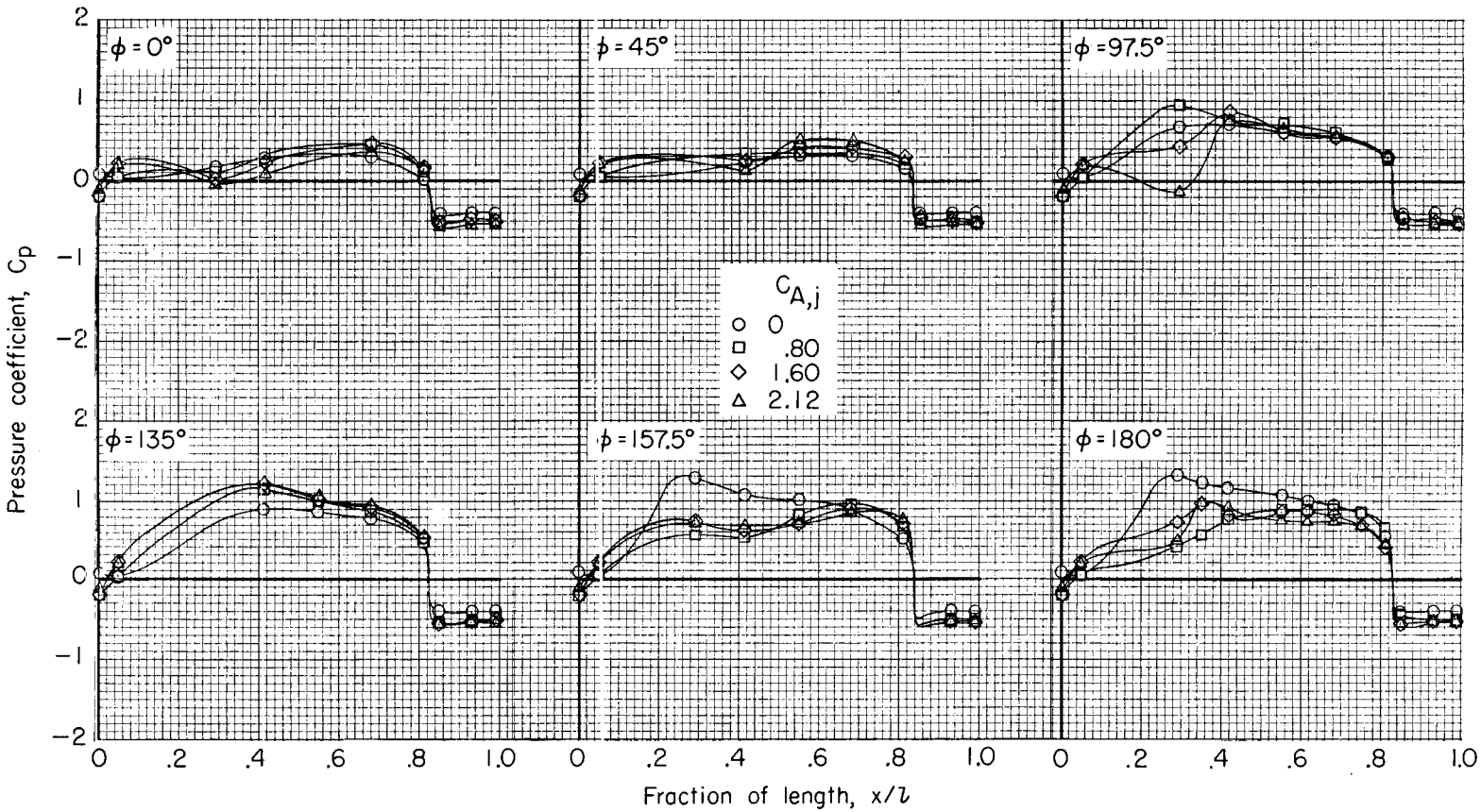

(b) $\alpha = 15^0$.

Figure 28.- Continued.

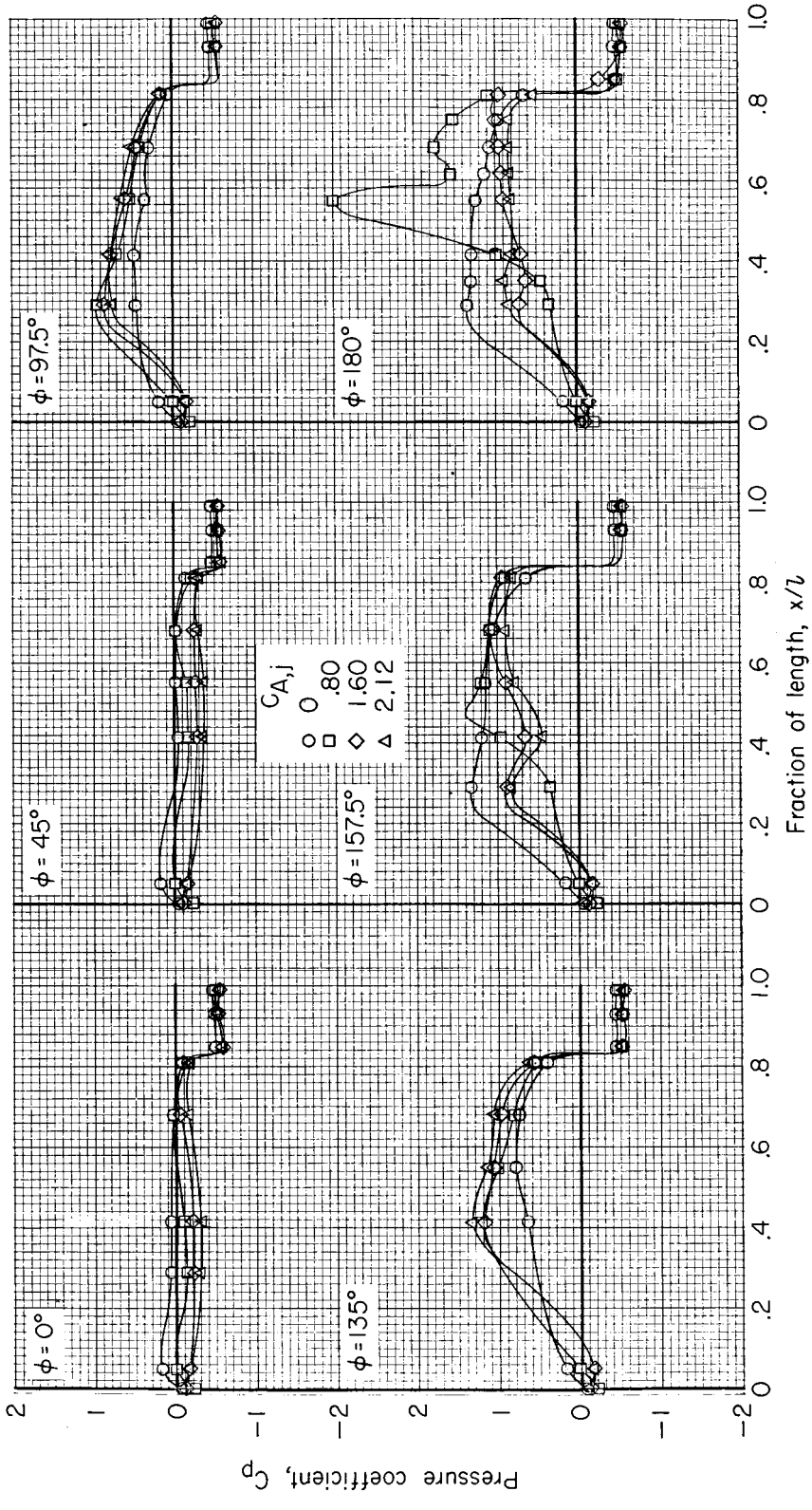

(c) α = 31°.

Figure 28.- Continued.

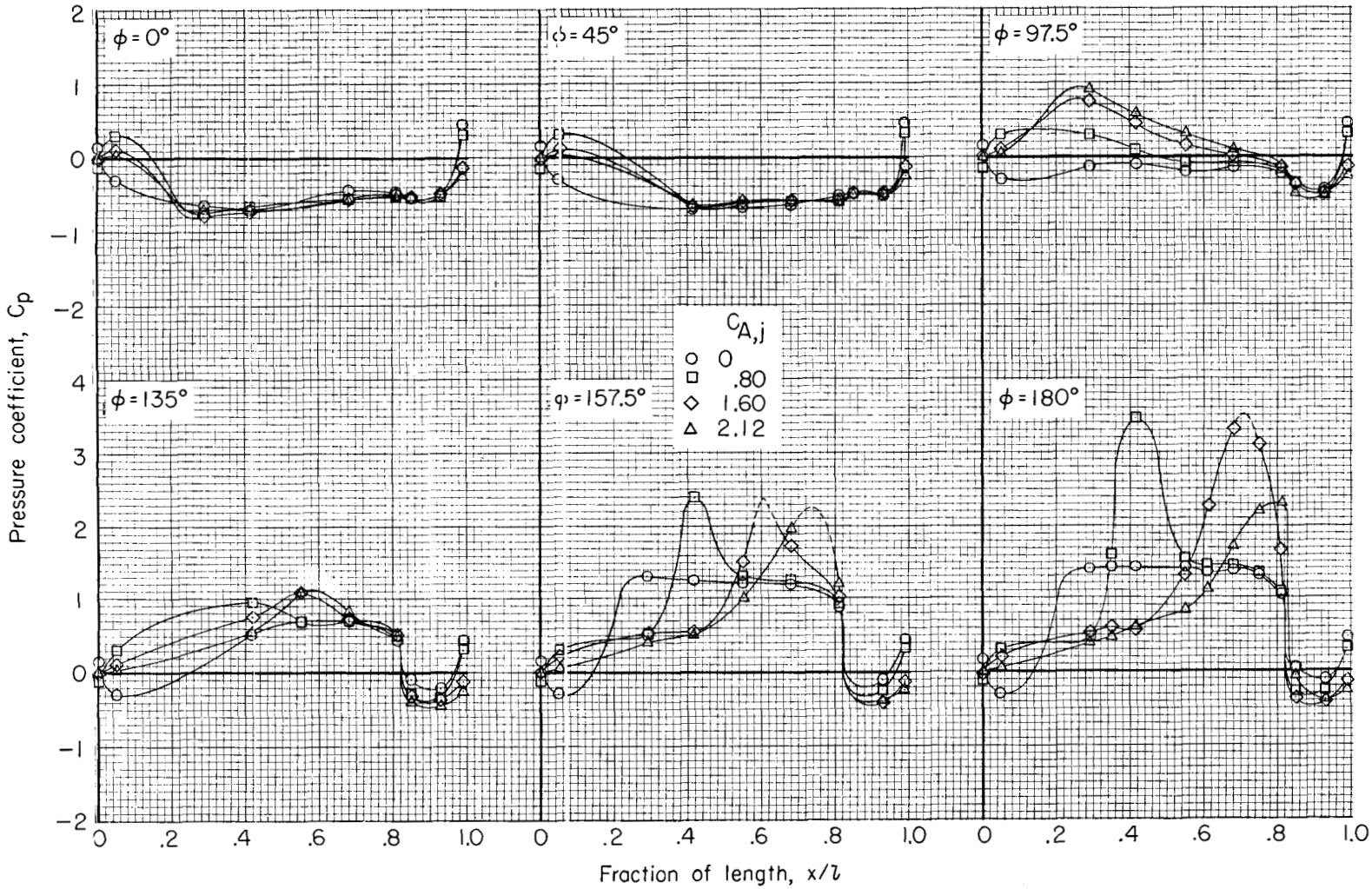

(d) $\alpha = 55^0$.

Figure 28.- Concluded.

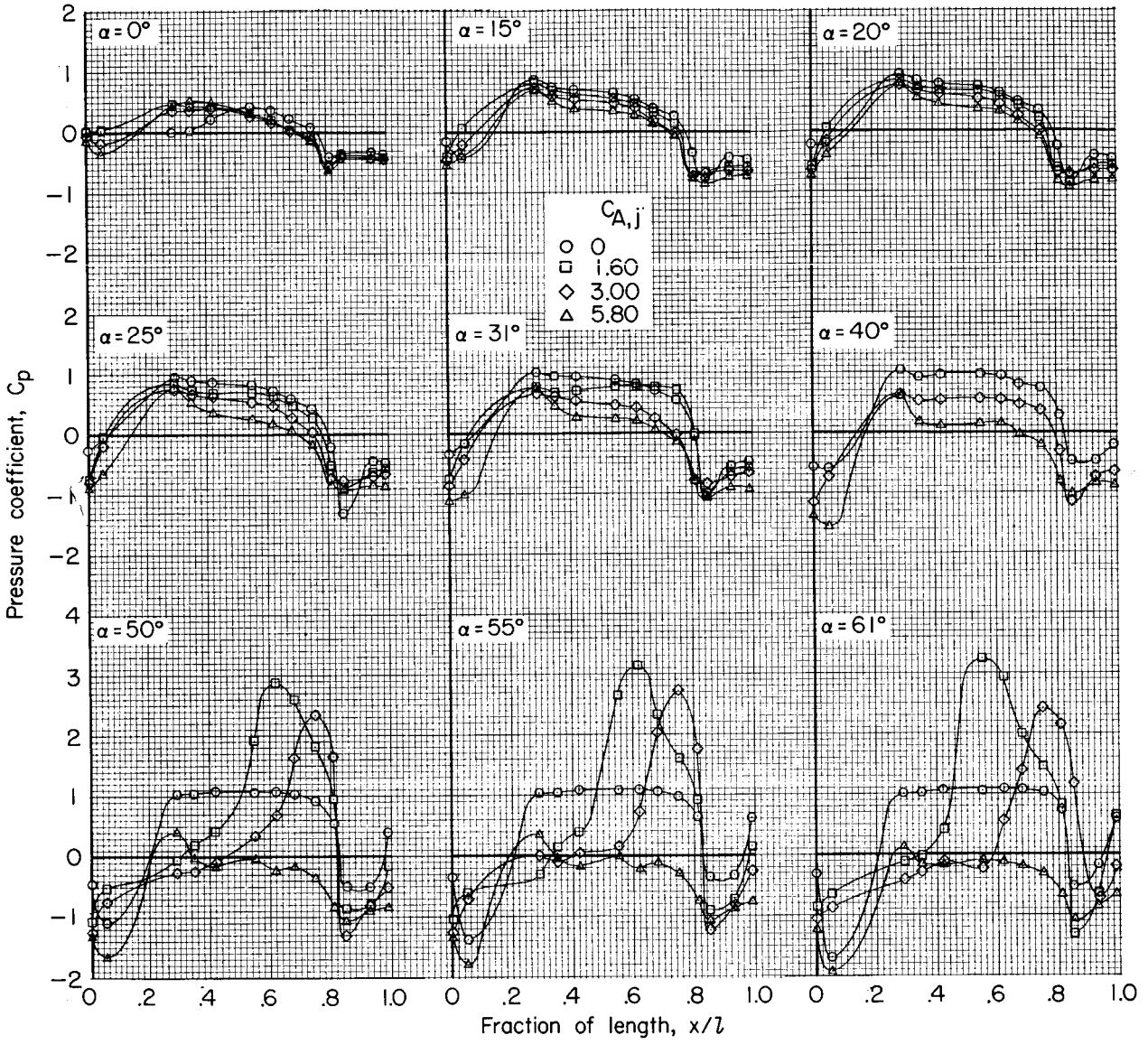

(a) M = 0.50.

Figure 29.- Effect of angle of attack on command module pressure distributions at $\Phi = 180^{\circ}$.

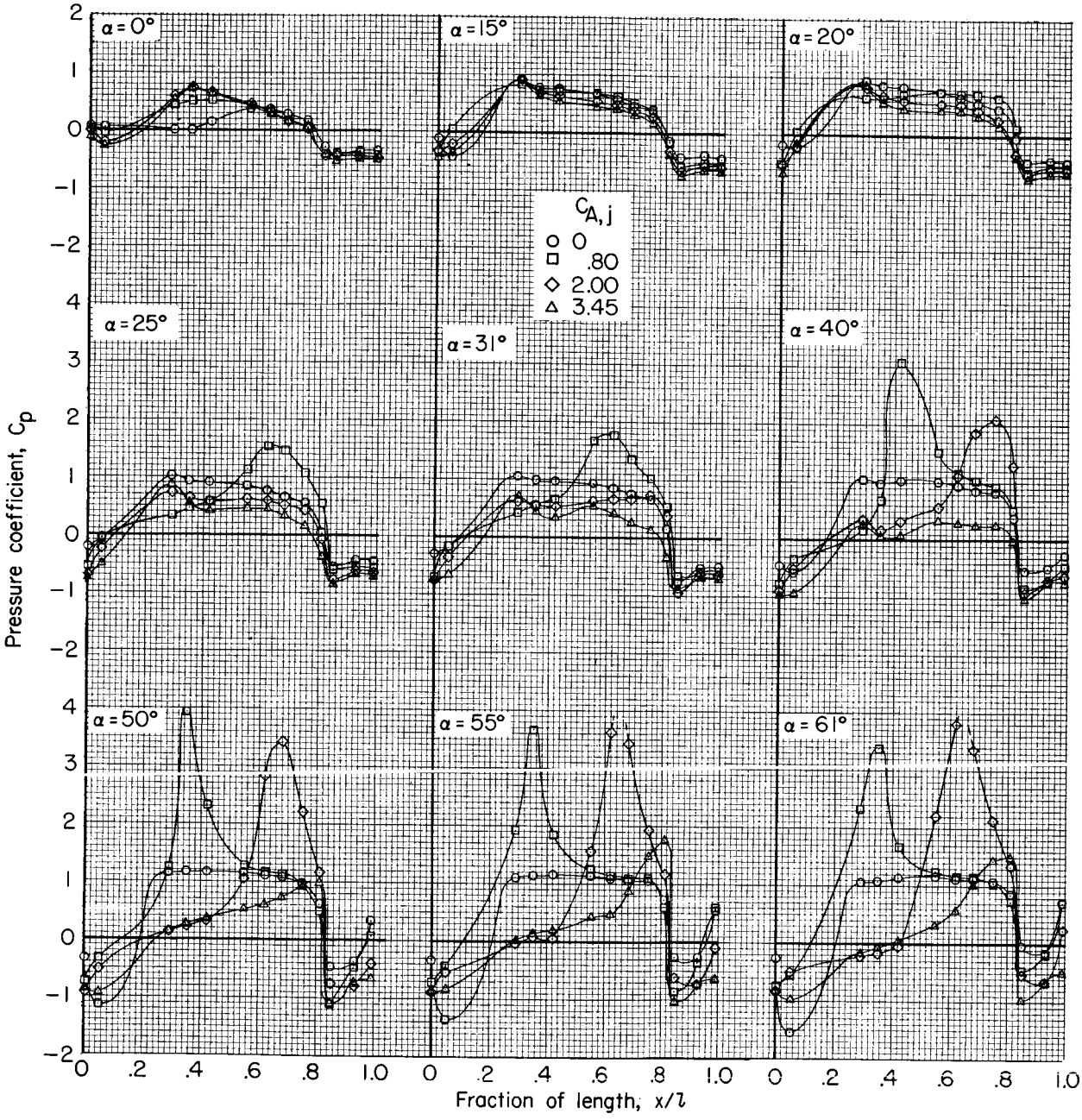

(b) M = 0.70.

Figure 29.- Continued.

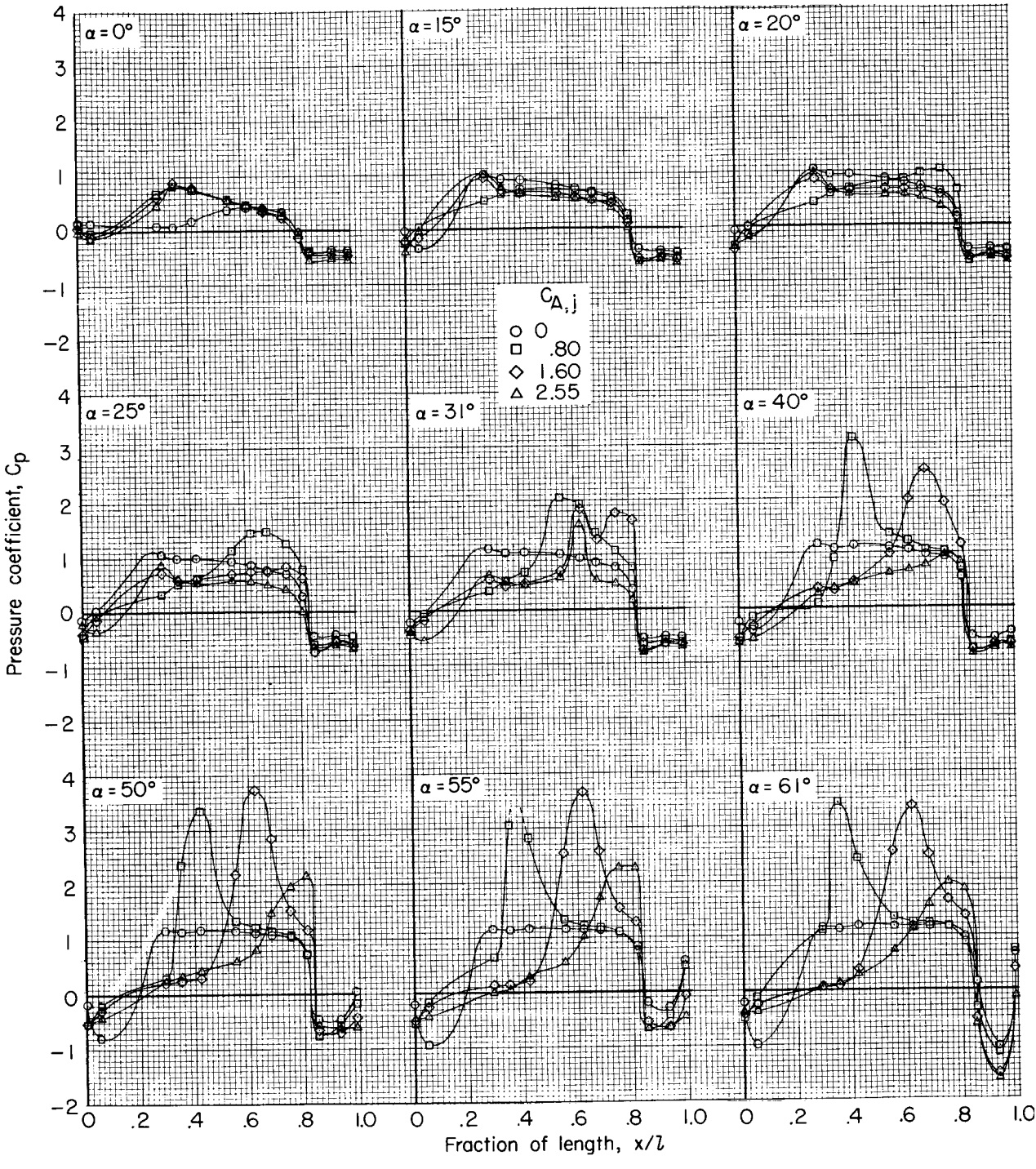

(c) M = 0.90.

Figure 29.- Continued.

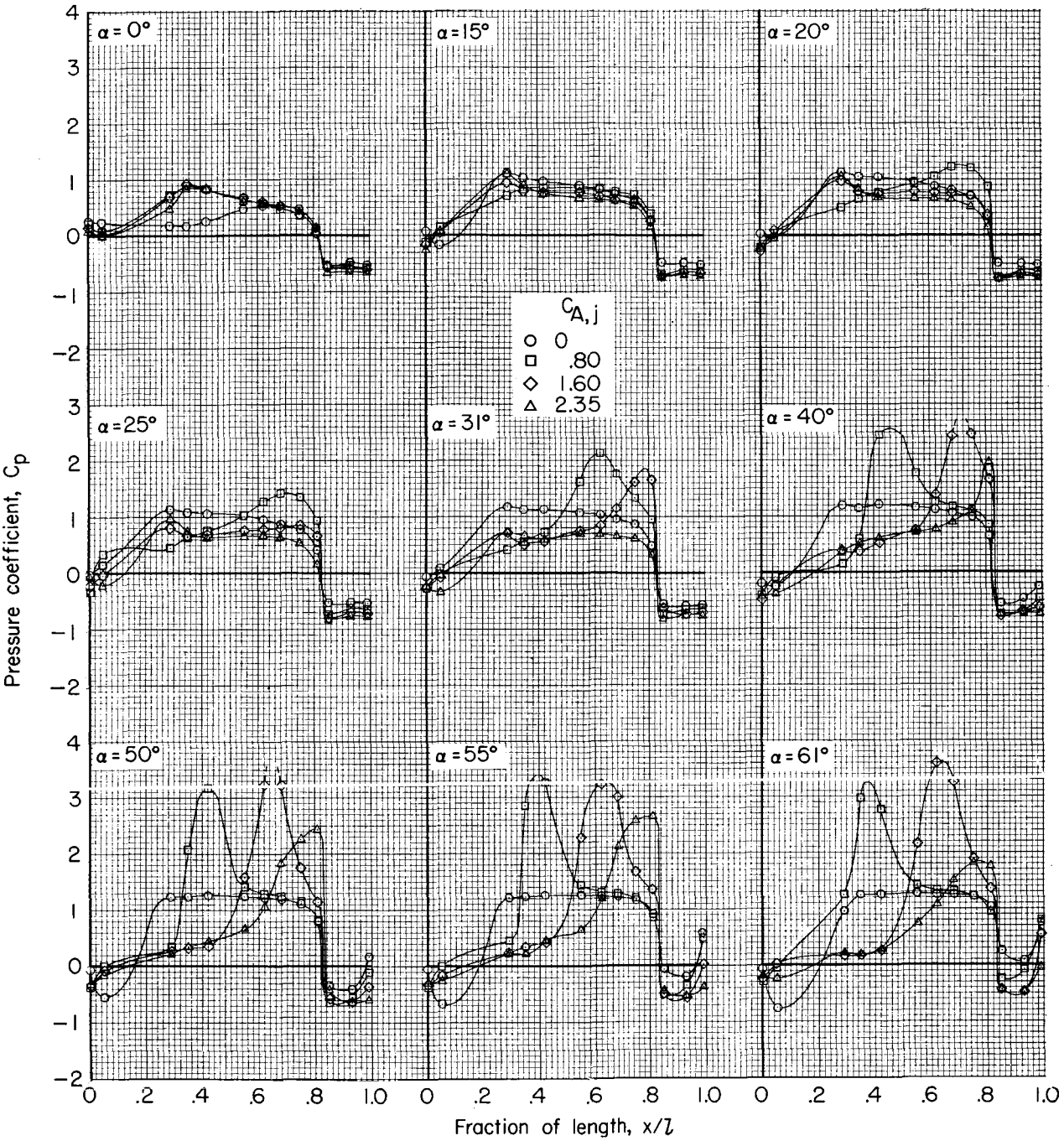

(d) M = 1.00.

Figure 29.- Continued.

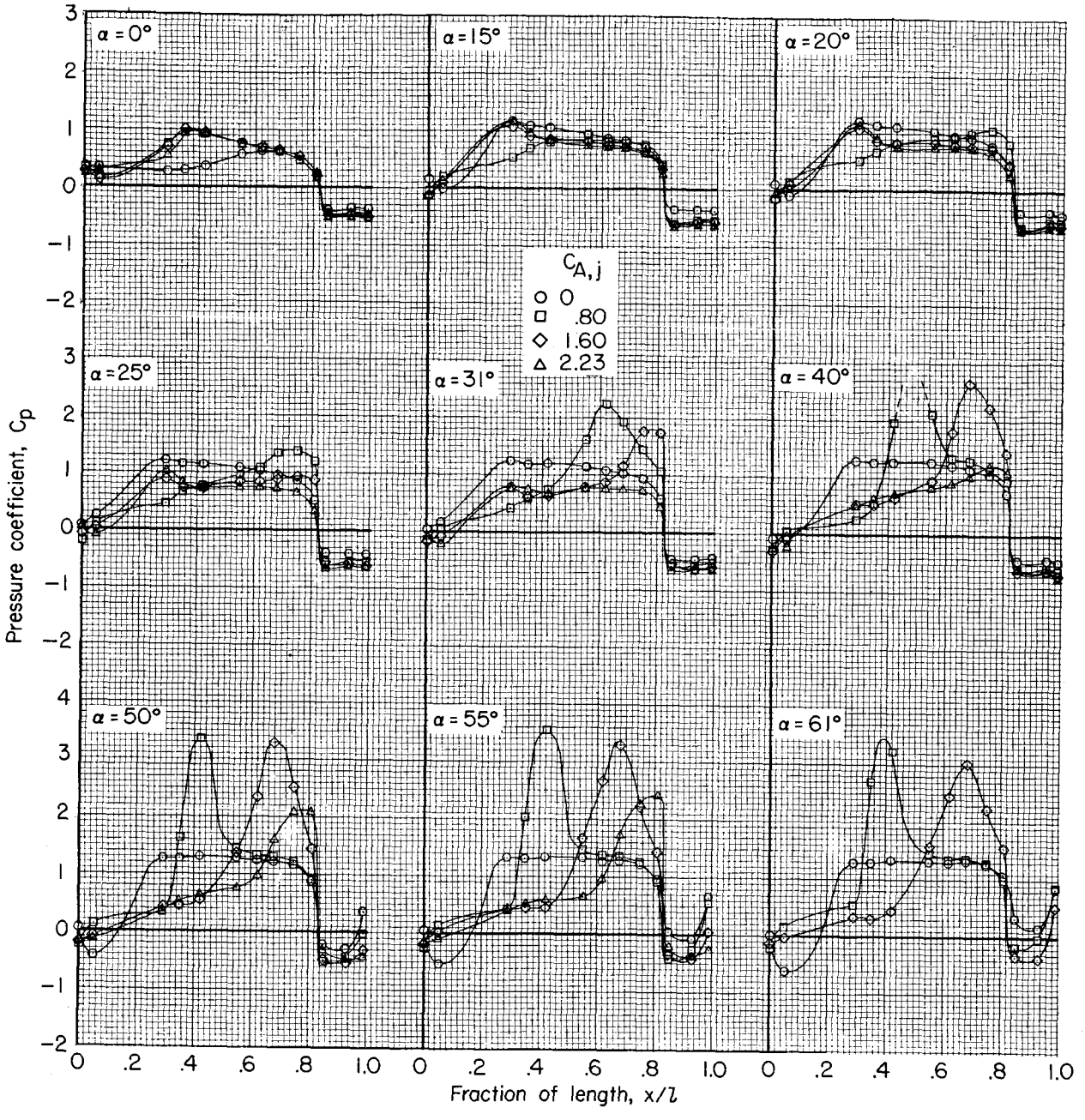

(e) M = 1.1.

Figure 29.- Continued.

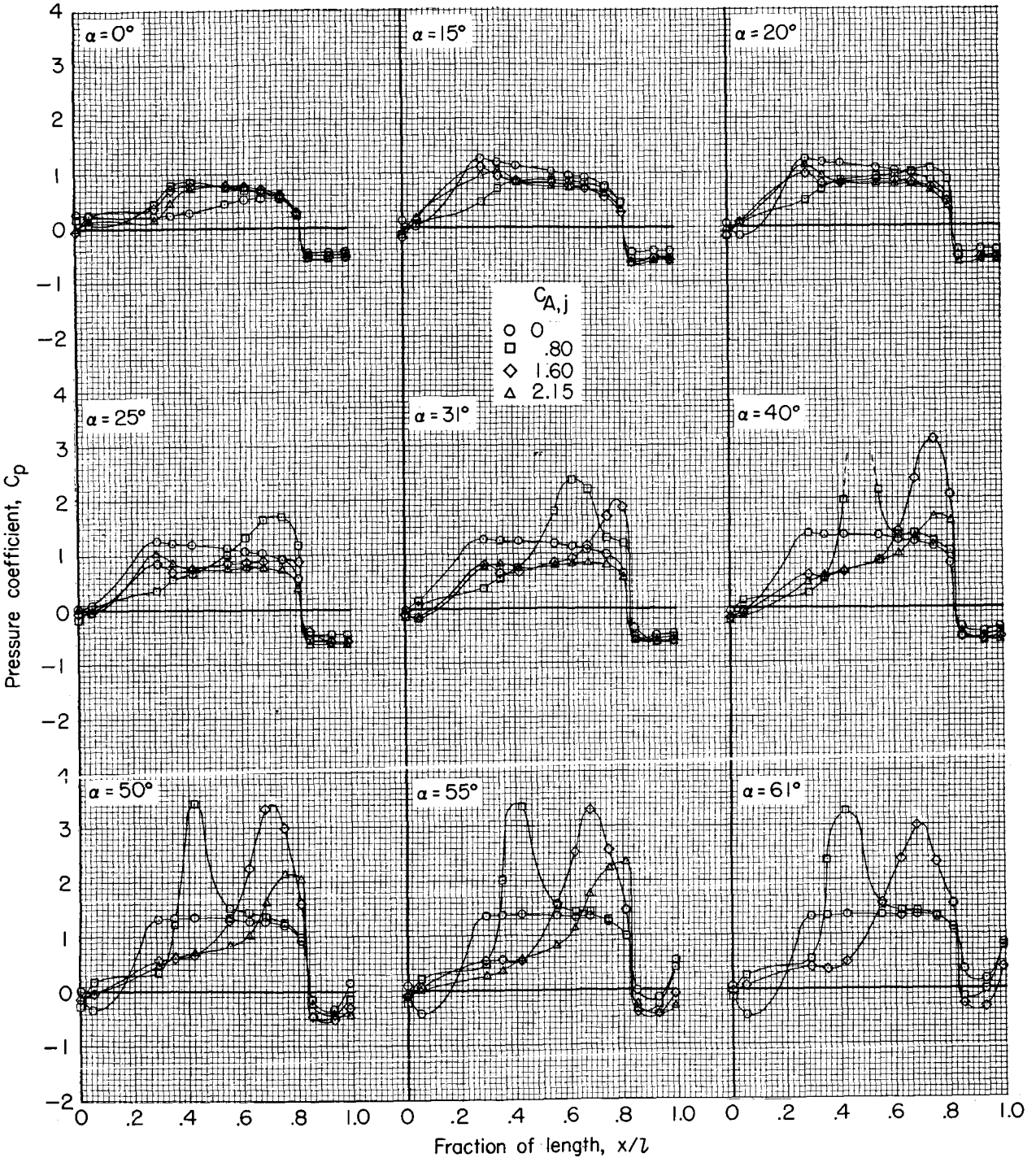

(f) M = 1.2.

Figure 29.- Continued.

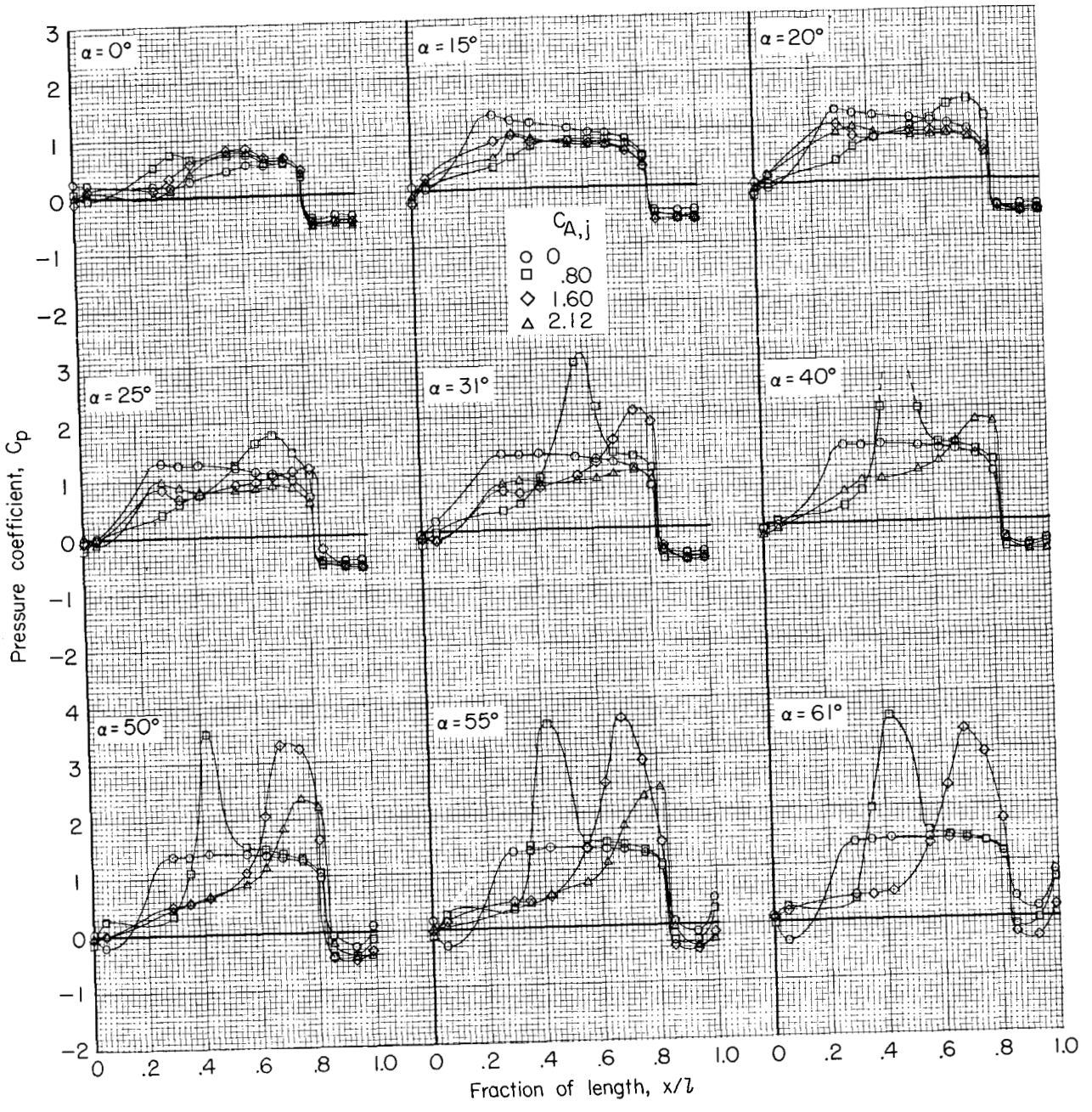

(g) M = 1.3.

Figure 29.- Concluded.

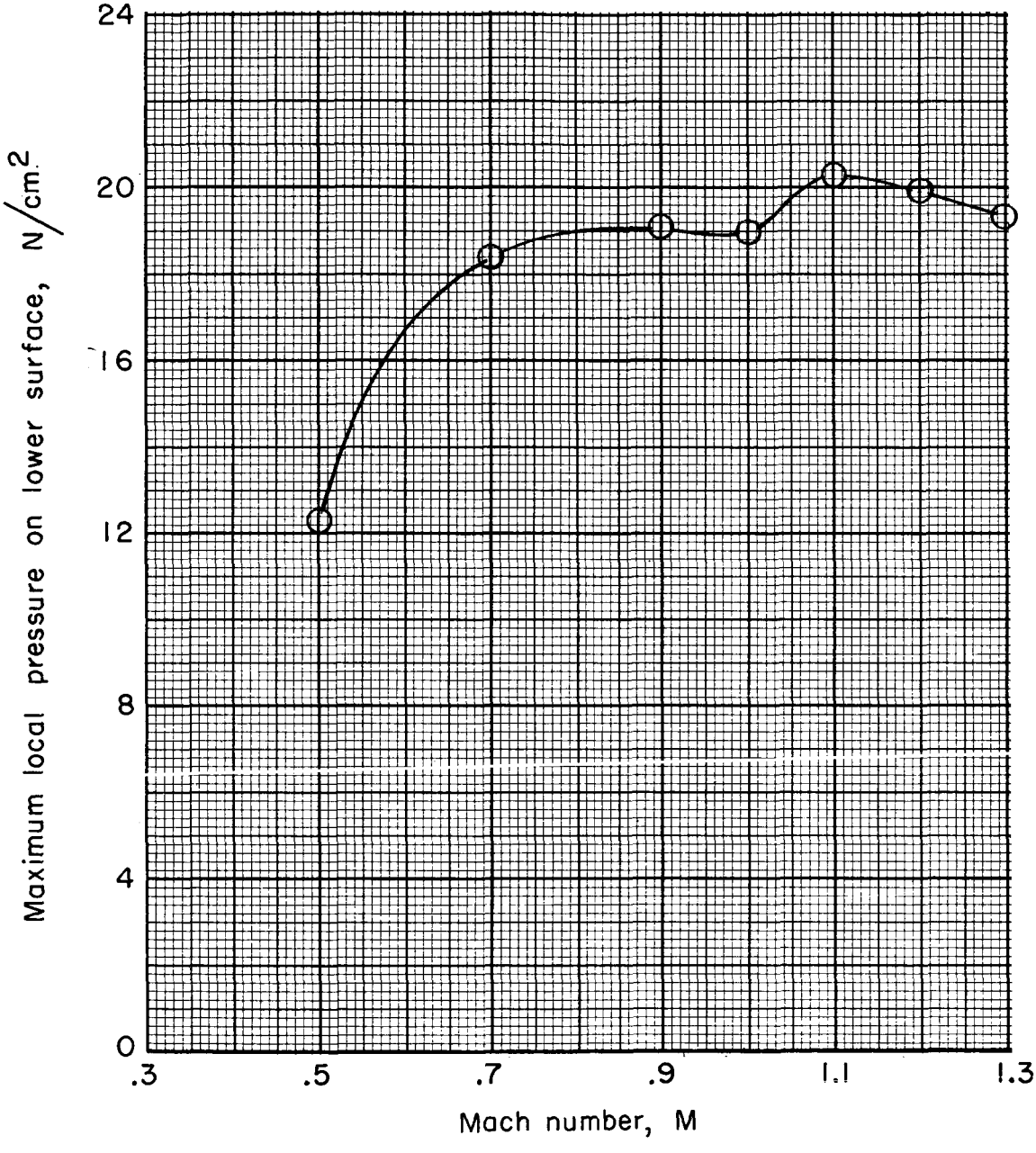

Figure 30.- Peak pressures on the command module due to impingement at $\Phi = 180^{\circ}$.